The Nucleus

An Open Access International Scientific Journal

The Nucleus

Published since 1964

CONTENTS

Occupational Hazards and Environmental Consequences of Sandstone Mining: A Case Study from Soorsagar, Jodhpur, Rajasthan

Bikas Saha

Department of Geology, Durgapur Government College, Durgapur, West Bengal, India

ABSTRACT

Mining plays a crucial role in the economic growth and supports national development. However, it also raises significant concerns due to its environmental impact and health risks, particularly in the nearby areas. In India's sandstone mines, both mechanical and manual methods are employed. Mining operations rely heavily on equipment such as trucks, dumpers, compressors, drills for blasting, and cranes for lifting heavy blocks. These activities generate large amounts of dust containing high levels of silica, which poses severe health risks. Prolonged inhalation of silica dust can lead to silicosis, a preventable but serious disease characterized by dyspnoea (shortness of breath) and persistent cough, and is sometimes associated with lung cancer and tuberculosis. Silicosis is one of the most common occupational diseases globally and has a significant impact on workers' health in developing countries like India. The use of heavy machinery and vehicles also creates high levels of noise and vibration in the surrounding. Prolonged exposure to noise can result in occupational hearing loss due to neurosensory deafness. Additionally, continuous exposure to whole-body vibrations leads to degenerative spinal conditions, including chronic back pain. Although stone quarrying near Soorsagar, Jodhpur, contributes to both the rural and national economies, its environmental consequences are considerable. Unplanned and haphazard quarrying has resulted in environmental degradation, and unauthorized mining activities have further worsened the local ecological balance.

Keywords: Sandstone quarrying, Environmental Pollution, Occupational Health Hazard, Silicosis, Dust pollution, Noise pollution

Introduction

In today's world, in most countries, mining involves initial mineral exploration, mineral extraction, and processing, including the extracted material's crushing, grinding, and washing. Exploration, mine development, mine operation, decommissioning, and land rehabilitation comprise a mine area's life cycle. Mining is a multidisciplinary sector that utilizes a variety of trades and professions. Because the term "miner" is somewhat ambiguous, it is crucial to ascertain the specifics of mining tasks in order to guarantee accuracy in clinical and epidemiological studies.

One of the most common types of sedimentary rocks, sandstone is found in sedimentary basins all over the world [1]. The aerial extent of sandstone deposits in India is about 1.79 million sq. km [2]. Sandstone rocks are made up of varying percentages of 'so-called' framework grains, comprising of minerals, rock fragments, organic compounds, with cement and matrix in the interstitial spaces between them. Quartz is by far the most common framework grain for siliciclastic sandstones, along with feldspar. The most prevalent mineral on Earth's surface is quartz, which comes in a variety of hues including white, grey, purple, yellow, brown, black, pink, green, and red. Sandstone with predominant quartz grains is considered a texturally mature rock, compared to feldspar-dominated sandstone [1]. The Indian states of Andhra Pradesh, Assam, Bihar, Gujarat, Haryana, Madhya Pradesh, Meghalaya, Mizoram, Karnataka, Odisha, Punjab, Rajasthan, Uttar Pradesh, Tamil Nadu, and West Bengal are among those where sandstone occurs. Rajasthan produces about 90 % of the total sandstone extracted from India. The sandstone mines of Rajasthan are spread over the districts of Bharatpur, Dholpur, Kota, Sawai-

Madhopur, Karauli, Bundi, Jhalawar, Chittorgarh, Jodhpur, Bikaner, Nagaur and Jaisalmer. Due to rapidly growing infrastructural development, the importance of mining is also increasing, especially to meet the demand for metals, minerals and building stones. Sandstone is one of the most important building materials. Roofing, flooring, pavement, paneling, beams, pillars, arches, door and window sills, wall-facings, fence posts, milestones, and many other applications are among the various uses for it. As a building stone, sandstone is acid resistant, alkali resistant as well as thermally resistant. On sandstone, the impact of salty winds is minimal and sandstone is appropriate for carving and making windows and decorative and ventilatory friezes (jallis). So sandstone is useful for covering the exterior of coastal buildings. It is also suitable for flooring, wall fixing & lining in chemical industries due to its acid and alkali resistant properties. Humans have used sandstone as building material for centuries. Therefore, many historical structures and monuments are composed of sandstone like the Buddhist Stupas of Sarnath, Red Fort, Sansad Bhawan, Rashtrapati Bhawan, the National Museum, Chhitar Palace, Jodhpur, etc. [3].

Mining has consistently been one of the riskiest professions [4]. The hazards and hazardous working conditions in mines were brought to light by the Second National Commission on Labor. Workers in mines face significant health hazards that shorten their lives. Due to inadequate protection and care, both on and off site, the miners get affected by the biggest health threats like silicosis, pneumoconiosis and tuberculosis [5]. A large amount of fine dust is generated due to quarrying and crushing of stones. This fine particulate matter contains free silica in the range of 20 to 70% [6]. Breathing in fine crystalline silica dust can cause cancer, bronchitis or

---

silicosis. As the silica dust enters in the lungs, annoying them ceaselessly, lung capacities will reduce [7, 8]. Apart from silicosis, accidents are frequent in mine areas, especially when miners work without any safety gear. Sometimes workers lose their limbs due to these accidents. In India, 20% of on-site deaths take place due to falling objects [9]. Apart from these, noise and vibration are created due to heavy machinery, blasting, transport vehicles, hammering and chiseling; these are also very hazardous for the mine worker. Mining is one of the most common jobs in India, despite being a dangerous one. Mining employs a sizable portion of the labor force and will continue to expand in the future [4, 10].

Social well-being and economic development of any modern society depend on the mineral resources of that society or nation [11]. The importance of mining has been advanced greatly due to the rapidly rising need for all types of minerals and metals. As a result, global mining industries have been booming since the early 20th Century and these industries not only produce jobs at national, state and regional levels but also increase the earning of tax revenues and foreign currency for the nation [12]. However, mining has detrimental effects on society and the environment. The majority of the detrimental impacts of mining operations have a significant impact on the nearby communities that reside near the mining sites [12-15]. Mining has been practiced across the world and is not confined within a single country [16-18]. Additionally, mining has developed best practices to lessen related problems. Conflicts between developmental works of any nation and environmental degradation of that nation are the obvious outcome due to any unplanned and haphazard human involvement in the ecological sphere. Moreover, though mining may be fulfilling the necessity of resources and thus contributing in the direction of the regional economy, the unverifiable practice of mining deeply affects the local environment.

Examples of these human involvements are the rigorous agriculture, industrialization, extension of roadways as well as railways, construction of dams etc. that accompany development. An essential component of the growth of the human socioeconomic system is mining. Excavation of minerals, stones and coal have yielded a footing for local economy across the globe. Local bodies are engaged in the extraction procedure almost everywhere. The social web of a region experiences unexpected changes due to mining [19]. Above Around 20 million people worldwide rely on the unregulated mining of mineral resources as their primary source of income, which is much more in terms of numbers than workers employed in formal mining industries [20]. A considerable portion of Indian rural households to subsist, these non-farm occupations as their primary source of income [21]. Among the mining workers and their families, a few significant social problems are found, such as illiteracy, child marriage, child labor, and loneliness etc.

Geological background

The End-Proterozoic geological events in the north-western submerged continental shelf of Indian plate is represented by the Marwar basin [22, 23]. The Marwar Supergroup, also known as the Trans-Aravalli Vindhyans, overlies Malani Rhyolites of Neoproterozoic age [24-26]. The more or less horizontal, unmetamorphosed and undeformed Marwar Supergroup is subdivided into the Jodhpur Group, Bilara Group and Nagaur Group in order of superposition [27, 28]. Three formations namely the Pokaran Boulder Bed at the bottom, the Sonia Sandstone at the middle and the Girbhakar Sandstone, at the top, make up the Jodhpur Group [28-30] (Table 1: Stratigraphic Succession, Fig. 1). Around 60 m thick, undeformed, unmetamorphosed, arenaceous Sonia Sandstone Formation commonly overlies the acid volcanic rocks of the Malani Rhyolite and the argillaceous sedimentary strata of the Girbakhar Formation are uncomfortably layered atop it [28].

Table 1: Generalized Stratigraphic Succession of the Marwar Supergroup (after [28, 31])

Age	Supergroup	Group	Formation	Lithology
Permo-Carb.	Bap Boulder Bed			Subrounded, ellipsoidal cobbles and pebbles
		———————————————— Unconformity ————————————————		
Ediacaran to Middle Cambrian	Marwar Supergroup	Nagaur Group (75 – 500 m)	Tunklian Sandstone	Brick red sandstone, siltstone & red claystone
			Nagaur Sandstone	Brick red sandstone, siltstone & red and green clay beds
		Bilara Group (100 – 300 m)	Pondlo Dolomite	Cherty dolomitic limestone
			Gotan Limestone	Interbedded dolomite & limestone
			Dhanapa Dolomite	Dolomitic limestone with cherty lenses, sandstone with cherty lenses
		Jodhpur Group (125 – 240 m)	Girbhakar Sandstone	Brick-red sandstone, siltstone and shale, pebbly to gritty near top
			Sonia Sandstone	Maroon siltstone and shale, cream sandstone with sedimentary structures. Banded chert-jasper, subordinate dolomite and sandstone
			Pokaran Boulder Bed	Sub-rounded, ellipsoidal cobbles, pebbles and sandstone
		———————————————— Unconformity ————————————————		
779 – 681 Ma	Malani Igneous Suite			
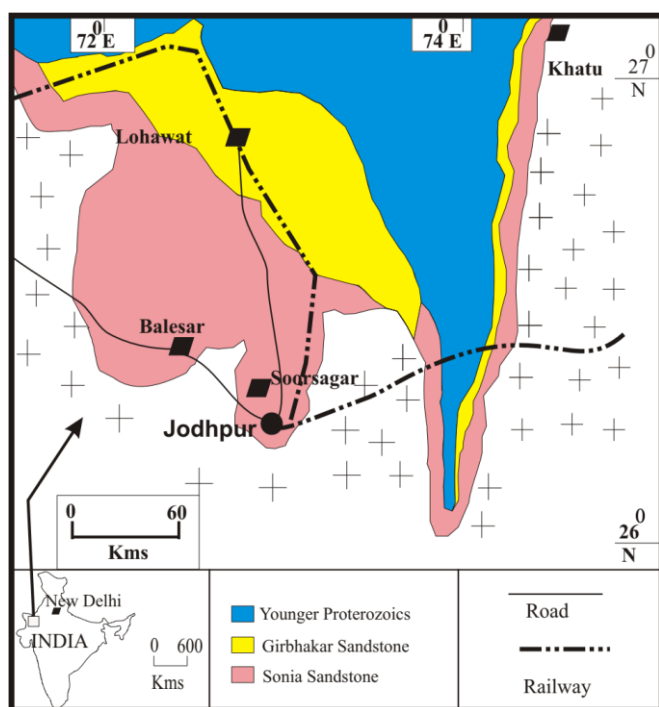
Fig. 1: Location and geological context of the research area: an outcrop map illustrating the spread of the several formations that make up the Marwar Supergroup (after [32]).

Combining the Sonia Sandstone and Girbhakar Sandstone, as per Pareek [28], into the Jodhpur Sandstone, Chauhan et al. [31] subdivided the Jodhpur Group into the Pokaran Boulder Bed and Jodhpur Sandstone Formation. The lowermost Pokaran Boulder Bed Formation of the Jodhpur Group is developed in the Northern part of the basin, is about 4 m thick, and is followed by the Jodhpur Sandstone Formation. Exposed in an elongated area, the Marwar Supergroup is bounded by basin-margin fault systems trending roughly NNW–SSE and N–S [32]. Sag basins or intracratonic rifts are the places where the Marwar Supergroup was deposited [22, 32].

This present paper deals with the sandstone mining from the deposits within the shallow marine interval of the Marwar Supergroup's unmetamorphosed and undeformed Sonia Sandstone Formation, that are exposed ~7 km north-west from Jodhpur town, Rajasthan, India [27, 31] (Fig. 1).

Discussion

Humanity started mining and quarrying from the 'Stone Age', before they started to use fire. Humans were used to use rocks and stone for hunting animals for their food. Even in this era, the necessity of obtaining materials like stone, metals and ceramics has been increasing with time due to tremendous population growth. As a result, the mining and quarrying sectors are growing tremendously, in terms of extents of mining areas and intensity of this activity, for the past few years. In terms of quality and quantity, India has an abundance of minerals and rocks available across the country. At present, India produces 27% of the total stone of the World. One of the major sandstone production centres

and a craftsmanship centre in India is Jodhpur, Rajasthan. According to the Indian Bureau of Mines [33], Rajasthan used to produce about 90 % of the sandstone of India. Considering the favorable color and texture of the sandstone, Jodhpur produces a vast variety of sandstone. Sandstone from Rajasthan has been widely used because of its high quality, which includes regular bedding, consistent grain size, acceptable character, and durability (Fig. 2). It is even exported, to Canada, Japan and the Middle Eastern countries [34].

Fig. 2: Use of Sandstone as building materials – from quarried raw material i.e., slabs of sandstone (left side) to finished building of sandstone (right side).

Jodhpur city is situated in the eastern margin of the 'Thar Desert' in Rajasthan. As per the available literature, the sandstone quarrying in the region started sometime in 16th century. Most of the historical buildings of the city, the Jodhpur Palace, the Meharangarh Fort and Royal Tombs at Mandore Garden are made up of this sandstone. The sandstone mining activity lies very close to Jodhpur city within a distance of 8–10 km in the north [35]. Two and half million people are employed in and around the 30,000 mines present in Rajasthan. Out of these 30,000, 1300 are sandstone mines engaging around 71,000 workers [34]. These approximately 71,000 sandstone workers in the mines do a variety of tasks, including as drilling, blasting, breaking down larger stones into smaller ones and loading & unloading of slabs from trucks. These tasks expose mine employees to high concentrations of silica dust for extended periods of time [36] (Fig. 3). The Jodhpur district in Rajasthan is composed of several geological elements such as sandstone, limestone, granite, rhyolite, schist, phyllite, and slate [37]. One of the main hubs for the quarrying and artisanal production of sandstone in India is Jodhpur, where miners extract a diverse range of sandstone types in terms of color and texture. Jodhpur and the surrounding areas have seen a rise in the number of sandstone quarrying and processing operations as a result of a boost in exports over the past 20 years. Currently, one of the most significant economic sectors in Jodhpur is the quarrying and processing of sandstone [35]. The largest industry of Jodhpur district is the sandstone quarrying. Government earns about 12 crores annually through taxes [35]. Among the large numbers of

quarries in the area, the major ones include Fedusar, Keru, Soduki Dhani, Pabu Magra, Barli, Chaina ka Bariya, Brahmno ka Tanka, Mandore, Kali Beri, Ghora Ghati, Balsamand, Old Fort, Magji ki Ghati, Palri and Soorsagar. Among these mining areas, Keru, Fedusar, Soorsagar and Mandore are the biggest blocks and are extensively quarried [35].

There are 2.5 million workers engaged in mining in Rajasthan [38]. Unfortunately, most of these mines are from an unorganized economic sector [36]. Workers in the majority of the unorganized sector face dangers to their bodily and mental health due to their line of work [39] and carries an increased risk of exposure to harmful chemicals [40].

Fig. 3: Silica dust generated due to different types of mining activities. This dust reduces the lung's ability to function by causing silicosis, or the fibrosis of lung tissues.

Silicosis is a lung ailment that is commonly encountered by miners and employees in related industrial and construction sectors. This avoidable sickness is brought on by breathing in silica-containing dust that is produced during various mining operations. There are two types of silica: amorphous and crystalline. Crystalline silica is more harmful than the amorphous silica. Polymorphs of crystalline silica include tridymite, cristobalite, and quartz. The crust of the Earth is covered with an abundance of silica, composed mainly of quartz [41]. Crystalline silica emits free silica into the mine area during various mining operations, such as drilling, cutting, and crushing of rocks. Workers in mines breathe in and deposit silica dust particles, which results in chronic inflammation and the development of granulomas. Additionally, silica dusts induce lung tissue fibrosis, which lowers the lungs' ability to function [41-43]. In addition to this, mine workers who are exposed to crystalline silica dust may develop silicosis, pulmonary TB, and chronic obstructive pulmonary disease (COPD) [44]. Based on the duration of silica exposure and radiological results, three types of silicosis can be distinguished: accelerated, chronic, and acute [45]. Because silicosis is linked to a number of illnesses, including lung cancer and tuberculosis, it increases occupational morbidity and death [46].

Mechanized operations like drilling, crushing, screening, blasting, and so forth cause noise levels to be far higher than the suggested noise threshold of 90 dB(A). Consequently, neurosensory deafness causes occupational hearing loss in mine workers exposed to high noise levels. There have been reports of noise levels during drilling reaching 115–122 dB or higher (Fig. 4). Extremely high noise levels and explosive blasts have the potential to rupture the tympanic membrane, impairing hearing at all frequencies and perhaps causing hemorrhaging into the middle or inner ear.
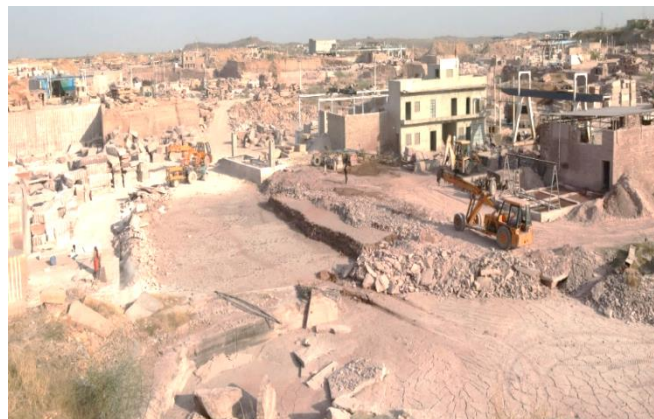
Fig. 4: Due to automated procedures including drilling, crushing, screening and blasting, etc., noise level is much higher than the recommended limit. Moreover, Workers who use pneumatic tools like drills can get vibration illnesses.

To save time, heavy earth moving machines have been introduced in the mining operation in the Soorsagar quarry, Jodhpur (Fig. 4). Consequently, there is now a greater risk of whole body vibrations for operators. Chronic whole-body vibration exposure leading to degenerative spinal diseases, including back pain. After a few months to several years, pneumatic instruments like drills cause vibration disorders in workers. The most prevalent vibration disorder is Raynaud's phenomenon i.e., vasospasm, which is characterized by the spasmodic contraction of finger blood vessels that briefly causes the fingers to turn white and numb.

Nearly all human activities have an adverse effect on the ecosystem, ecology, and terrain. But due to the mining activities, local environments are degraded due to stripping of topsoil, destruction of the vegetation, altering soil properties and thus disturbing nearby ecosystems. As a result, the existing landscape and environment are being ruined [35, 47, 48, 49]. Mine dumps and tailings, one of the major problems in the mining industry, are also the cause of degraded environment [50, 51] (Fig. 5). Adverse environmental changes due to unsystematic disposal of the mining waste will affect the agricultural land, forest land, surface & subsurface drainage, flora & fauna etc. The fact that the visible negative effects of environmental degradation are so evident as a result of developmental activity is concerning. Thus, the best course of action for improving the situation is to develop the area sustainably by extracting its

mineral wealth while also protecting the ecosystem. One of the major sources of pollution during quarrying and transporting stone is the waste stone dust. It directly jeopardizes the health of the mining employees, because stone dust is the cause of life threatening breathing problems among the mine workers like silicosis, tuberculosis, and chest pains [34, 52- 54]. Due to wind and surface runoff, the stone dust is being deposited on the soil and crop lands. As a result, the soil quality and crop production are decreasing [49, 55].

Fig. 5: The environment is affected by the mine dumps and tailings

Conclusions

Millions of people are employed globally in the mining industry. Mining can be carried out on a large, medium, or small scale under extremely hazardous working conditions, or it can be done on a high tech level in large mines with adequate working conditions and safety for the miners. With an average of one million people employed every day and an annual turnover of over 40 billion US dollars, India boasts a unique blend of large and small, manual and mechanized, opencast and underground mines that contribute to roughly 2.5% of the country's GDP [63]. The most common occupational lung disease among mine workers is still silicosis, a condition linked to dust. Over a century of accident data and safety experience in Indian mines demonstrate a decline in both mortality and accidents over time. The fatality rate per 1000 mine workers, however, has been averaging 0.30 in both the non-coal and coal industries; following a period of steady decline, fatal accident trends increased once more in the 1980s and 1990s. The efficacy of the current, traditional method of enforcing occupational safety and health laws in mines through statutory investigations, inspections, and other means has reportedly reached its limit. It is necessary to develop a strategy that combines "strategic" and "systems" thinking in order to get the mining sector ready to meet higher requirements for the health and safety of mine workers. Together with hazard control, analysis to foresee hazards, and engineering solutions to prevent accidents and occupational diseases, the new thinking must take into account behavioral, cultural, and organizational systems.

Mining activity has increased many fold in the last 10-15 years and caused different degrees of damage to drainage systems, canals, agricultural land, groundwater, vegetation and cultural objects like roads and rail networks, buildings etc. As a result, there is a reduction of the flow of rainwater to the existing tanks and several artificial water bodies are created in the mined-out areas. For mining to grow responsibly in India and around the world, there are a number of factors that must come together, including legislation, mine supervision and control, accurate data on accidents and occupational illnesses, the creation of safety programs, and a safety culture. From the present study, it can be concluded that the health shape of the miners as well as the near-by inhabitants is in critical situations. Improper and unsupportable mining and mining-related wastes are the main culprits for such situations. Through a variety of educational programs and practical training programs, local Government Officials and various Non-Governmental Organizations (NGOs) should take the initiative to raise awareness about potential health effects linked with sandstone quarrying and accompanying dust.

Many steps can be taken to address the unwanted quarrying functions. These are as follows:

By providing the right tools and machinery, miners can reduce the production of excess waste and dust emissions due to mining as the first and most crucial measuring step. Sandstone miners of Soorsagar are still using old-school hand-held chisels and hammers for cutting the blasted stone, without any kind of safety gear. As a result, dust created due to hammering and blasting is spreading across the area which is affecting the miners as well as the local residents. Due to inadequate safety gears, the maximum number of injuries and illnesses is taking place among the miners. Therefore, the mine owners should provide safety gears like helmets, masks, safety goggles, rubber boots and mine workers should use these equipments. Miners can use this water for wet drilling and cutting. They can also spread this water around the mining area to reduce the suspended dust in the area. As the second most important strategy, recycle the generated wastes or turn them into building materials that are useful. Lastly, secure disposal of the trash generated due to mining.

Acknowledgements

References

[1]   F.J. Pettijohn, P.E. Potter and R. Siever, "Sand and Sandstone (Second Edition)," Springer, vol. 559, no. 1-2, 1987.

[2]   A. Ahmad, "Socio-economic and health status of sandstone miners: a case study of Sorya village, Karauli, Rajasthan," Int. J. Res. Med. Sci., vol. 3, no. 5, pp. 1159–1164, 2015.

[3] P. Gupta and A. Laddha, "Jodhpur Sand Stone'–A Splendid Architectural Building Material," Journal of Emerging Technologies and Innovative Research (JETIR), vol. 5, no. 11, pp. 755–761, 2018.

[4] K.S. Cho and S.H. Lee, "Occupational health hazards of mine workers," Bull World Health Organ., vol. 56, no. 2, pp. 205–218, 1978.

[5] M. Shafiei, A. Ghasemian, M. Eslami, F. Nojoomi & H. Rajabi-Vardanjani, "Risk factors and control strategies for silicotuberculosis as an occupational disease," New Microbe and New Infect. vol. 27, pp. 75–77, 2019.

[6] M.I. Greenberg and J. Waksman, "Silicosis: a review". Disease-a-Month," vol. 53, pp. 394–416, 2007.

[7] R. Merget, T. Bauer, H.U. Küpper, S. Philippou, H.D. Bauer, R. Breitstadt & T. Bruening, "Health hazards due to the inhalation of amorphous silica," Arch Toxial, vol. 75, no. 11–12, pp. 625–634, 2002.

[8] D. Macallan, "Malnutrition in tuberculosis," Diagn. Microbiol. Infect. Dis., vol. 34, no. 2, pp. 153–157, 1999.

[9] S. Verma and S. Chaudhari, "Safety of Workers in Indian Mines: Study, Analysis, and Prediction," Safety and Health at Work. vol. 8, pp. 267–275, 2017.

[10] S.S. Nandi, S.V. Dhatrak, D.M. Chaterjee and U.I. Dhumne, "Health Survey in Gypsum Mines in India," Indian J. Community Med. Off Publ. Indian Assoc. Prev. Soc. Med., vol. 34, no. 4, pp. 343–345, 2009.

[11] L. Mancinia and S. Sala, "Social impact assessment in the mining sector: review and comparison of indicators frameworks," Res Policy, 57, pp. 98–111, 2018.

[12] P.P. Mishra, "Coal mining and rural livelihoods: a case of the IB Valley Coalfield, Orissa," Econ. Polit. Wkly., vol. 44, no. 44, pp. 117–123, 2009.

[13] P. Hota and B. Behera, "Opencast coal mining and sustainable local livelihoods in Odisha, India," Miner Econ., vol 29, pp. 1–13, 2016.

[14] A.G.N. Kitula, "The environmental and socio-economic impacts of mining on local livelihoods in Tanzania: a case study of Geita Districts," Cleaner Production, vol. 14, pp. 405–414, 2006.

[15] A. Sincovich, T. Gregory, A. Wilson and S. Brinkman, "The social impacts of mining on local communities in Australia," Rural Soc., vol. 27, no. 1, pp. 18–34, 2018.

[16] C.D. McCullough and M.A. Lund, "Opportunities for sustainable mining pit lakes in Australia," Mine Water Environ., vol. 25, pp. 220–226, 2006.

[17] A. Sincovich, T. Gregory, A. Wilson & S. Brinkman, "The social impacts of mining on local communities in Australia," Rural Society, 2018.

[18] B. Dold, "Sustainability in metal mining: from exploration, over processing to mine waste management," Rev. Environ Sci. Biotechnol., vol. 7, no. 4, pp. 275–285, 2008.

[19] S. Petrova & D. Marinova, "Social impacts of mining: Changes within the local social landscape," Rural Society, vol. 22, no. 2, pp. 153–165, 2013.

[20] L. Wang, J.-L. Zhang and L.M. Liu, "Diversification of rural livelihood strategies and its effect on local landscape restoration in the Semiarid Hilly Area of the Loess Plateau, China," Land Degrad. Develop., vol. 21, no. 5, pp. 433–445, 2010.

[21] A. Das, R. Raj & N.M. Patnaik, "Status, Impact, and Factor Determining Rural Non-farm Economy of India: A Review," Indian Journal of Economics and Development. vol. 16, no. SS, pp. 68–76, 2020.

[22] D.S. Chauhan, "Tectonic and sedimentary evolution of the Marwar basin: A Neoproterozoic–Early Cambrian intracratonic sag basin," In: Proceedings of the Seminar on Geology of Rajasthan – Status and Perspective (A.B. Roy Felicitation Volume) Geology Department, MLSU, Udaipur, pp. 111–125, 1999.

[23] K.S. Valdiya, "Marwar's connection with the Himalayas; In: Geological Evolution of Northwestern India," B.S. Paliwal (ed). Scientific Publishers India, pp. 1–18, 1999.

[24] S.S. Rathore, T.R. Venkatesan and R.K. Srivastava, "Rb–Sr and Ar–Ar systematics of Malani volcanic rocks of southwest Rajasthan: Evidence for a younger postcrystallization thermal event," Proc. Indian Acad. Sci. (Earth Planet. Sci.), vol. 105, pp. 131–141, 1996.

[25] S.S. Rathore, T.R. Venkatesan and R.K. Srivastava, "Rb–Sr isotope dating of Neoproterozoic (Malani Group) magmatism from southwest Rajasthan, India: Evidence of younger Pan-African thermal event by 40Ar–39Ar studies," Gondwana Res. vol. 2, no. 2, pp. 271–281, 1998.

[26] S.J. Malone, J.G. Meert, D.M. Banerjee, M.K. Pandit, E. Tamrat, G.D. Kamenov, V.R. Pradhan and L.E. Sohl, "Paleomagnetism and Detrital Zircon Geochronology of the Upper Vindhyan Sequence, Son Valley and Rajasthan, India: A ca. 1000 Ma age for the Purana Basins," Precamb. Res., vol. 164, pp. 137–159, 2008.

[27] H.S. Pareek, "Basin configuration and sedimentary stratigraphy of Western Rajasthan," J. Geol. Soc. Ind., vol. 22, pp. 517–527, 1981.

[28] H.S. Pareek, "Pre-Quaternary geology and mineral resources of north-western Rajasthan," Geol. Surv. India Memoir., vol. 115, pp. 1–95, 1984.

[29] S.K. Das Gupta and S.S. Bulgauda, "An overview of the geology and hydrocarbon occurrence in western part of Bikaner–Nagaur basin," Indian J. Petrol. Geol., vol. 3, no. 1, pp. 1–17, 1994.

[30] S.K. Das Gupta, "Marwar Supergroup evaporates, Rajasthan. In Recent advances in Vindhyan Geology (ed A. Bhattacharyya)," Geol. Soc. India Memoir., vol. 36, pp. 49–58, 1996.

[31] D.S. Chauhan, R. Bhanwara and R. Narayanan, "Jodhpur sandstone: A gift of ancient beaches to Western Rajasthan," Journal of the Geological Society of India, vol. 64, pp. 265–276, 2004.

[32] S. Sarkar, P. Samanta, S. Mukhopadhyay and P.K. Bose, "Stratigraphic architecture of the Sonia Fluvial interval, India in its Precambrian context," Precamb. Res., vol. 214–215, pp. 210–226, 2012.

[33] M. Vishwanath & A. Singh Rathore, "A Study of Market Scenario of Sand Stone Industry of Rajasthan," Ijfans International Journal of Food and Nutritional Sciences. vol. 11, no. 12, 2022.

[34] A. Ahmad, "Socio-economic and health status of sandstone miners: a case study of Sorya village, Karauli, Rajasthan," Int. J. Res. Med. Sci., vol. 3, no. 5, pp. 1159–1164, 2015.

[35] B.K. Bhadra, A.K. Gupta, J.R. Sharma and B.R. Choudhary, "Mining activity and its impact on the environment: Study from Makrana marble and Jodhpur sandstone mining areas of Rajasthan," Journal of Geological Society of India, vol. 70, no. 4, pp. 557–570, 2007.

[36] P.K. Sishodiya, "Silicosis Detection and Relief Programme: A Case Study of Rajasthan, India. In: Medical Geology in Mining: Health Hazards Due to Metal Toxicity (Eds: K. Randive, S. Pingle, A. Agnihotri)," 2022, Springer Geology.

[37] M. Shafiei, A. Ghasemian, M. Eslami, F. Nojoomi and H. Rajabi-Vardanjani, "Risk factors and control strategies for silicotuberculosis as an occupational disease," New Microbes New Infect., vol. 27, pp. 75–77, 2018.

[38] A. Ahmad, "Awareness of workplace hazards and preventive measures among sandstone mineworkers in Rajasthan, India: a cross-sectional study," J. Health Soc. Sci., vol. 2, no. 1, pp. 69–82, 2017. DOI 10.19204/2017/wrns6

[39] A.M. Donoghue, "Occupational health hazards in mining: an overview," Occup. Med., vol. 54, pp. 283–289, 2004.

[40] N.E. Adler and K. Newman, "Socioeconomic disparities in health: pathways and policies," Health Aff., vol. 21, pp. 60–76, 2002.

[41] D. Rees and J. Murray, J., "Silica, silicosis and tuberculosis," Int. J. Tuberc. Lung Dis., vol. 11, pp. 474–484, 2007.

[42] C.R. Thomas and T.R.A. Kelley, "A brief review of silicosis in the United States," Environ. Health Insights., vol. 4, pp. 21–26, 2010.

[43] H.A. Kawasaki, "A mechanistic review of silica-induced inhalation toxicity," Inhal. Toxicol., vol. 27, pp. 363–377, 2015.

[44] K.M. Pollard, "Silica, silicosis, and autoimmunity," Front Immunol., vol. 7: 97, 2016.

[45] C. Santos, A. Norte, F. Fradinho, A. Catarino, A.J. Ferreira, M. Loureiro et al., "Silicosis-brief review and experience of a

pulmonology ward," Rev. Port. Pneumol., vol. 16, issue 1, pp. 99–115, 2010.

[46] M. Nasrullah, M., Mazurek, J. M., Wood, K.M. Bang and K. Kreiss, "Silicosis mortality with respiratory tuberculosis in the United States, 1968-2006," Am. J. Epidemiol., vol. 174, no. 7, pp. 839–848, 2011.

[47] N. Al-Joulani, "Soil Contamination in Hebron District Due to Stone Cutting Industry," Jordan Journal of Applied Science, vol. 10, pp. 37–50, 2008.

[48] S.D. Odell, A. Bebbington and K.E. Frey, "Mining and climate change: A review and framework for analysis," The Extractive Industries and Society, vol. 5, no. 1, pp. 201–214, 2017.

[49] S. Zia Khan, W. Spreer, Y.Pengnian, X. Zhao, H. Othmanli, X. He. and J. Müller, "Effect of dust deposition on stomatal conductance and leaf temperature of cotton in northwest China. Water. vol. 7, no. 1, pp. 116–131, 2014.

[50] R.K. Bapna, "Marble waste minimization," Rajasthan Mineral Bulletin., vol. 23, no. 3, pp. 17–19, 2002.

[51] U. Forstner, "Introduction. In: Environmental impacts of mining activities: emphasis on mitigation and remedial measures (ed Azcue, J.M.)," Springer, Heidelberg, pp. 1–3, 1999.

[52] K. Chopra, P. Prakash, S. Bhansali, A. Mathur. and P.K. Gupta, "Incidence and prevalence of silicotuberculosis in western Rajasthan: A retrospective study of three years," National Journal of Community Medicine, vol. 3, no. 1, pp. 161–163, 2012.

[53] J. Solanki, S. Gupta and S. Chand, "Oral health of stone mine workers of Jodhpur City, Rajasthan, India," Safety and health at work, vol. 5, no. 3, pp. 136–139, 2014.

[54] A. Yarahmadi, M.M. Zahmatkesh, M. Ghaffari, S. Mohammadi, Y. Labbafinejad, S.M. Seyedmehdi, M. Nojomi and M. Attarchi, "Correlation between silica exposure and risk of tuberculosis in Lorestan province of Iran," Tanaffos., vol. 12, no. 2, pp. 34–40, 2013.

[55] S.K. Prajapati, "Ecological effect of airborne particulate matter on plants," Environmental Skeptics and Critics., vol. 1, no. 1, pp. 12–22, 2012.

[56] R.E. Mittleman and C.V. Welti, "The fatal café coronary," JAMA, vol. 247, pp. 1285–1288, 1982.

[57] P.C. Elmes, "Inorganic dusts". In: P.A.B Raffle, P.H. Adams, P.J. Baxter, W.R. Lee (Ed.): "Hunter's Diseases of Occupations," Edward Arnold Publications, London, pp. 421–428, 1994.

[58] A.G. Leitch, "Functions of lungs". In: Anthony Seaton, Douglas Seaton, A Gordon Leitch (Eds.): "Rofton and Douglas's Respiratory Disease (5th Edition)," Oxford: Blackwell Science Ltd., vol. 1, pp. 43–46, 2000.

[59] K. Kimura, I. Nakano, Y. Ohtsuka, K. Okamoto, I. Usami, K. Onishi, T. Kishimoto, K. Genma, K. Mizuhashi, M. Sakatani and H. Kaji, "Today's occupational respiratory disease–From our recent investigations," Hokkaido Igaku Zasshi, vol. 85, no. 1, pp. 27–30, 2010.

[60] P.K. Sishodiya, "Silicosis–An Ancient Disease Providing Succour to Silicosis Victims, Lessons from Rajasthan Model," Indian Journal of Occupational and Environmental Medicine, vol. 26, no. 2, pp. 57–61, 2022.

[61] B.K. Sikand and S.P. Pamra, "Preliminary Report on the occurrence of Silicosis among Stone Masons Workers: In: Proceedings of 7th Tuberculosis Conference (1964)," Ind. J. Chest Diseases, vol. 6, no. 1, pp. 37–38, 1964.

[62] M.L. Mathur, "Silicosis among sand stone quarry workers of a desert district Jodhpur," Annals of the National Academy of Medical Sciences (India). vol. 32, pp. 113–118, 1996.

[63] S. Mazumder, "Mine safety analysis with a special focus on accidents due to explosives," Journal of Emerging Technologies and Innovative Research (JETIR), vol. 4, no. 11, pp. 128–133, 2017.

LRS Bianchi Type-I Cosmological Model in Modified *f(R, T)* Gravitation Theory filled with Perfect Fluid

Vijay G. Mete and Vishal M. Ingle[*]

Department of Mathematics, R.D.I.K & K.D. College, Badnera-444701, India

A B S T R A C T

This study explores LRS Bianchi Type-I space time filled with a perfect fluid within the framework of f(R,T) gravity, where R represents the Ricci scalar and T denotes the trace of the stress-energy momentum tensor. We analyze the simplest form of cosmic evolution in the context of general non-minimally coupled gravity models. Two specific models of f(R,T) gravity are considered. A time-dependent deceleration parameter is introduced, leading to an accelerated universe with an exact field solution. Additionally, we examine the kinematical and physical properties of the proposed models.

Keywords: LRS Bianchi type-I; f(R,T) gravity; Perfect fluid.

1. Introduction

It was made possible by the revolution in current cosmological understanding because of the observational cosmology research during the last two decades. Currently, the results of observational studies imply that the universe is growing more quickly than before [1-10]. Recent information provided by the Plank collaboration [11], Baryon Oscillation Spectroscopic Survey (BOSS) [12] and Atacama Cosmology Telescope Polarimeter (ACTPol) Collaboration [13] gives essential experimental data supporting that universe is in accelerated expansion stage. Moreover, the high red shift supernova experiments (HRSSE) [14,15] give clear indication that the indirect evidence for cosmic acceleration originates with observations like the cosmic microwave background (CMB) fluctuation [4] and large scale structure (LSS) [5].

There are two primary approaches for solving the challenge of cosmic acceleration. Introducing a cosmic component of dark energy is the first step and looks into its dynamic behavior and modifying general relativity is the second technique itself. Both strategies have unique elements as well as some serious theoretical issues. However, in this paper, our goal is to modify gravity, general relativity has seen various modifications in the last few decades.

Astrophysical measurements demonstrate that the universe is expanding rapidly due to an unusual form of energy accompanied by a strong negative pressure, known as dark energy, despite observational evidence. A tricky problem is still the character of dark energy in modern cosmology. The mysterious nature of dark energy is explained by modified theories of gravitation. Consequently, late time acceleration has been investigated by researchers and Dark energy can be investigated with modifying general relativity (GR) i.e. through modifying geometric part of Einstein–Hilbert action [16]. A highly successful strategy across them is this one to explore dark energy. The negative pressure created by "dark energy" and therefore causes the Universe to expand faster than the usual. Considering the Wilkinson Microwave Anisotropy Probe (WMAP) satellite

experiment, the dark energy occupies 73% of the matter in the universe is non-baryonic dark matter that fills up to 23% and regular baryonic (normal) matter occupy 4%. Cosmologists have postulated different types of dark energy candidates, including the cosmological constant, the Tachyon, the quintessence, the phantom, and others, to explain the observed data.

It's possible that modifying the Einstein-Hilbert action is going to be the best way to give an explanation how the cosmos has evolved. Among them, *f(R)* suggested a theory of gravity by Nojiri and Odintsov [17], a theory of gravity is remarkable. *f (R, T)* modified theory of gravity was recently created by Harko *et al.* [18], where the stress-energy tensor's trace *T* and Ricci scalar *R's* arbitrary function *R* yield the gravitational Lagrangian. In addition, for test particles the equations of motion, have the metric formalism's equations for the gravitational field, which result from the stress-energy tensor's covariant divergence.

Now, taking into account metric-dependent Lagrangian density, according to the following, the relevant gravity field equations are obtained with the Hilbert-Einstein variations principle. The action in light of *f(R,T)* theory of gravity is

$$S = \int \left(\frac{1}{16\pi G} f(R,T) + L_m \right) \sqrt{-g}\, d^4 x \qquad (1)$$

Here L_m this is the usual matter Lagrangian density of matter source, a random function of Ricci scalar *R* & the trace *T* of the energy–momentum tensor T_{ij} the origin of the matter is $f(R,T)$, the determinant of the metric tensor g_{ij} is g. The energy–momentum tensor T_{ij} with the Lagrangian matter is outlined in such a manner and $T = g^{ij} T_{ij}$ is its trace, Here, matter Lagrangian L_m relies only on the metric tensor component g_{ij} in place of its derivatives this is we considered here, Hence, we secure

$$T_{ij} = -\frac{2}{\sqrt{-g}} \frac{\delta(\sqrt{-g}\, L_m)}{\delta g^{\mu\nu}} \qquad (2)$$

$$T_{ij} = g_{ij}L_m - \frac{\partial L_m}{\partial g^{ij}} \qquad (3)$$

The *f(R, T)* gravitation field's equations are acquired by varying the action *S* in relation to metric tensor ($g_{\mu\nu}$).

$$f_R(R,T)R_{ij} - \frac{1}{2}f(R,T)g_{ij} + [g_{ij}\nabla^i\nabla_i - \nabla_i\nabla_j]f_R(R,T) \qquad (4)$$
$$= 8\pi T_{ij} - f_T(R,T)T_{ij} - f_T(R,T)\theta_{ij}$$

here

$$f_R = \frac{\delta f(R,T)}{\delta R}, f_T = \frac{\delta f(R,T)}{\delta T}, \Theta_{ij} = g^{\alpha\beta}\frac{\delta T_{\alpha\beta}}{\delta g^{ij}}.$$

Here ∇ referred as the covariant derivative also T_{ij} are usual matter energy-momentum tensor obtained from the Lagrangian L_m. It is stated here that the physical properties of the matter field are determined by field equations. Numerous theoretical frameworks that represent various contributions of matter for *f(R, T)* gravitational potential; But Still, Harko*et al.*[18] provided three classes for these models $f(R,T) = f_1(R) + f_2(T)$.

$$f(R,T) = \begin{cases} R + 2f(T), \\ f_1(R) + f_2(T), \\ f_1(R) + f_2(R)f_3(T) \end{cases} \qquad (5)$$

Separate equation of field for different models of $f(R,T)$ gravitation is presented as

1. $f(R,T) = R + 2f(T)$

$$R_{ij} - \frac{1}{2}Rg_{ij} = 8\pi T_{ij} - 2f'(T)T_{ij} - 2f'(T)\theta_{ij} + f(T)g_{ij} \qquad (6)$$

2. $f(R,T) = f_1(R) + f_2(T)$

$$f_1'(R)R_{ij} - \frac{1}{2}f_1(R)g_{ij} + [g_{ij}\nabla^i\nabla_i - \nabla_i\nabla_j]f_1'(R) = \qquad (7)$$

$$8\pi T_{ij} - f_2'(T)T_{ij} - f_2'(T)\theta_{ij} + \frac{1}{2}f_2(T)g_{ij}$$

If $L_m = p$ then $\theta_{ij} = -2T_{ij} - pg_{ij}$ (8)

The selection of the *f (R, T)* model affects the outcome, as is evident. In order to meaningfully depict our results, we must therefore select a workable *f(R, T)* model. The possibly cosmological criteria within *f(R)* theory, which characterizes the dark energy models, have been addressed by Nojiri and Odintsov [19]. The model that Sharif and Zubair [20] have chosen for us to discuss

$$f(R,T) = \alpha_1 R^m T^n + \alpha_2 T(1 + \alpha_3 T^p R^q) \qquad (9)$$

Whereas *m, n, p,* and *q* are assumed to have values higher than or equal to 1. We will examine our findings in light of various applications of the above model, and we'll concentrate our subsequent discussion on the next three scenarios.

$$f(R,T) = \alpha_1 R + \alpha_2 T + \alpha_4 T^2 \ for$$
$$m = 1, n = 0, \alpha_4 = \alpha_1\alpha_3, p = 1, q = 0 \qquad (10)$$

$$f(R,T) = R + \alpha_2 T \ for \ \alpha_1 = 1, m = 1, n = 0, \alpha_3 = 0 \quad (11)$$

$$f(R,T) = \alpha_1 R + \alpha_2 T(1 + \alpha_3 T \ R^2) \qquad (12)$$

Making use of equations (6), (7) and (8) in conjunction with the (10), (11) and (12), we have

Model-I:- $f(R,T) = \alpha_1 R + \alpha_2 T + \alpha_4 T^2 \ for$
$$m = 1, n = 0, \alpha_4 = \alpha_1\alpha_3, p = 1, q = 0 \ is$$

$$R_{ij} - \frac{1}{2}Rg_{ij} =$$
$$\frac{8\pi}{\alpha_1}T_{ij} + \left[\frac{\alpha_2}{\alpha_1} + 2\alpha_3 T\right][T_{ij} + pg_{ij}] + \frac{1}{2}\left[\frac{\alpha_2}{\alpha_1}T + \alpha_3 T^2\right]g_{ij} \qquad (13)$$

Model-II:- $f(R,T) = R + \alpha_2 T \ for \ \alpha_1 = 1, m = 1, n = 0, \alpha_3 = 0$

$$R_{ij} - \frac{1}{2}Rg_{ij} = [8\pi + \alpha_2]T_{ij} + \left[p\alpha_2 + \frac{1}{2}\alpha_2 T\right]g_{ij} \qquad (14)$$

So many scientists created cosmological models with perfect fluid substance explore the universe's accelerated expansion. Most recently discoveries show that the universe is expanding more quickly than predicted by the negative pressure caused by an unidentified type of energy i.e. named as dark energy. Due to this, we have to build a cosmological model of the accelerating universe lacking consideration for account of dark energy or dark matter, even though also selecting the greatest trustworthy matter component. As a result, the literature has extensively studied numerous cosmological models that include fluid with viscosity in the early universe [21, 22]. Also most of the researcher have studied on *f(T), f(R,T)* gravity [23, 24].

The current document is structured as follows: In Section 2, in this part we extract the exact solutions to one of the instances where *f(R,T)* gravity by using methodology [22]. The perfect fluid model offers a sophisticated explanation of matter behavior, distinguished by its pressure and energy density. It is a perfect fit for our study due of its adaptability and suitability for a variety of physical environments. Regarding the time-varying DP-supported spatially homogeneous anisotropic Bianchi Type-I space-time the bulk viscous pressure, bulk viscous coefficient, energy density, matter trace, Ricci scalar, and energy conditions are obtained. Section 3 & 4 presents the physical properties of both models.

2. Metric, Field Equations Solutions

Cosmological models of the Bianchi type are significant because they are homogenous and anisotropic, providing a framework for studying the universe's isotropization throughout time. Furthermore, anisotropic universes are more general than isotropic models from a theoretical perspective. Bianchi space times are helpful in building models of spatially homogenous &anisotropic cosmologies because of the ease of solving an field equations with their relative simplicity.

The LRS Bianchi Type-I line element is

$$ds^2 = -dt^2 + A^2 dx^2 + B^2(dy^2 + dz^2) \qquad (15)$$

However, A &B are the scale factors with function of cosmic time *t* only.

The stress energy tensor of matter is taken to be

$$T_{ij} = (p + \rho)u_i u_j + pg_{ij} \qquad (16)$$

Whereas $u_i = (0,0,0,1)$ is the four-velocity vector in co-moving coordinate system satisfying $u_i u_j = -1$.

2.1 Model-I

$$f(R,T) = \alpha_1 R + \alpha_2 T + \alpha_4 T^2 \text{ for}$$
$$m = 1, n = 0, \alpha_4 = \alpha_1 \alpha_3, p = 1, q = 0$$

From (13) and (15) field equation obtained as

$$\frac{2\ddot{B}}{B} + \frac{\dot{B}^2}{B^2} = X_1 p + X_2 p^2 + X_3 p\rho + X_4 \rho + X_5 \rho^2 \quad (17)$$

$$\frac{\ddot{A}}{A} + \frac{\ddot{B}}{B} + \frac{\dot{A}\dot{B}}{AB} = X_1 p + X_2 p^2 + X_3 p\rho + X_4 \rho + X_5 \rho^2 \quad (18)$$

$$\frac{2\dot{A}\dot{B}}{AB} + \frac{\dot{B}^2}{B^2} = Y_1 p + Y_2 p^2 + Y_3 p\rho + Y_4 \rho + Y_5 \rho^2 \quad (19)$$

Where dot (.) indicate the derivative with to t and

$$X_1 = \frac{8\pi}{\alpha_1} + \frac{7\alpha_2}{2\alpha_1}, X_2 = \frac{33\alpha_3}{2}, X_3 = -7\alpha_3, X_4 = -\frac{\alpha_2}{2\alpha_1}, X_5 = \frac{\alpha_3}{2} \quad (20)$$

$$Y_1 = \frac{5\alpha_2}{2\alpha_1}, Y_2 = \frac{21\alpha_3}{2}, Y_3 = -11\alpha_3 \; Y_4 = -\frac{8\pi}{\alpha_1} - \frac{3\alpha_2}{2\alpha_1} \; Y_5 = \frac{5\alpha_3}{2} \quad (21)$$

$$\frac{2\ddot{B}}{B} + \frac{2\dot{A}\dot{B}}{AB} + \frac{2\dot{B}^2}{B^2} = (X_1 + Y_1)p + (X_2 + Y_2)p^2 + \qquad (22)$$
$$(X_3 + Y_3)p\rho + (X_4 + Y_4)\rho + (X_5 + Y_5)\rho$$

$$\frac{\ddot{A}}{A} + \frac{\ddot{B}}{B} + \frac{3\dot{A}\dot{B}}{AB} + \frac{\dot{B}^2}{B^2} = (X_1 + Y_1)p + (X_2 + Y_2)p^2 \qquad (23)$$
$$+ (X_3 + Y_3)p\rho + (X_4 + Y_4)\rho + (X_5 + Y_5)\rho$$

Equating (22) and (23) we obtain

$$\frac{\ddot{B}}{B} + \frac{\dot{B}^2}{B^2} - \frac{\dot{A}\dot{B}}{AB} - \frac{\ddot{A}}{A} = 0 \qquad (24)$$

The expansion scalar relation is proportional to the shear scalar, resulting in

$$A = B^n \qquad (25)$$

Using (25) in (24) we have the equation

$$\frac{\ddot{B}}{B} + (1 + n)\frac{\dot{B}^2}{B^2} = 0 \qquad (26)$$

Assume $\dot{B} = G(B)$ then equation (26) is

$$\frac{dG}{dB} + (1 + n)G = 0 \qquad (27)$$

This is the linear differential equation in G, which leads the solution

$$G = k_1 e^{-(1+n)B} \qquad (28)$$

Where k_1 the constant of integration, hence is the solution is obtained as

$$ds^2 = -\left(\frac{dt}{dB}\right)^2 dB^2 + B^{2n}dx^2 + B^2(dy^2 + dz^2) \qquad (29)$$

This is written as

$$ds^2 = -k^2{}_1 e^{2(1+n)B}dB^2 + B^{2n}dx^2 + B^2(dy^2 + dz^2) \quad (30)$$

Now using transformation $B = \tilde{T}$, $x = \tilde{X}$, $y = \tilde{Y}$ and $z = \tilde{Z}$, eq. (30) takes the form

$$ds^2 = -k^2{}_1 e^{2(1+n)\tilde{T}}d\tilde{T}^2 + \tilde{T}^{2n}d\tilde{X}^2 + \tilde{T}^2(d\tilde{Y}^2 + d\tilde{Z}^2) \qquad (31)$$

From (31) we have

$$A = \tilde{T}^n \text{ and } B = \tilde{T} \qquad (32)$$

The average Hubble parameter obtained as

$$H = \frac{1}{3}(\frac{\dot{A}}{A} + 2\frac{\dot{B}}{B}) = \frac{k_1(n+2)}{3}\frac{e^{-(1+n)\tilde{T}}}{\tilde{T}} \qquad (33)$$

Expansion scalar is obtained as

$$\theta = 3H = k_1(n+2)\frac{e^{-(1+n)\tilde{T}}}{\tilde{T}} \qquad (34)$$

The value of deceleration parameter will be

$$q = \frac{d}{d\tilde{T}}\left(\frac{1}{H}\right) - 1 = \frac{3e^{(1+n)\tilde{T}}[\tilde{T}(1+n)+1] - k_1(n+2)}{k_1(n+2)} \qquad (35)$$

The average scale factor is

$$a = AB^2 = \tilde{T}^{n+2} \qquad (36)$$

Shear scalar is obtained as

$$\sigma^2 = \frac{1}{2}\left(H_x^2 + H_y^2 + H_z^2 - \frac{\theta^2}{3}\right) = \frac{k_1{}^2(n-1)^2}{3}e^{-2(1+n)\tilde{T}} \quad (37)$$

To solve field equation now we consider relation

$$p = \omega\rho \qquad (38)$$

From (22) and (38), we get

$$\frac{2\ddot{B}}{B} + \frac{2\dot{A}\dot{B}}{AB} + \frac{2\dot{B}^2}{B^2} = T_1 \rho^2 + T_2 \rho \qquad (39)$$

Where

$$T_1 = (X_2 + Y_2)\omega^2 + (X_3 + Y_3)\omega + (X_5 + Y_5),$$
$$T_2 = (X_1 + Y_1)\omega + (X_4 + Y_4) \qquad (40)$$

Then from (20) & (21) equation (40)

$$T_1 = 24\alpha_3\omega^2 - 11\alpha_3\omega + 3\alpha_3,$$
$$T_2 = \left[\frac{8\pi}{\alpha_1} + \frac{6\alpha_2}{\alpha_1}\right]\omega - \left[\frac{8\pi}{\alpha_1} + \frac{2\alpha_2}{\alpha_1}\right] \qquad (41)$$

Now put value of A and B from eq. (32) in eq. (39) we get

$$T_1 \rho^2 + T_2 \rho - \frac{2k_1{}^2(n+1)(1-\tilde{T})e^{-2(1+n)\tilde{T}}}{\tilde{T}^2} = 0 \qquad (42)$$

Equation obtained in (42) is quadratic equation in ρ then by [22]

$$\rho = \frac{-T_2\tilde{T} \pm \left[T_2{}^2\tilde{T}^2 + 8T_1 k_1{}^2(n+1)(1-\tilde{T})e^{-2(1+n)\tilde{T}}\right]^{1/2}}{2T_1\tilde{T}} \qquad (43)$$

$$p = \omega \frac{-T_2\tilde{T} \pm \left[T_2{}^2\tilde{T}^2 + 8T_1k_1{}^2(n+1)(1-\tilde{T})e^{-2(1+n)\tilde{T}} \right]^{1/2}}{2T_1\tilde{T}} \qquad (44)$$
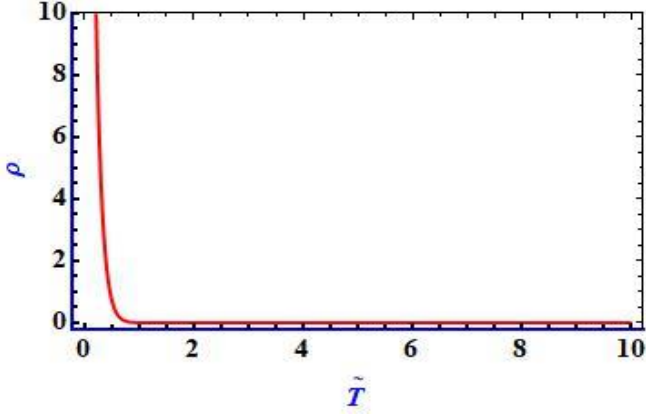
Fig.1. Variation of energy density against $\tilde{T}$ for $k_1 = 5$, $n = 1.5$, $T_1 = 1$, $T_2 = 5$
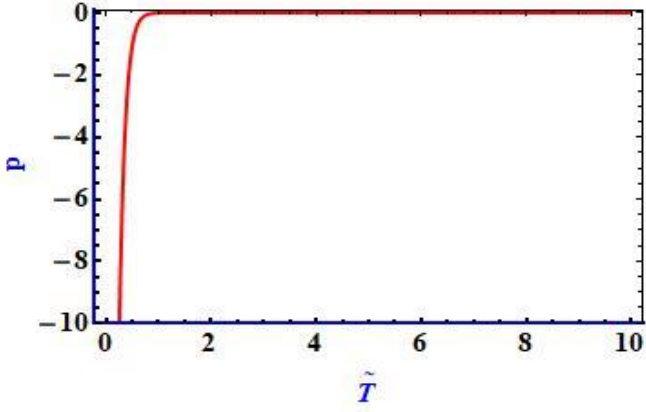
Fig. 2. Variation of pressure against $\tilde{T}$ for $k_1 = 5$, $n = 1.5$, $T_1 = 1$, $T_2 = 5$

2.2 Model-II

$f(R,T) = R + \alpha_2 T$ for $\alpha_1 = 1$, $m = 1, n = 0$, $\alpha_3 = 0$.

Using equations (14) and (15), the field equations are obtained as

$$\frac{2\ddot{B}}{B} + \frac{\dot{B}^2}{B^2} = [8\pi + \frac{7}{2}\alpha_2]p - \frac{1}{2}\alpha_2\rho \qquad (45)$$

$$\frac{\ddot{A}}{A} + \frac{\ddot{B}}{B} + \frac{\dot{A}\dot{B}}{AB} = [8\pi + \frac{7}{2}\alpha_2]p - \frac{1}{2}\alpha_2\rho \qquad (46)$$

$$\frac{2\dot{A}\dot{B}}{AB} + \frac{\dot{B}^2}{B^2} = \frac{5}{2}\alpha_2 p - [8\pi + \frac{3}{2}\alpha_2]\rho \qquad (47)$$

Here dot represents derivatives with respect to time

In order to resolve the above field equations, we have proceeded in the same manner as describe in Model-I

Now from equation (45) to (47) and (38) we have the equation

$$\frac{2\ddot{B}}{B} + \frac{2\dot{A}\dot{B}}{AB} + \frac{2\dot{B}^2}{B^2} = [(8\pi + 6\alpha_2)\omega - (8\pi + 2\alpha_2)]\rho \qquad (48)$$

In this model, by [22] the energy density and pressure are given as
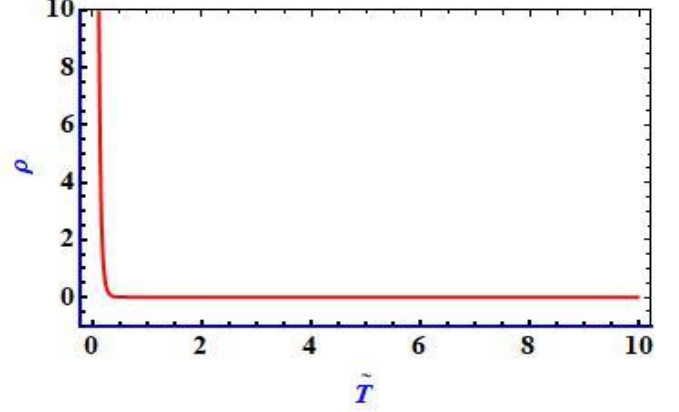
Fig.3. Variation of energy density against $\tilde{T}$ for $k_1 = 2.5$, $n = 5$, $\alpha_2 = 15$, $\omega = 1.5$
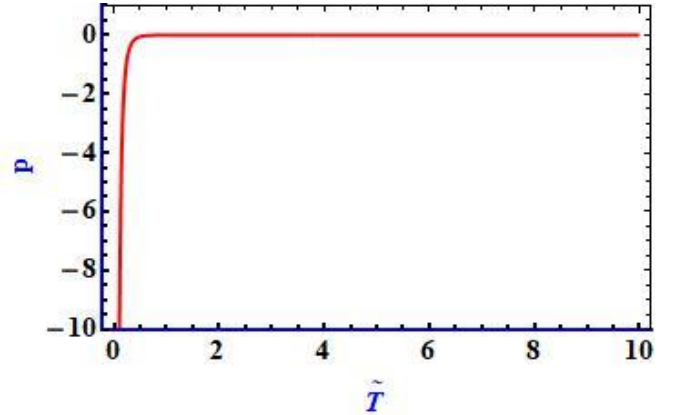
Fig. 4. Variation of pressure against $\tilde{T}$ for $k_1 = 2.5$, $n = 5$, $\alpha_2 = -15$, $\omega = 1.5$

$$\rho = \frac{2k_1{}^2(n+1)(1-\tilde{T})e^{-2(1+n)\tilde{T}}}{\{(8\pi + 6\alpha_2)\omega - (8\pi + 2\alpha_2)\}\tilde{T}^2} \qquad (49)$$

$$p = \frac{\omega 2k_1{}^2(n+1)(1-\tilde{T})e^{-2(1+n)\tilde{T}}}{\{(8\pi + 6\alpha_2)\omega - (8\pi + 2\alpha_2)\}\tilde{T}^2} \qquad (50)$$

3. State Finder Diagnostic

The state-finder pair {r, s} is characterized as

$$r = 1 + \frac{3\dot{H}}{H^2} + \frac{\ddot{H}}{H^3}, \qquad s = \frac{r-1}{3(q - \frac{1}{2})} \qquad (51)$$

The state-finder pair is diagnostic parameter in geometrical that is directly derived from a space-time metric also has more universal than physical variables because physical variables rely upon the properties of physical fields that define DE.

The state-finder parameter values regarding our examples are

$$r = 1 - \frac{9\tilde{T}^2}{k_1(n+2)}\left\{\frac{1}{\tilde{T}^2} + \frac{(1+n)}{\tilde{T}}\right\}e^{(1+n)\tilde{T}}$$
$$+ \frac{9\tilde{T}^3}{k_1^2(n+2)^2}\left\{\frac{2}{\tilde{T}^3} + \frac{2(1+n)}{\tilde{T}^2} + \frac{(1+n)^2}{\tilde{T}}\right\}e^{2(1+n)\tilde{T}} \tag{52}$$

$$s = \frac{-9\tilde{T}^2\left\{\frac{1}{\tilde{T}^2} + \frac{(1+n)}{\tilde{T}}\right\}e^{(1+n)\tilde{T}}k_1(n+2) + }{9\tilde{T}^3\left\{\frac{2}{\tilde{T}^3} + \frac{2(1+n)}{\tilde{T}^2} + \frac{(1+n)^2}{\tilde{T}}\right\}e^{2(1+n)\tilde{T}}}{3e^{k_1(n+2)}\{3e^{(1+n)\tilde{T}}[\tilde{T}(1+n)+1] - \frac{3}{2}k_1(n+2)\}} \tag{53}$$

4. Physical Interpretation of Graph

Fig. 1 shows that for Model-I, As $\tilde{T}$ goes on, the universe's energy density decreases and eventually tends to a constant value 0.1, $\rho \to 0$ as $\tilde{T} \to +\infty$ .and values of density goes to infinite as $\tilde{T}$ tends to zero i.e. $\rho \to +\infty$ as $\tilde{T} \to 0$ so range of ρ is $(0,\infty)$. When it comes to pressure by Fig. 2, it is an increasing function of $\tilde{T}$ and takes the negative values throughout cosmic evolution $p \to -\infty$ as $\tilde{T} \to 0$ and $p \to 0$ as $\tilde{T} \to +\infty$ It starts with extremely high negative values both initially and ultimately gets closer to zero and range of p is $(-\infty, 0)$. Recent observations have demonstrated that the Universe is accelerating, and the negative pressure supports this phase and our model.

For Model–II Fig. 3 shows that, a decaying function of time describes the energy density of the universe along with eventually approaches a constant value. i.e.$\tilde{T} \to \infty$ as $\rho \to -0.4$ it will goes very close to y-axis as $\tilde{T} \to 0$ & Range interval of the density is $(-0.5,\infty)$ and from Fig. 4 pressure is increasing function takes the negative values throughout cosmic evolution and range set of the pressure is $(-\infty, 0.1)$

Conclusion

In this study, we analyzed the LRS Bianchi Type-I cosmological model within the framework of f(R,T) gravity, considering a perfect fluid as the cosmic source. Two specific f(R,T) models were explored, leading to exact solutions of the modified Einstein field equations under the assumption of a time-dependent deceleration parameter. Various cosmological parameters, including the deceleration parameter, were examined.

By adopting a special law of variation for the Hubble parameter and deceleration parameter, we derived solutions that describe the evolution of the universe. Notably, our results indicate that the deceleration parameter remains negative across all datasets, providing strong evidence that

the universe is undergoing accelerated expansion, with the acceleration becoming progressively stronger over time.

References

[1] A.G. Riess, A.V. Filippenko, P. Challis, A. Clocchiatti, A. Diercks, P.M. Garnavich, and J. Tonry, "Observational evidence from supernovae for an accelerating universe and a cosmological constant,"*The Astronomical Journal*, vol. 116, no. 3, pp. 1009, 1998.

[2] S. Perlmutter, G. Aldering, G. Goldhaber, R.A. Knop, P. Nugent, P.G. Castro, S. Deustua, S. Fabbro, A. Goobar, D.E. Groom and I.M. Hook, "Measurements of Ω and Λ from 42 high-redshift supernovae," *The Astrophysical Journal*, vol. 517, no. 2, pp. 565, 1999.

[3] A.G. Riess, R.P. Kirshner, B.P. Schmidt, S. Jha, P. Challis, P.M. Garnavich, and P. Zhao, "BVRI light curves for 22 type Ia supernovae," *The Astronomical Journal*, vol. 117, no. 2, pp. 707, 1999.

[4] D.N. Spergel, L. Verde, H.V. Peiris, E. Komatsu, M.R. Nolta, C.L. Bennett, and E.L. Wright, "First-year Wilkinson Microwave Anisotropy Probe (WMAP) observations: determination of cosmological parameters," *The Astrophysical Journal Supplement Series*, vol. 148, no. 1, pp. 175, 2003.

[5] M. Tegmark, M.A. Strauss, M. R. Blanton, K. Abazajian, S. Dodelson, H. Sandvik, and D.G. York, "Cosmological parameters from SDSS and WMAP," *Physical Review D*, vol. 69, no. 10, pp. 103501, 2004.

[6] K. Abazajian, J.K. Adelman-McCarthy, M.A. Agüeros, S.S. Allam, K.S. Anderson, S.F. Anderson, J. Annis, N.A. Bahcall, I.K. Baldry, S. Bastian and A. Berlind "The second data release of the Sloan Digital Sky Survey*," The Astronomical Journal*, vol. 128, no. 1, pp. 502, 2004.

K. Abazajian, J.K. Adelman-McCarthy, M.A. Agüeros, S.S. Allam, K. S. Anderson, S.F. Anderson, J. Annis, N.A. Bahcall, I.K. Baldry, S. Bastian and A. Berlind, "The third data release of the Sloan Digital Sky Survey," *The Astronomical Journal*, vol. 129, no. 3, pp. 1755, 2005.

[7] D.N. Spergel, R. Bean, O. Doré, M.R. Nolta, C.L. Bennett, J. Dunkley, G. Hinshaw, N.E. Jarosik, E. Komatsu, L. Page and H.V. Peiris,"Three-year Wilkinson Microwave Anisotropy Probe (WMAP) observations: implications for cosmology," *The Astrophysical Journal Supplement Series*, vol. 170, no. 2, pp. 377, 2007.

[8] E. Komatsu, J. Dunkley, M.R. Nolta, C.L. Bennett, B. Gold, G. Hinshaw, N. Jarosik, D. Larson, M. Limon, L.E.A. Page and D.N. Spergel, "Five-year Wilkinson Microwave Anisotropy Probe (WMAP) observations: cosmological interpretation," *The Astrophysical Journal Supplement Series*, vol. 180, no. 2, pp. 330, 2009.

[9] D. Larson, J. Dunkley, G. Hinshaw, E. Komatsu, M.R. Nolta, C.L. Bennett, B. Gold, M. Halpern, R.S. Hill, N. Jarosik and A. Kogut "Seven-year Wilkinson Microwave Anisotropy Probe (WMAP) observations: power spectra and WMAP-derived parameters," *The Astrophysical Journal Supplement Series*, vol. 192, no. 2, pp. 16, 2011.

[10] P.A. Ade, N. Aghanim, M. Arnaud, M. Ashdown, J. Aumont, C. Baccigalupi, and S. Matarrese, "Planck 2015 results-XIII. Cosmological parameters," *Astronomy & Astrophysics*, vol. 594, pp. A13, 2016.

[11] S. Alam, M. Ata, S. Bailey, F. Beutler, D. Bizyaev, J.A. Blazek, and G.B. Zhao, "The clustering of galaxies in the completed SDSS-III Baryon Oscillation Spectroscopic Survey: cosmological analysis of the DR12 galaxy sample," *Monthly Notices of the Royal Astronomical Society*, vol. 470, no. 3, pp. 2617-2652, 2017.

[12] S. Naess, M. Hasselfield, J. McMahon, M.D. Niemack, G.E. Addison, P.A. Ade, R. Allison, M. Amiri, N. Battaglia, J.A. Beall and F. De Bernardis, "The Atacama Cosmology Telescope: CMB polarization at 200<ℓ<9000," *Journal of Cosmology and Astroparticle Physics*, vol. 2014, no. 10, pp. 007, 2014.

[13] A.G. Riess, L.G. Strolger, J. Tonry, S. Casertano, H.C. Ferguson, B. Mobasher, and Z. Tsvetanov, "Type Isupernova discoveries at z > 1 from the Hubble Space Telescope: Evidence for past deceleration and constraints on dark energy evolution," *The Astrophysical Journal*, vol. 607, no. 2, pp. 665, 2004.

[14] C.L. Bennett, R.S. Hill, G. Hinshaw, M.R. Nolta, N. Odegard, L. Page, and E. Wollack, "First-year Wilkinson Microwave Anisotropy Probe (WMAP) observations: foreground emission," *The Astrophysical Journal Supplement Series*, vol. 148, no. 1, pp. 97, 2003.

[15] A. Jakubiec and J. Kijowski, "On the Cauchy problem for the theory of gravitation with nonlinear Lagrangian," *Journal of Mathematical Physics*, vol. 30, no. 12, pp. 2923-2924, 1989.

[16] S.I. Nojiri and S.D. Odintsov, "Modified gravity with negative and positive powers of curvature: Unification of inflation and cosmic acceleration," *Physical Review D*, vol. 68, no. 12, pp. 123512, 2003.

[17] T. Harko, F.S. Lobo, S.I. Nojiri, and S. D. Odintsov, "*f (R, T)* gravity," *Physical Review D*, vol. 84, no. 2, pp. 024020, 2011.

[18] S.I. Nojiri and S.D. Odintsov, "Introduction to modified gravity and gravitational alternative for dark energy," *International Journal of Geometric Methods in Modern Physics*, vol. 4, no. 1, pp. 115-145, 2007.

[19] M. Sharif and M. Zubair, "Cosmological reconstruction and stability in f (R, T) gravity," *General Relativity and Gravitation*, vol. 46, no. 6, pp. 1723, 2014.

[20] Y.S. Solanke, D.D. Pawar, and V.J. Dagwal, "Accelerating dark energy universe with LRS Bianchi Type-I space-time," *International Journal of Geometric Methods in Modern Physics*, vol. 18, no. 4, pp. 2150062, 2021.

[21] G.P. Singh, B.K. Bishi, and P.K. Sahoo, "Cosmological constant Λ in f (R, T) modified gravity," *International Journal of Geometric Methods in Modern Physics*, vol. 13, no. 5, pp. 1650058, 2016.

[22] V.G. Mete, V.M. Ingle, and A.T. Valkunde, "LRS Bianchi Type-I Cosmological Model in Modified f (R, T)," *Prespacetime Journal*, vol. 14, no. 6, 2023.

[23] V.G. Mete, P.S. Dudhe, and V.M. Ingle, "Bianchi Type-I Cosmological Model with Perfect Fluid in Modified f (T) Gravity," *Journal of Scientific Research*, vol. 15, no. III, pp. 571-581, 2023.

Assessment of Spring Distribution across Pakistan: Implications for Water Security

Ghani Akbar* and Muhammad Bilal Iqbal

Climate, Energy and Water Research Institute (CEWRI), National Agricultural Research Centre (NARC), Park Road, Chak Shahzad Islamabad, Pakistan

A B S T R A C T

Springs play a vital role in Pakistan's water security, particularly in remote regions where they serve as a lifeline for agriculture, livestock, and domestic needs. However, increased pressure on spring resources from climate change, population growth, deforestation, and land degradation has significantly declined their availability. Springs have been largely overlooked in both research and policy formulation in Pakistan. This study assesses the distribution and status of springs across Pakistan's main provinces and regions. Focusing on the springs data from the 2023 Survey of Pakistan, along with population data from the 2023 census and climatic data from the nearest stations of Pakistan Meteorological Department, this study maps the spatial distribution of springs and examines the influence of environmental parameters, such as rainfall, temperature, elevation, and slope on their existence. The findings highlight that 81% of the nation's springs are concentrated in Khyber Pakhtunkhwa (KP) and Baluchistan provinces, with substantial regional dependency on these resources. The Hindu Kush Himalaya (HKH) region of Pakistan host 5051 springs (28%) for the 21 million people in Pakistan. Approximately 114 million people live in 108 spring districts with an average of 26,252 persons per spring, while the average spring density is around three springs per hectare. Through province-level mapping, this study underscores the urgent need for sustainable policies to conserve springs and improve water security. This study emphasized on the need for sustainable water management policies and their urgent field implementation that prioritize spring conservation and adaptation to climate change impacts.

Keywords: Springs, Climate Change, Water Security, Pakistan, Livelihoods

1. Introduction

Springs are natural discharge points of groundwater [1] and are essential water sources, particularly in rural, hilly and mountainous regions of Pakistan. These springs, which emerge from underground aquifers, are critical for sustaining communities in high-altitude, remote and semi-arid areas, where alternative water sources are limited. Pakistan's diverse climate and topography, ranging from the arid plains of Sindh and Baluchistan to the mountainous regions of Khyber Pakhtunkhwa (KP), Gilgit-Baltistan (GB), and Azad Jammu and Kashmir (AJ&K), makes springs a crucial water resource, especially in areas with limited water availability. In KP, AJ&K, and GB, spring-fed gravity water channels built on contour lines, known as the Kuhl irrigation system, are vital for agriculture and domestic use, particularly where canal irrigation is impractical due to challenging terrain [2]. Springs are also important for sustaining agriculture, ecology, and livelihoods in these regions, playing a pivotal role in balancing the hydrological cycle and replenishing aquifers to ensure sustainable water availability.

The sustainability of springs has been largely threatened by climate change [3, 4], with its impacts particularly more evident in northern Pakistan. Key climate change factors, including unpredictable and extreme rainfall patterns, rising temperatures, land degradation, urbanization, and glacier retreat, have disrupted the recharge of aquifers that feed springs [5]. These trends also mirror global observations in the Hindu Kush-Himalayan (HKH) region, where traditional spring-based water supply systems are also being affected by climate change [3, 6]. The combined impacts of glacier retreat and frequent droughts are severely impacting spring water availability, particularly in the Malakand and Hazara regions. As a result, the livelihoods of spring-dependent communities, and livestock survival, are increasingly threatened [7].

The HKH region in northern Pakistan in particular, encompassing GB and KP, is home to numerous springs that serve as the primary water source for human, animal, and agricultural needs. The construction and maintenance of spring-fed Kuhl irrigation channels rely on traditional knowledge and community involvement [7]. However, this system faces numerous challenges, including the direct diversion of spring water through pipes for household use, frequent damage to channels from climate change-induced storms and flooding, and the growing use of deep tubewells, which has led to the drying up of springs in some areas. These issues threaten ecosystems downstream, hinder agricultural productivity, and undermine the livelihoods of communities reliant on spring-fed water systems [8]. Moreover, changing weather patterns, such as altered snowmelt timing and shifting monsoon rainfall, causes variability in spring flows, further affecting water security for both humans and livestock.

Water quality is another critical concern that negatively impacts the health and well-being of spring-dependent communities [9-12]. Poor water quality is often attributed to mismanagement of spring catchment areas, including deforestation, land-use changes, and urbanization, which reduce water infiltration, increase surface runoff, and increase water pollution particularly in KP and Punjab [13]. The chemical composition of spring water is influenced by both human activities involving untreated sewage disposal and natural processes, such as the mineralization of rocks [14, 15]. In KP and AJ&K, deforestation and rock drilling for groundwater extraction through deep tubewells pose significant challenges to both the quality and quantity of spring water. The loss of ground cover due to deforestation reduces the land's ability to absorb and retain water,

---

*Corresponding author: ghani_akbar@hotmail.com

leading to increased runoff, soil erosion, and land degradation, which further compromises spring sustainability [16].

Despite the growing importance of springs for water security and livelihoods, the management of springs has been largely neglected in Pakistan's water, climate, and food security policies. This highlights the urgent need for targeted research and policy interventions to safeguard these vital resources. This study aims to address this gap by undertaking the first comprehensive assessment of spring distribution across Pakistan and analyzing their correlation with environmental variables such as rainfall, temperature, elevation, and slope. By providing a detailed understanding of spring distribution and the population's dependency on these water sources, this research seeks to inform researchers, policymakers and planners, guiding the development of future programs to conserve and manage these critical water resources effectively.

2.   Materials and Methods

2.1   Study Area

This study area is comprised of KP, Punjab, Sindh, Baluchistan, AJ&K, GB, Islamabad capital territory and the HKH region that fall in Pakistan. The study area represents variable topographies, from the mountainous north to the plains of Sindh and Punjab, providing a wide range of geographical and climatic conditions. All these factors may influence the distribution and occurrence of springs.

2.2   Data Collection

The data of springs distribution across the country was obtained from the Survey of Pakistan recorded during 2023. The weather and geographical information comprising (rainfall, temperature, elevation, and slope) were obtained from the Pakistan Meteorological Department (PMD) and other online resources. Population data from the 2023 census was used to calculate spring dependency rates for the various districts. The spatial analysis of spring distribution was conducted using Geographic Information System (GIS) software to generate maps for each province.

2.3   Statistical Analysis

To assess the distribution of springs across Pakistan, the total number of springs along with relevant climatic and geographical data for spring-bearing districts in each province was compiled into an Excel spreadsheet (2021). The statistical analysis aimed to establish the relationship between the number of springs in each district (dependent variable) and selected climatic and topographic parameters (independent variables).

A correlation and regression analysis was performed to quantify the influence of climatic and geographical factors on spring distribution. The statistical model was set at a 95% confidence level, and the correlation coefficient (r), coefficient of determination (R^2), and significance level (p-value) were computed using built-in statistical functions in Microsoft Excel. The strength and direction of associations between variables were assessed using Pearson's correlation coefficient (r), while the predictive capability of independent variables was evaluated through linear regression analysis.

The computed values of r, R^2, and p were systematically presented in tabular form to illustrate the statistical relationships between spring availability and climatic and geographical parameters. The significance of these relationships was interpreted based on conventional statistical thresholds ($p < 0.05$ for statistical significance).

3.   Results

3.1   Overview of Spring Distribution

The results indicate substantial variation in spring distribution across Pakistan, as given in Figure 1. Our analysis identified 18,114 springs across Pakistan, with approximately 81% located in KP and Baluchistan, highlighting significant clustering in regions with favorable climatic and geographic conditions. Lower elevation and arid regions, such as southern Punjab and Sindh, showed limited spring presence. On average, about 26,225 people rely on each spring in the 108 spring bearing districts containing springs, underscoring the critical role these resources play in regional water security.
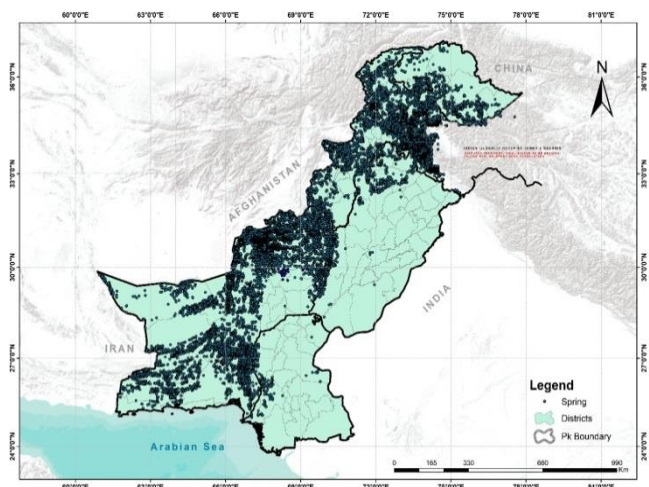
Fig. 1: Spatial distribution of springs across Pakistan

Table 1 presents a summary of the total number of districts, total number of springs, average rainfall, temperature, average elevation, and slope for each province.

The total number of springs per province and the number of persons per spring based on the cumulative population of all spring's districts in each province are summarized in Figure 2. The number of springs in the HKH region that fall in Pakistan is 5051 (28%) of the total springs (18114) in the country. Generally, dependence on springs is larger in the northern part of the country.

Table 1: Spring Distribution and Annual Climatic Variables and Topographic Parameters for the Different Districts in different Provinces and Regions Across Pakistan

Province	Total Districts	Total Springs	Avg. Rainfall (mm)	Avg. Temp. (°C)	Avg. Elev. (m)	Avg. Slope
Khyber Pakhtunkhwa	37	4501	789	12-22	851	Steep
Punjab	14	1285	507	20-30	250	Flat
Sindh	8	215	294	30-40	103	Flat
Balouchistan	29	10047	310	20-30	1036	Moderate
Azad Jammu & Kashmir	10	943	1088	10-20	1350	Steep
Gilgit-Baltistan	8	1095	600	5-15	2155	Steep
Islamabad	1	28	800	15-25	500	Flat
Hindukush Himalaya	37	5051	892	10-22	1590	Steept
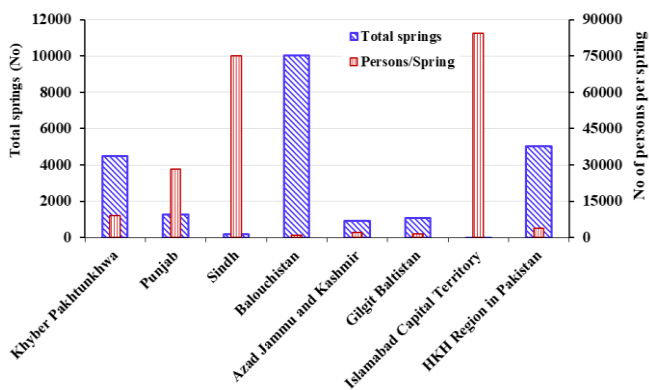
Fig. 2: Comparative analysis of the number of springs and number of persons per spring

The number of springs per unit area of respective districts in each province and the cumulative population of respective spring districts in each province is summarized in Figure 3. The average number of springs per hectare is around 3 in the spring districts of the country. However, the spring densities are 39%, 170% and 24% higher in KP, AJ&K and HKH region of Pakistan respectively than the country's average value.
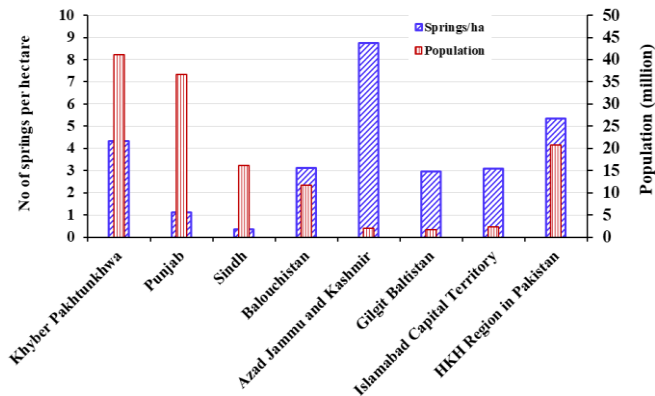
Fig. 3: Spring density and population of respective districts of provinces of Pakistan

3.2 Detailed Analysis of Key Regions

3.2.1 Khyber Pakhtunkhwa

Khyber Pakhtunkhwa (KP) has the highest density of springs showing presence in 37 districts, particularly in Malakand and Hazara divisions, as indicated in Figure 4, where factors such as higher rainfall, moderate elevation, and clay-rich soils support spring formation. Districts such as Abbottabad, Swat, and Lower Dir have a high spring density, where rainfall is high and elevation is moderate.
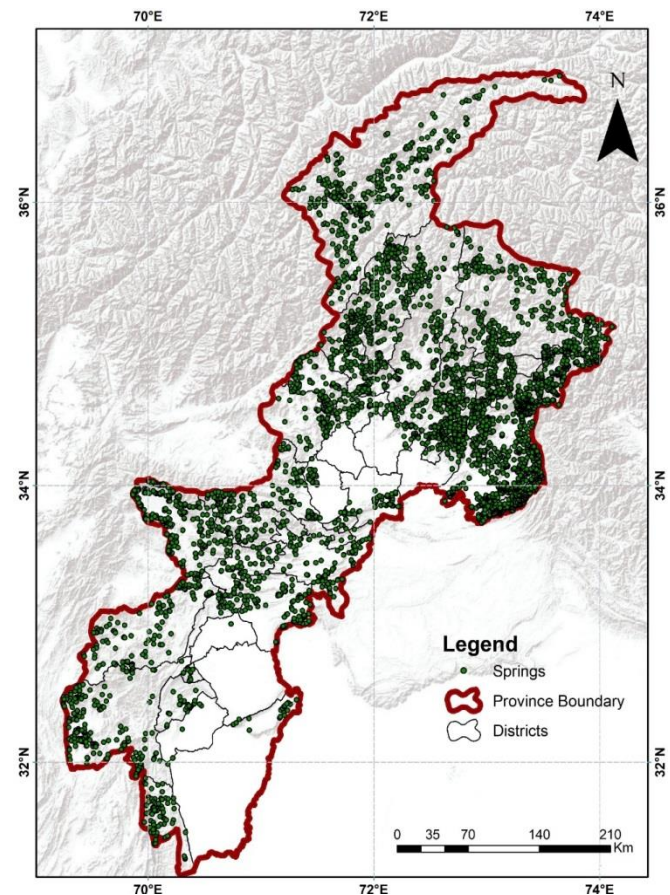
Fig. 4: Spatial distribution of springs in Khyber Pakhtunkhwa province

3.2.2 *Punjab*

Northern Punjab has larger spring presence (Figure 5), while the arid southern districts show sparse distribution. Springs in Rawalpindi and Chakwal are denser where seasonal monsoons rains are more and altitudes are moderate.

3.2.3 *Sindh*

The Sindh province show limited spring presence. The few springs found in Sindh are mostly seasonal, occurring in districts like Jamshoro, where occasional monsoon rains temporarily recharge local aquifers, as illustrated in Figure 6.

3.2.4 *Baluchistan*

The highest number of springs is found in Baluchistan, particularly in districts like Khuzdar and Kalat. Despite the province's arid climate, the geology favors the presence of springs, which are vital for local communities. The spatial distribution of springs in Baluchistan is presented in Figure 7.

3.2.5 *Azad Jammu and Kashmir*

The distribution of springs in AJ&K is vital for sustaining local communities and ecosystems. Continued research and effective management strategies are essential to ensure their availability and quality for future generations. The distribution of springs in AJ&K is presented in Figure 8.

3.2.6 *Gilgit Baltistan*

The mountainous terrain and higher elevations of GB hosts numerous springs. These springs are critical for agriculture and domestic use, with Skardu and Astore being key districts with a high density of springs. The spatial distribution of springs in GB is given in Figure 9.
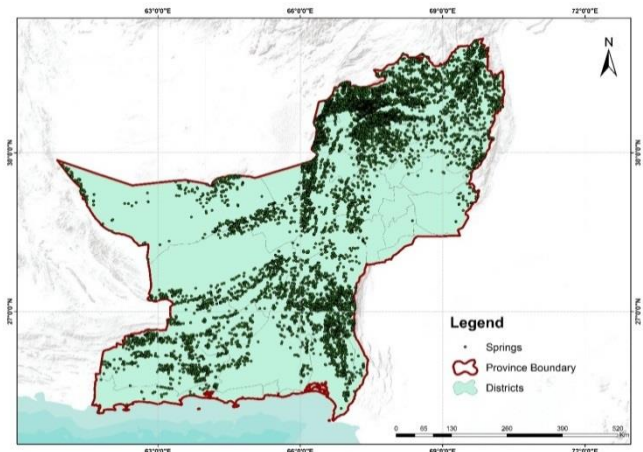
Fig. 7: Spatial distribution of springs in Baluchistan province
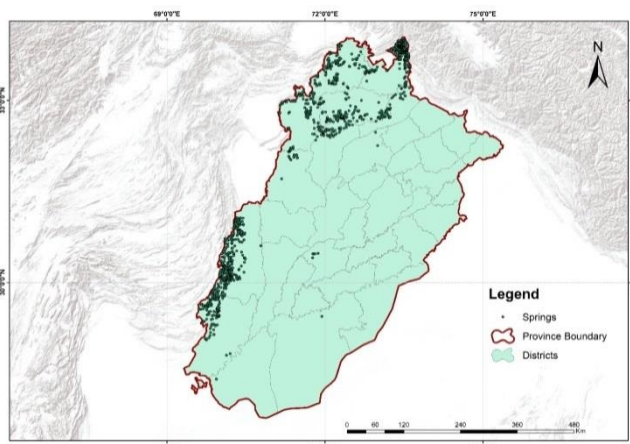
Fig. 5: Spatial distribution of springs across Punjab province
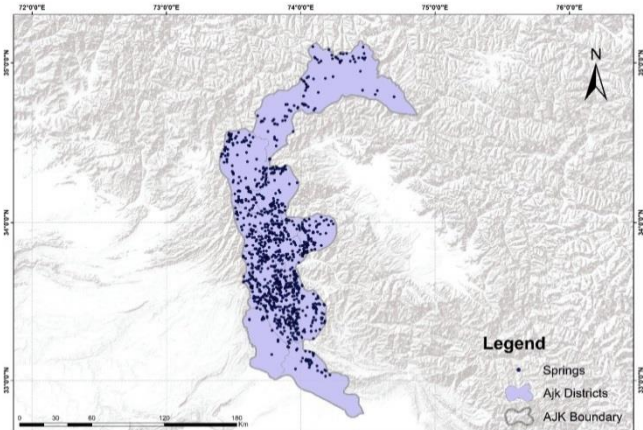
Fig. 8: Distribution of springs in Azad Jammu and Kashmir in Pakistan
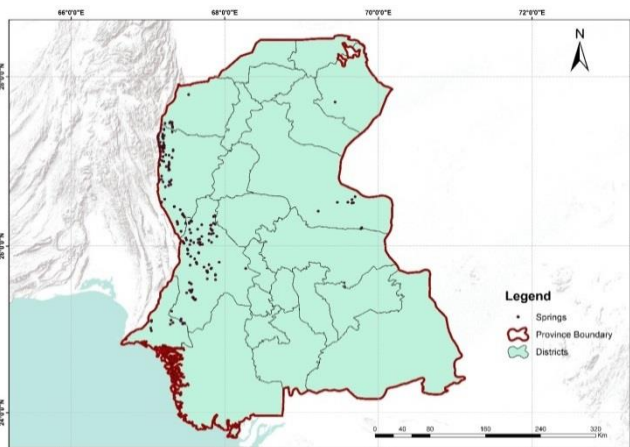
Fig. 6: Spatial distribution of springs across Sindh province
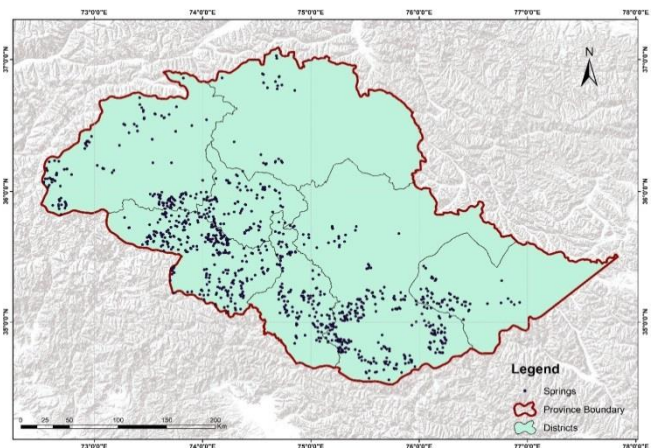
Fig. 9: Spatial distribution of springs in Gilgit Baltistan province

3.2.7 Hindu-Kush Himalaya

The spatial distribution of springs in the HKH region is presented in Figure 10. The north western part of HKH is home to majority of the springs. The HKH region host 5051 springs with majority of springs concentrated in the Himalaya and Hindukush regions while the Karakoram region host a smaller number of springs. The total population of HKH region that falls in Pakistan are around 24 million, while persons per spring are around 4739 and spring density is around 4 springs/ha.
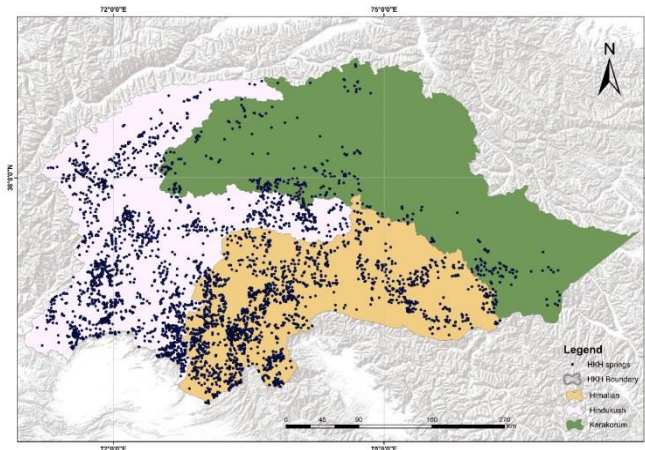
Fig. 10: Spatial distribution of springs in the Hindukush Himalaya region of Pakistan

3.3 Correlation and Regression Analysis

The correlation and regression analysis indicated a generally weak relationship between the number of springs and the climatic or topographical parameters across districts in each province, as summarized in Table 2. However, a more distinct pattern emerged in KP, Punjab, AJ&K, and the HKH region, where the number of springs exhibited a positive correlation with rainfall and elevation and a negative correlation with temperature.

These findings suggest that higher altitudes and increased precipitation Favor Spring formation, likely due to enhanced groundwater recharge and lower evaporation rates. Conversely, warmer temperatures appear to reduce spring viability, potentially due to increased evapotranspiration and reduced groundwater retention. The observed trends underscore the critical role of climatic and topographic factors in governing spring distribution, with implications for regional water management and climate resilience strategies.

In summary, the rainfall is the most significant factor influencing spring distribution, particularly in Punjab, KP, and AJ&K. Higher temperatures negatively impact spring occurrence, but the effect varies by region. Elevation moderately influences spring distribution, particularly in mountainous regions, but is less significant in arid zones such as Sindh and Baluchistan. The HKH region demonstrates a moderate dependence on rainfall, with weaker relationships to temperature and elevation.

4. Discussion

The findings indicate that the existence of springs is likely influenced by the hydro-geological characteristics of the host region, although the study presents only weak evidence regarding the contribution of environmental and topographical factors to the distribution of springs. The results suggest that regions with higher elevations and substantial rainfall, such as KP, AJ&K, and GB, tend to exhibit a higher density of springs, compared to the more arid regions of Sindh and southern Punjab. The negative correlation with temperature aligns with global findings indicating similar impacts of weather and climate change on spring systems in other parts of the HKH region [17-19].

Glacier retreat, unpredictable and extreme rainfall events in northern Pakistan have shortened the spring recharge period, resulting in reduced spring flows, particularly in regions highly dependent on springs, such as Malakand, Hazara, GB, and AJ&K. These findings are consistent with those of other studies [20, 21], which attribute reduced groundwater recharge to rising temperatures and altered rainfall patterns, further diminishing spring flows [22-24]. Land degradation due to deforestation in KP and AJ&K, coupled with the over-extraction of groundwater through deep tubewells, especially in Punjab, are key drivers of spring depletion. Similar patterns of spring depletion have been reported in other countries as well [25-29]. Based on these findings, there is a clear need to develop and implement integrated land use, land cover, forest, rainwater harvesting, artificial recharge systems and groundwater conservation policies, particularly in regions with high spring dependency

Table 2: Relationship Between Spring Distribution and Environmental Variables

Region/Province	Rainfall (r, R², p)*	Temperature (r, R², p)	Elevation (r, R², p)
Khyber Pakhtunkhwa	0.52, 0.27, p<0.05	-0.37, 0.13, p<0.05	0.36, 0.13, p<0.05
Punjab	0.61, 0.37, p<0.05	-0.22, 0.05, p>0.05	0.39, 0.15, p>0.05
Sindh	0.05, 0.002, p>0.05	0.32, 0.12, p>0.05	0.04, 0.001, p>0.05
Balouchistan	0.13, 0.02, p>0.05	-0.04, 0.001, p>0.05	0.02, 0.0002, p>0.05
Azad Jammu & Kashmir	0.58, 0.33, p>0.05	0.21, 0.04, p>0.05	0.39, 0.15, p>0.05
Gilgit-Baltistan	0.03, 0.001, p>0.05	-0.18, 0.03, p>0.05	0.37, 0.14, p>0.05
Hindu Kush-Himalaya	0.43, 0.18, p<0.05	-0.15, 0.02, p>0.05	0.15, 0.02, p>0.05

*(Correlation Coefficient (r), Coefficient of Determination (R²), and Statistical Significance (p-value))

such as KP and Baluchistan. Reforestation, sustainable land-use practices, and artificial recharge systems of groundwater with rainwater may serve as effective strategies to mitigate spring depletion.

This study reinforces the significance of topographic and climatic factors in determining spring distribution across Pakistan, a pattern observed globally [30-33]. Specifically, regions with higher elevations and greater rainfall, notably KP, AJ&K, and GB, are correlated with a higher number of springs. Conversely, temperature negatively correlates with spring occurrence in arid regions such as Sindh and Baluchistan. Springs in these arid zones are often seasonal and do not provide perennial water flow. Consequently, spring conservation in regions like KP, GB, and AJ&K requires more attention and government investment to ensure sustainable water availability and water security [10]. Comprehensive awareness, policy frameworks, and effective monitoring systems for springs are urgently needed to secure sustainable spring management in Pakistan.

The strong correlation between elevation and spring distribution suggests that mountainous regions have a greater potential for spring formation due to higher rainfall and cooler temperatures, both of which are conducive to spring recharge, as noted by [32]. Furthermore, the moderate to steep slopes, along with relatively more ground cover and forest in these areas, facilitate water percolation into underground aquifers, which is crucial for sustaining spring flows. The negative correlation between temperature and spring distribution, particularly in Sindh and Baluchistan, highlights the vulnerability of springs to rising temperatures. As climate change exacerbates temperature extremes and alters precipitation patterns, the recharge of springs in arid and semi-arid regions is expected to decline further. These findings are consistent with global studies documenting similar climate change impacts on water resources, particularly in the HKH region [32, 34, 35].

In northern Pakistan, particularly in KP, GB, and AJ&K, the increasing frequency of extreme climate events [36] and the shortening of the snowmelt season have reduced the water available for spring recharge, contributing to declining spring flows. This reduction in water availability for domestic and agricultural use has adversely affected the livelihoods of communities that rely on springs [37]. Anthropogenic activities, such as deforestation, land-use changes, direct disposal of sewage water and the over-extraction of groundwater through deep pumping to meet the demands of a growing population are significant contributors to spring depletion and the deterioration of water quality [21]. The accelerating deforestation in KP and AJ&K has diminished the land's capacity to absorb and retain water, further hindering spring recharge.

The results of this study emphasize the importance of promoting site-specific interventions and an integrated approach to resource management, as advocated by [38], which could be vital for the conservation and sustainable management of springs across Pakistan. Focusing on isolated resource management solutions may not be effective. Instead, a holistic, multidisciplinary approach involving various departments working collaboratively is essential. Managing water resources from the point of rainfall to river basins in an integrated manner is critical. Projects should prioritize interventions based on scientific evidence and in-depth knowledge of local vulnerabilities, taking into account the characteristics of catchments, sub-watersheds, and watersheds to ensure sustainable development and targeted actions for each locality.

5. Conclusion

This study represents a pioneering effort in mapping and analyzing the distribution of springs across Pakistan. Springs are vital water sources for rural and mountainous regions of Pakistan, particularly in areas with limited access to alternative water resources. However, their sustainability is increasingly threatened by climate change, including rising temperatures, altered rainfall patterns, glacier retreat, deep boring and land degradation. These challenges have been particularly pronounced in northern Pakistan, where the dependence on springs for agriculture, domestic use, and ecosystem support is high. The degradation of spring water quality, compounded by deforestation, land-use changes, and over-extraction, further exacerbates the vulnerability of these vital resources.

To safeguard springs and ensure sustainable water availability, it is essential to implement targeted conservation strategies, including rainwater harvesting, artificial recharge of groundwater, reforestation, land-use management, and sustainable groundwater practices. Furthermore, addressing the gaps in updated springs data, spring management, governance, policies and integrating climate change adaptation measures will be crucial to preserving these resources for future generations. This study highlights the urgent need for comprehensive research and policy frameworks that consider the unique environmental and socio-economic dynamics of spring-dependent regions in Pakistan.

References

[1] G. Van der Kamp, "The hydrogeology of springs in relation to the biodiversity of spring fauna: a review," Journal of the Kansas Entomological Society, pp. 4-17, 1995.

[2] Z. T. Virk, B. Khalid, A. Hussain, B. Ahmad, S. S. Dogar, N. Raza, N. Raza, B. Iqbal., "Water availability, consumption and sufficiency in Himalayan towns: a case of Murree and Havellian towns from Indus River Basin, Pakistan," Water Policy, vol. 22, no. S1, pp. 46-64, 2020.

[3] S. Panwar, "Vulnerability of Himalayan springs to climate change and anthropogenic impact: a review," Journal of Mountain Science, vol. 17, no. 1, pp. 117-132, 2020.

[4] D.D. Poudel and T.W. Duex, "Vanishing springs in Nepalese mountains: Assessment of water sources, farmers' perceptions, and climate change adaptation," Mountain Research and Development, vol. 37, no. 1, pp. 35-46, 2017.

[5] H. A. Sheikh, M. S. Bhat, A. Alam, S. Ahsan, and B. Shah, "Evaluating the drivers of groundwater spring discharge in Sindh basin of Kashmir Himalaya," Environment, Development and Sustainability, pp. 1-23, 2023.

[6] I. K. Murthy, R. Tiwari, G. Hegde, M. Beerappa, K. Rao, and N. Ravindranath, "Comparison of mitigation potential estimates of three models using the IPCC 3-tier approach," International Journal of

Climate Change Strategies and Management, vol. 6, no. 3, pp. 236-249, 2014.

[7] P. Wester, A. Mishra, A. Mukherji, and A. B. Shrestha, "The Hindu Kush Himalaya assessment: mountains, climate change, sustainability and people." Springer Nature, 2019.

[8] P. C. Tiwari, A. Tiwari, and B. Joshi, "Urban growth in Himalaya: understanding the process and options for sustainable development," Journal of Urban and Regional Studies on Contemporary India, vol. 4, no. 2, pp. 15-27, 2018.

[9] A. Hussain, G. Rasul, B. Mahapatra, S. Wahid, and S. Tuladhar, "Climate change-induced hazards and local adaptations in agriculture: A study from Koshi River Basin, Nepal," Natural Hazards, vol. 91, no. 3, pp. 1365-1383, 2018.

[10] S. W. Hussain, K. Hussain, Q. Zehra, S. Liaqat, A. Ali, Y. Abbas, and B. Hussain., "Assessment of drinking water quality, Natural springs and surface water and associated health risks in Gilgit-Baltistan Pakistan," Pure and Applied Biology, vol. 11, no. 4, pp. 919-931, 2022.

[11] M. A. Mirza, M. Khuhawar, and R. Arain, "Quality of spring water in the catchment areas of the Indus River," Asian Journal of Chemistry, vol. 19, no. 7, pp. 5279-5304, 2007.

[12] T. M. Jahangir, M. Y. Khuhawar, S. M. Leghari, M. T. Mahar, and A. A. Khaskheli, "Chemical assessment of natural springs of Sindh Pakistan," Canadian Journal of Pure and Applied Sciences Senra Academic Publishers, British Columbia, vol. 7, no. 2, pp. 2431-2449, 2013.

[13] A. Butt, R. Shabbir, S. S. Ahmad, and N. Aziz, "Land use change mapping and analysis using Remote Sensing and GIS: A case study of Simly watershed, Islamabad, Pakistan," The Egyptian journal of remote sensing and space science, vol. 18, no. 2, pp. 251-259, 2015.

[14] V. Simeonov, J. Stratis, C. Samara, G. Zachariadis, D. Voutsa, A. Anthemidis, M. Sofonio, and T. Kouimtzis, "Assessment of the surface water quality in Northern Greece," Water research, vol. 37, no. 17, pp. 4119-4124, 2003.

[15] M. Afşin, İ. Kuşcu, H. Elhatip, and K. Dirik, "Hydrogeochemical properties of CO_2-rich thermal–mineral waters in Kayseri (Central Anatolia), Turkey," Environmental Geology, vol. 50, pp. 24-36, 2006.

[16] S. Zokaib and G. Naser, "Impacts of land uses on runoff and soil erosion A case study in Hilkot watershed Pakistan," International Journal of Sediment Research, vol. 26, no. 3, pp. 343-352, 2011.

[17] S. Tambe, G. Kharel, M. Arrawatia, H. Kulkarni, K. Mahamuni, and A. K. Ganeriwala, "Reviving dying springs: climate change adaptation experiments from the Sikkim Himalaya," Mountain Research and Development, vol. 32, no. 1, pp. 62-72, 2012.

[18] S. P. Singh, R. Thadani, G. Negi, R. D. Singh, and S. Gumber, "The impact of climate change in Hindu Kush Himalayas: key sustainability issues," Himalayan Weather and Climate and their Impact on the Environment, pp. 453-472, 2020.

[19] N. Chettri, A. B. Shrestha, and E. Sharma, "Climate change trends and ecosystem resilience in the Hindu Kush Himalayas," Himalayan Weather and Climate and their Impact on the Environment, pp. 525-552, 2020.

[20] K. Khadka, G. Pokhrel, M. Dhakal, J. Desai, and R. B. Shrestha, "Spring-shed management: an approach to revive drying Springs in the Himalayas," LEAV, 2019.

[21] S. T. Rahman Ullah, Z. Malik, W. M. Achakzai, S. Saddozai, A. Raza, A. Rahat, T. Aziz, T. Azeem, H.U. Rehman, and F. Amin., "Drinking Water Quality Assessment of Springs in Gokand Valley District Buner Khyber Pakhtunkhwa Pakistan," Journal of Health and Rehabilitation Research, vol. 3, no. 2, pp. 988-995, 2023.

[22] G. Cinkus, V. Sivelle, H. Jourde, N. Mazzilli, Y. Tramblay, B. Andreo, J.A. Barbera, R. Bouhlila, J. Doumar and J. Fernandez-Ortega, "Impact of climate change on groundwater level dynamics and karst spring discharge of several karst systems in the Mediterranean

area," in EGU General Assembly Conference Abstracts, 2023, pp. EGU-12285.

[23] A. Lamacova, O. Ledvinka, L. Bohdalkova, F. Oulehle, J. Kreisinger, and R. Vlnas, "Response of spring yield dynamics to climate change across altitude gradient and varied hydrogeological conditions," Science of The Total Environment, vol. 921, p. 171082, 2024.

[24] P. Ranjan, P. K. Pandey, V. Pandey, and P. T. Lepcha, "Spring Water Management to Ensure Long Term Sustainability in North-Eastern Regions of India," in IOP Conference Series: Earth and Environmental Science, 2022, vol. 1084, no. 1: IOP Publishing, p. 012062.

[25] G. Cardenas Castillero, M. Kuráž, and A. Rahim, "Review of Global Interest and Developments in the Research on Aquifer Recharge and Climate Change: A Bibliometric Approach," Water, vol. 13, no. 21, p. 3001, 2021.

[26] W. Cheng, Q. Feng, H. Xi, X. Yin, L. Cheng, and C. Sindikubwabo, "Modeling and assessing the impacts of climate change on groundwater recharge in endorheic basins of Northwest China," Science of The Total Environment, vol. 918, p. 170829, 2024.

[27] N. Mizyed, "Climate change challenges to groundwater resources: Palestine as a case study," Journal of water resource and protection, vol. 10, no. 2, pp. 215-229, 2018.

[28] E. Dubois, M. Larocque, S. Gagné, and M. Braun, "Climate Change Impacts on Groundwater Recharge in Cold and Humid Climates: Controlling Processes and Thresholds. Climate 2022, 10, 6," Application of Climatic Data in Hydrologic Models, pp. 1-115, 2022.

[29] S. Gelsinari, S. Bourke, J. McCallum, D. McFarlane, J. Hall, and R. Silberstein, "Nonstationary recharge responses to a drying climate in the Gnangara Groundwater System, Western Australia," Journal of Hydrology, vol. 633, p. 131007, 2024.

[30] G. Tamburello, G. Chiodini, and G. Ciotoli, "Global thermal spring distribution and relationship to endogenous and exogenous factors. Nat Commun 13: 6378," Nature Communications, vol. 13, no. 6378, pp. 1-9, 2022.

[31] I. Martinić and I. Čanjevac, "Distribution and Characteristics of Springs in Two Neighboring Areas of Different Morphogenic Relief Type—Example of SW Medvednica Mountain (Central Croatia)," Water, vol. 16, no. 7, p. 994, 2024.

[32] V. Audorff, J. Kapfer, C. Beierkuhnlein, M. Strohbach, V. Audorff, and C. Beierkuhnlein, "The role of hydrological and spatial factors for the vegetation of BayCEER-online," vol. 5, pp. 24-46, 2009.

[33] E. V. Gaidukova and V. V. Kovalenko, "Geographic pattern as a determinant factor of interlinking climatic and hydrological components of the natural resources," International Letters of Natural Sciences, vol. 74, pp. 49-55, 2019.

[34] P. Gairola, A. Maiti, S. Sannigrahi, A. Bhatt, S. Singh Rawat, and S. Kumar, "A novel approach for predicting spring locations using machine learning algorithms in Indian Himalayan Region," in EGU General Assembly Conference 2023, pp. EGU-13411, 2023.

[35] E. S. Pérez, "Distribution functions of spring discharges according to their lithologies and the influence of lower limit to flow: an example from Spain," Groundwater, vol. 39, no. 2, pp. 203-209, 2001.

[36] N. Khan, N. P. Gaire, O. Rahmonov, and R. Ullah, "Multi-century (635-year) spring season precipitation reconstruction from northern Pakistan revealed increasing extremes," Scientific Reports, vol. 14, no. 1, pp. 92, 2024.

[37] W. Ishaque, R. Tanvir, and M. Mukhtar, "Climate change and water crises in Pakistan: implications on water quality and health risks," Journal of Environmental and Public Health, vol. 2022, no. 1, pp. 1-12, 2022.

[38] G. Akbar, A. A. Khan, M. M. Ahmad, M. L. Shrestha, A. De Silva, B. V. R. Punyawardena, S. Thakuri, and D.R. Bhattarai, "Improving decision support system in identifying vulnerability rating and prioritizing the best interventions for sustainable watersheds in Pakistan, Nepal, and Sri Lanka," Water Resources and Irrigation Management-WRIM, vol. 12, no. 1-3, pp. 101-114, 2023.

Statistical Analysis of Yttrium-Doped ZnO Nanoparticles for Gas Sensing Applications

Satender Kumar[1], Ankur Nehra[2*]

[1]*Department of Physics (School of Science) Sunrise University, Alawar, Rajasthan, India*

[2]*Department of Mathematics, Dhanauri P.G. College, Dhanauri, Haridwar, Uttarakhand, India*

A B S T R A C T

Yttrium-doped ZnO (YZ) thin films were synthesized using sol-gel spin coating technique on planar glass substrates. Their optical and electrical properties were analyzed to assess their potential for O_2 gas detection. XRD analysis confirmed a hexagonal wurtzite crystal structure, while FE-SEM images revealed a network of spherical nanoparticles. Optical transmission spectra showed that increasing Y-dopant concentration widened the bandgap from 3.27 eV to 3.30 eV. Electrical measurements indicated that YZ3 exhibited highest conductivity. Gas sensing performance was evaluated for YZ2 and YZ4 at an O_2 flow rate of 450 sccm and an operating temperature of 70°C. Among them, YZ4 demonstrated the highest response, reaching a value of 1, with a fast response time of 2 seconds and a recovery time of 4 seconds. Statistical analysis suggests that YZ thin films hold promise for efficient gas sensing at lower operating temperatures.

Keywords: YZ thin films, Electrical properties, Gas sensing, Sol-gel, Synthetic material

1. Introduction

The capability of non-toxic gases like O_2, H_2, and Ar to detect gases, generate chemicals, monitor air quality, and fuel gas-powered engines has garnered scientific interest for its applications in clinical diagnostics [1, 2]. Oxygen gas is an odorless, combustible gas that is essential to many organisms' ability to survive. Examples of semiconductor metal oxides that are necessary for gas distinction are ZnO, TiO_2, and CdO. ZnO has been considered the ideal material for gas detection applications because of its superior substance dependability, warmth under operating settings, and remarkable adaptability to lead electrons [3-8]. Due to its large band hole (3.37 eV) and high excitation energy (60 meV), ZnO is a very promising material for a variety of uses, including gas sensors, photodetectors, Schottky diodes, and photocatalysis [9]. Modern warming heaters and underground mine O_2 gas screening use ZnO-based oxygen sensors. Numerous factors, including deformities, particle size, surface characteristics, blockage level and width, and stoichiometry, influence the properties of sensors [10-11]. Doping ZnO with metals, non-metals, and interesting earth metals can reduce its resistivity [12]. These rare earth metals stand out from one another because they are predecessors of ZnO dopants, which suppress the local point defect concentrations of ZnO. La, Sc, and Y are examples of uncommon earth minerals that are widely used in a variety of applications due to their strong conductivity, consistent electrochemical responses, and iridescent qualities [13-19]. Yttrium (Y) doping in ZnO has a significant effect on the identification of O2 gas, as demonstrated by the changed optical and electrical characteristics of ZnO and the more noticeable ionic radii of Y3+ (1.01 Å) compared to Zn2+ (0.66 Å) [20-23]. Meanwhile, ZnO has been doped with Y to improve its optical band hole and conductivity, making it more appropriate for gas detection applications [24-25]. The size and surface form of ZnO was entirely altered by the proper concentration of Y doping. Additionally, doping ZnO has been demonstrated by Guo et al. [26] to alter its surface charge regions, which impacts the material's use, particularly

for gas detection applications. Despite the data, ZnO tiny videos' union of kink-type morphology is excellent and more accurate for detecting O_2 gas. The dynamic surface region that the sensor uses to perform responses at the sensor surface represents the sensor reaction. A suitable dynamic surface region will therefore most likely successfully ascend the sensor reaction for the gas finding [27]. For slim film preparedness, a variety of witness tactics have been put forth, including the sol-gel approach [29-30], beat laser, splash pyrolysis [28], and synthetic fume statement. The sol-gel process is the most advantageous of them all since it is low cost, offers large region coatings, has an excellent material structure, and provides basic creation [31]. In this work, pure and Y-doped ZnO thin films were produced on a glass substrate via the sol-gel procedure. The main optical and morphological features of the thin films were described. Furthermore, oxygen gas's gas-detecting properties have also been taken into consideration.

2. Experimental Details

Yttrium acetic acid derivation di-hydrate ($C_6H_{14}O_7Y$; immaculateness 099.9%), 2-methoxy ethanol ($C_3H_8O_2$; immaculateness 099.0%), monoethanolamine (C_2H_7NO; virtue 099.9%), and zinc acetic acid derivation di-hydrate ($C_4H_{10}O_6Zn$; virtue 098.0%) were the materials and synthetic compounds used in the trial. Alfa Aesar supplied all the materials and synthetics used in the analysis, requiring no further sanitization. Prior to the claim, the substrates had been properly treated with $(CH_3)_2CO$, ultrasonically sonicated at a steady voltage, and cleaned by the cleaner. Every synthetic material and reagent was utilized exactly as it was obtained. After mixing ZnO with Y (Y=0, 0.50, 01.0, and 1.5 at. %) in 2-methoxy ethanol for 20 minutes, the material was ready. Subsequently, one drop at a time, stabilizer specialist mono ethanolamine was applied to each arrangement, and the mixture was stirred for a further two hours at room temperature. Thus, uniform simple configurations were obtained, and as a result, all replies for maturing 24 hours were obtained to outline all substantive

*Corresponding author: nehradpgc123@gmail.com

responses among them. Furthermore, turn-covering units employed the obtained arrangements for the statement of small-scale films. Throughout the affidavit of every example, the testimony rate was maintained at 2500.00 rpm/30 s, and the samples were then dried at 200º C. To achieve the perfect thickness of the slight films, the cycles were repeated several times. Finally, the thin films were heated to 450º C for one hour in a silent heater to promote genuine crystallinity and remove impurities. Codes YZ1, YZ2, YZ3, and YZ4 were given to ZnO doped with Y that included 0.0, 0.50, 01.0, and 1.50 at. % of Y Slim films, which were mixed at the same time. X-ray diffraction (XRD) (Philips X'pert Favorable to diffractometer) was used to analyze the primary features of small films from YZ1 to YZ4. YZ meager videos were transported using a UV-Vis spectrophotometer (Shimadzu 3600.00), and their surface morphology was examined using an electron microscope (SEM) (Zeiss Super 60.00). Two test electrometers (Keithly-4200.00 SCS) were used to assess the I-V characteristics, and a gas detection system was used to look at the gas reaction of films that were comparable to our past research [32].
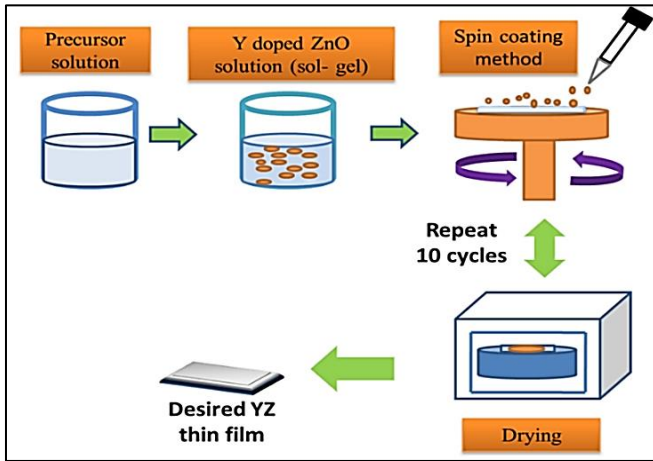

Fig. 1: Schematic Diagram for the Production of YZO Thin Film

3. Main Results with Discussion

The XRD analysis of the YZO thin film test results is shown in Figure 2. In the diffraction example of YZO tests, many tops were found at planes (001), (002), (101), (102), and (110). Based on XRD analysis, all of the YZO thin films are polycrystalline and match the wurtzite hexagonal structure of JCPDS card number 36-1451 (ZnO). It was shown that when the doping degree of Y grows, the ZnO tops become more distributed and varied in power compared to undoped ZnO (YZ1). By widening the yttrium focus, the diversity in force is linked to the enhancement of gem formation. Furthermore, the XRD design did not include any pollutants or extra pinnacles, indicating that Y particles replace ZnO locations or interstitial destinations [33, 34]. Moreover, there was neither left nor right shifting, which produced excellent agreement with the typical ZnO results. Using Eq. 1, the grid limits 'a' and 'c' were evaluated at (100) and (002) tops, respectively, and discussed in Table 1.

$$\frac{1}{d^2} = \frac{4}{3a^2}(h^2 + hk + k^2) + \frac{l^2}{c^2} \qquad (1)$$

Furthermore, no contaminants or extra pinnacles were added to the XRD design, indicating that Y particles replace ZnO locations or interstitial destinations [33, 34]. Moreover, neither left nor right moving was present, which greatly agreed with the typical ZnO results. Table 1 presents the results of the evaluation of the grid boundaries 'a' and 'c' at (100) and (002) tops, respectively, using Eq. 1.

$$D = 0.94\lambda/\beta \cos\theta \qquad (2)$$

Where the usual bounds are denoted by θ, β, and λ [35]. As shown in Table 1, it was discovered that increasing the doping of Y in ZnO changed the value of crystallite size.

Table 1: Y-Doped ZnO meagre films: optical limit and underlaying layers

Sample Code	Peak position (2θ)	Lattice parameter a (Å)	Lattice parameter c (Å)	Crystalline size nm	Optical band gap (Eg)(eV)
YZ1	036.121	03.241	05.23	18.00	03.27
YZ2	036.220	03.249	05.23	17.00	03.128
YZ3	036.520	03.247	05.23	10.00	03.129
YZ4	036.319	03.252	05.23	12.00	03.130
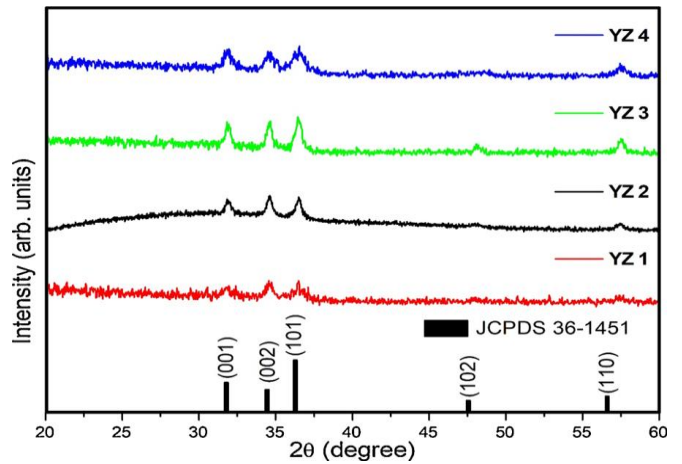
Fig. 2: XRD pattern of Y doped ZnO (Y=0.0. 0.5. 1. 1.5at%) thin film samples coded as YZ1, YZ2, YZ3 and YZ4

3.1. Surface Structure

The FESEM was used to examine the surface morphology of YZ thin films, as Figure 3 illustrates. SEM scans showed that, at low magnification, all thin films had wrinkle-type morphology, as shown in Figures 3(a), (c), (e), and (d). These fault networks were made up of tiny, spherical nanoparticles. This kind of crumpled morphology may have been molded by compressive film forces because a YZ-put-together configuration was maintained with respect to a glass substrate during the combination cycle [36–37]. The difference in warm development coefficients then surfaced in the fragile film drying system, which motivated the gelated-based slight film twisting technique. As can be shown in Figure 3 (b, d, f, and h), higher amplification usually reveals that thin films have oval and round-type morphology. In this way, the grains were arranged in a more granular form and suitably interconnected.
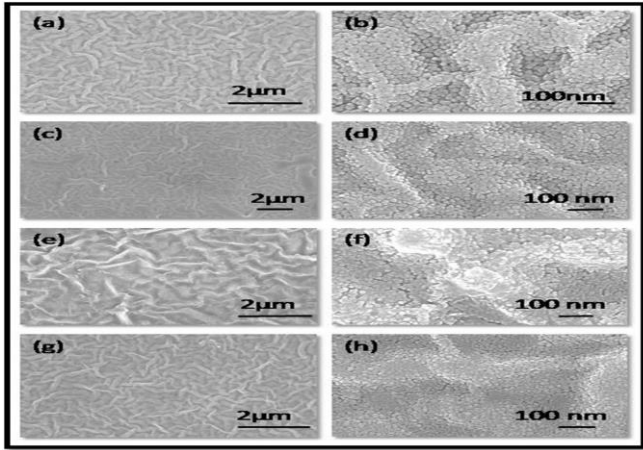
Fig. 3: FESEM pictures show ZnO doped with Y.

3.2. Optical Study

The transmission spectra of the slight films of YZ1, YZ2, YZ3, and YZ4 were kept within the 300–800 nm frequency range, as Fig. 4(a) illustrates. As Yttrium doping in ZnO increased, the typical conveyance increased in the notable region for testing from YZ1 to YZ4, as shown in Fig. 4(a). In the meantime, there was no discernible difference between the contaminated and pure samples' retention margins. The reduction of the spaces in the example is directly related to the improvement in apparent conveyance. In this way, it expands the distribution and enhances the homogeneous design. Furthermore, the standard conveyance was directly related to grain size. The grain size changed, but just a little. In the obvious location, typical conveyance therefore only changed from 92% to 97%. Consequently, a critical rise in straightforwardness was not achieved by raising the doping concentration of Y in ZnO. Rana et al. [33] have also explained similar results for Mg-doped ZnO setup using a sol-gel turn covering technique. In due course, Tauc's plot was employed to evaluate the optical bandgap of the samples using Eq. 3.
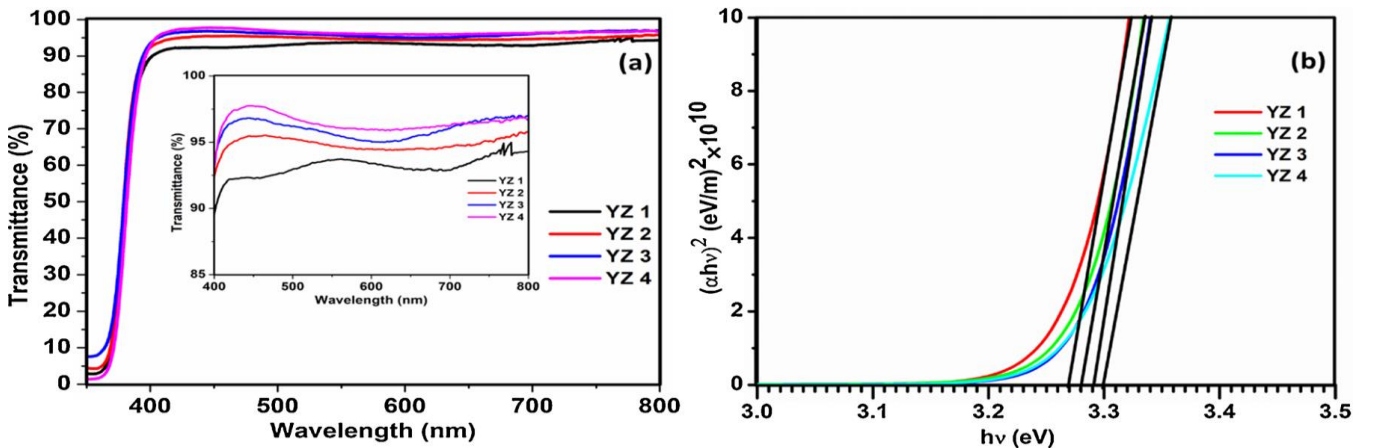
$$(\alpha h\nu)^2 = A(h\nu - E_g) \tag{3}$$

where $h\nu$ is the occurrence energy, A is the proportionality consistent, E_g addresses the example's band hole, and α addresses the retention coefficient. The band gap was calculated by extrapolating the direct parcel from the $(\alpha h\nu)^2$ vs $h\nu$ plot, as explained in Fig. 4(b) [38]. Table 1 illustrates how the estimated bandgap changed as the Y doping focus increased, going from 3.27 eV to 3.30 eV. The optical band hole saw had a small alteration due to the low yttrium doping in ZnO. This could be a result of Y's fermi level, which is associated with the Greenery Burstein influence and is located inside ZnO's conduction band. Similar outcomes were shown by Thirumoorthi et al. [34] when Y-doped ZnO thin films were made by the sol-gel turn covering technique.

3.3. Electrical Characteristics

Figure 5 shows the current-voltage (I-V) characteristics of the thin films YZ1, YZ2, YZ3, and YZ4. Research has shown that while the conductivity of the thin film was lower for test YZ4, it was higher for test YZ3 when the Y doping level in ZnO was increased [39, 40]. The whole diversity in the conductivity of YZO dainty flicks was caused by the straightforward substitution of Y^{3+} in Zn^{+2} locations with essentially no grid twisting. Expanding the electrical conductivity is caused by introducing additional free electrons into the conduction band, as demonstrated by the YZ1 to YZ3 tests. From that point on, The SEM image in Fig. 3(h) makes clear that the conductivity was decreased for the YZ4 test, and the cause was grain limit dispersion and isolation of Y at the grain limit. That being said, the YZ4 test's electrical conductivity was more notable than the pure ZnO test (YZ1 test). Ozturk and colleagues similarly reported similar outcomes. Moreover, the film's outer layer and crystallinity also affect how the conductivity varies. Similarly, the dopants and defects have a major role in regulating the conductivity of the thin layer. Furthermore, the SEM micrograph's flaw-type morphology could give electrons a clear route to travel, increasing electrical conductivity [34] and improving sensor response.

Figure 4: Optical properties of ZnO thin-film doped with Y: Transmission (a) and optical band gap (b)
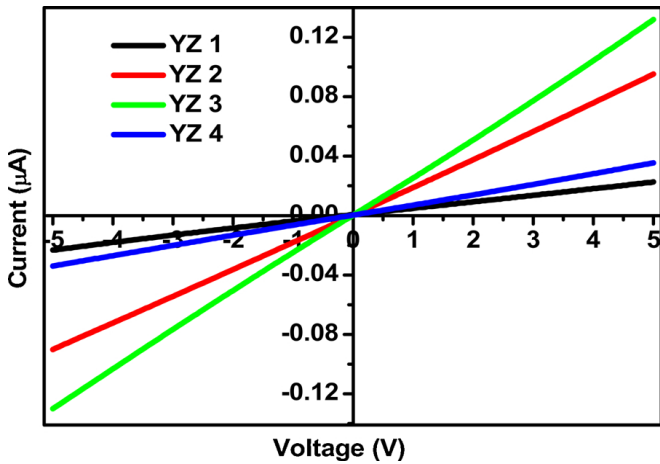
Fig. 5: I-V characteristics of thin films YZ1, YZ2, YZ3, and YZ4 are shown in this Figure

3.4   Gas Sensing

The restricted film output of YZ was optimized for gas detection. The quality of the diamonds and the electrical responsiveness of the thin sheets are two factors that affect the detecting reaction. All YZ slim films have a gem structure, which is confirmed by the XRD design. Better electrical outcomes were anticipated in every situation, as shown by the SEM pictures' kink-type surface topology. It was determined that the YZ2 test's defect type morphology was useful for identifying O2 gas, while improvements in awareness of CO_2 gas were shown by Basyooni et al. [42] using the Na-ZnO nanostructured defect type morphology. Additionally, the I-V research shows that the YZ4 thin film's conductivity is the most noteworthy. The YZ slight film tests were judged to have exhibited oxygen detection at a convergence of 450 sccm. In our environment, oxygen is a readily available gas that interacts with the surface of metal oxides to function as an electron acceptor, ionizes, and forms a superficial ionic layer that aids in the retention of vaporous particles. One important limit for gas-detecting applications is working temperature. The stability of the sensor response is displayed in Fig. 6(a). The voltage rises quickly and stabilizes when O_2 gas enters the test chamber. When the O_2 gas is taken out of the test chamber, the voltage returns to its starting point. For the YZ2 and YZ4 experiments, the sensor reaction/recuperation times were observed at around 2 s/3 s and 2 s/4 s, respectively. Furthermore, the YZ2 thin film's suitability for the gas reaction is demonstrated in Fig. 6(b), where the reaction bend is almost constant. For the YZ4 test, the highest sensor reaction was recorded at 70° C, with a reaction esteem of 1. Compared to YZ4, At all operating temperatures, YZ2's sensor response was poorer. Because the kink-type morphology facilitates easy electron movement and produces better electrical results, the morphology at the surface level was directly responsible for the detecting reaction.

$O_2(gas) + e^-(srf)$	....	$O_2^-(ads)$	(4)
$O_2(gas) + e^-(srf)$	....	$2O^-(ads)$	(5)
$1/2O_2(gas) + e^-(srf)$	....	$O^-(ads)$	(6)

4.   Conclusion

Yttrium-doped ZnO (YZ) thin films were successfully synthesized using the sol-gel spin coating technique on flat glass substrates. Their structural, optical, and electrical properties were analyzed to assess their potential for O_2 gas detection. XRD analysis confirmed a hexagonal wurtzite crystal structure, while FE-SEM images revealed spherical nanoparticles forming a network. Optical transmission spectra showed that increasing Y-dopant concentration widened the bandgap from 3.27 eV to 3.30 eV. Electrical analysis indicated that YZ3 exhibited the highest conductivity.

Gas sensing performance was evaluated for YZ2 and YZ4 at an O_2 flow rate of 450 sccm and an operating temperature of 70°C. Among them, YZ4 demonstrated the highest gas response, reaching a value of 1, with a fast response time of 2 seconds and a recovery time of 4 seconds. These findings suggest that YZ thin films are promising candidates for gas detection applications at lower operating temperatures, as supported by statistical analysis.
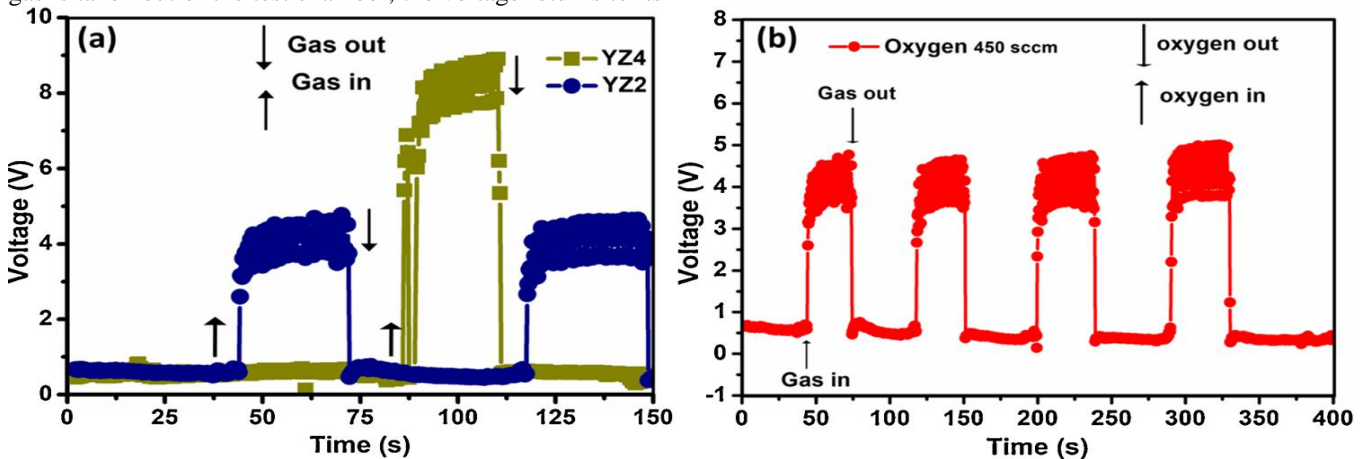

Fig. 6: Curve of Sensor Response

References

[1] R. T. R. Kumar, J. Grabowska, J. P. Mosnier, M. O. Henry, and E. McGlynn, "Morphological control of ZnO nanostructures grown on silicon in integrated optoelectronic devices," *Proc. SPIE*, vol. 6474, pp. 64741, 2007.

[2] C. Y. Lu, S. P. Chang, S. J. Chang, T. J. Hsueh, C. L. Hsu, Y. Z. Chiou, and I. C. Chen, "ZnO nanowire-based oxygen gas sensor," *IEEE Sens. J.*, vol. 9, no. 4, pp. 485–489, 2009.

[3] N. Kumar, R. Kaur, and R. M. Mehra, "Characterization of sol-gel derived yttrium-doped n-ZnO/p-Si heterostructure," *Mater. Sci. Poland*, vol. 24, pp. 375–383, 2006.

[4] V. Kumar, V. Kumar, S. Soma, L. P. Purohit, O. M. Ntwaeaborwa, and H. C. Swart, "Role of swift heavy ion irradiation on the emission of boron-doped ZnO thin films for near white light application," *J. Alloys Compd.*, vol. 594, pp. 32–38, 2014.

[5] T. K. Pathak, V. Kumar, H. C. Swart, and L. P. Purohit, "P-type conductivity in doped and co-doped ZnO thin films synthesized by RF magnetron sputtering," *J. Mod. Opt.*, vol. 62, pp. 1368–1373, 2015.

[6] R. C. Singh, M. P. Singh, O. Singh, P. S. Chandi, and R. Kumar, "Effect of 100 MeV O^{7+} ions irradiation on ethanol sensing response of nanostructures of ZnO and SnO_2," *Appl. Phys.*, vol. 98, pp. 161–166, 2010.

[7] V. Galstyan, E. Comini, C. Baratto, G. Faglia, and G. Sberveglierim, "Nanostructured Zn chemical gas sensor," *Ceram. Int.*, vol. 41, pp. 14239–14244, 2015.

[8] G. K. Upadhyay, J. K. Rajput, T. K. Pathak, and P. K. Pal, "Tailoring and optimization of hybrid ZnO: TiO_2: CdO nanomaterials for advanced oxidation process under visible light," *Appl. Surf. Sci.*, vol. 509, pp. 145326, 2020.

[9] G. K. Upadhyay, J. K. Rajput, T. K. Pathak, and V. Kumar, "Synthesis of ZnO: TiO_2 nanocomposites for photocatalyst application in visible light," *Vacuum*, vol. 160, pp. 154–163, 2019.

[10] G. Korotcenkov, "Handbook of Gas Sensor Materials: Properties, Advantages and Shortcomings for Applications," Volume 1: Conventional Approaches, Springer, New York, Heidelberg, Dordrecht, London, vol. 1, pp. 442–454, 2013.

[11] M. J. Madou and S. R. Morrison, Chemical Sensing with Solid State Devices, Academic Press, London, vol. 19, pp. 342–348, 1989.

[12] P. Singh, R. Kumar, and R. K. Singh, "Progress on transition metal-doped ZnO nanoparticles and its application," *Ind. Eng. Chem. Res.*, vol. 58, pp. 17130–17163, 2019.

[13] L. Cheng, S. Y. Ma, X. B. Li, J. Luo, W. Q. Li, F. M. Li, Y. Z. Mao, T. T. Wang, and Y. F. Li, "Highly sensitive acetone sensors based on Y-doped SnO_2 prismatic hollow nanofibers synthesized by electrospinning," *Sens. Actuators B: Chem.*, vol. 200, pp. 181–190, 2014.

[14] M. Hjiri, R. Dhahri, K. Omri, L. E. Mir, S. G. Leonardi, N. Donato, and G. Neri, "Effect of indium doping on ZnO-based gas sensor for CO," *Mater. Sci. Semicond. Process.*, vol. 27, pp. 319–325, 2014.

[15] S. A. Hakim, Y. Liu, Y. Lu, and W. Chen, "Room temperature highly selective ethanol sensing behavior of hydrothermally prepared Te-V_2O_5 nanorod nanocomposites," *Mater. Sci. Semicond. Process.*, vol. 31, pp. 630–638, 2015.

[16] R. C. Singh, O. Singh, M. P. Singh, P. S. Chandi, and R. Thangaraj, "Sensing behavior of nanosized zinc-tin composite oxide towards liquefied petroleum gas and ethanol," *Mater. Res. Bull.*, vol. 45, no. 9, pp. 1162–1164, 2010.

[17] C. Y. Tee, G. K. Das, Y. Zhang, and T. T. T. Yang, "Rare earth nanophosphors in light-emitting diodes," in *Rare Earth Nanotechnology*, Singapore: Pan Stanford Publishing Pte. Ltd., pp. 203–244, 2012.

[18] J. Steckl, J. H. Park, and J. M. Zavada, "Prospects for rare earth doped GaN lasers on Si," *Mater. Today*, vol. 10, pp. 20–27, 2007.

[19] V. Kumar, O. M. Ntwaeaborwa, J. Holsa, D. E. Motaung, and H. C. Swart, "The role of oxygen and titanium-related defects on the emission of TiO_2:Tb^{3+} nano-phosphor for blue lighting applications," *Opt. Mater.*, vol. 46, pp. 510–516, 2015.

[20] W. Shide, L. Chao, W. Wei, W. Huanxin, S. Yangliang, Z. Youqi, and L. Lingzhen, "Nd-doped SnO_2: characterization and its gas sensing property," *J. Rare Earths*, vol. 28, pp. 171–173, 2010.

[21] Q. Xiang, G. Meng, Y. Zhang, J. Xu, P. Xu, Q. Pan, and W. Yu, "Ag nanoparticle embedded-ZnO nanorods synthesized via a photochemical method and its gas sensing properties," *Sens. Actuators B: Chem.*, vol. 143, pp. 635–640, 2010.

[22] H. S. Woo, C. H. Kwak, J. H. Chung, and J. H. Lee, "Highly selective and sensitive xylene sensors using Ni-doped branched ZnO nanowire networks," *Sens. Actuators B: Chem.*, vol. 216, pp. 358–366, 2015.

[23] S. Huang, T. Wang, and Q. Xiao, "Effect of Fe doping on the structural and gas sensing properties of ZnO porous microspheres," *J. Phys. Chem. Solids*, vol. 76, pp. 51–58, 2015.

[24] D. Han, J. Yang, F. Gu, and Z. Wang, "Effects of rare earth elements doping on ethanol gas sensing performance of three-dimensionally ordered macroporous In_2O_3," *RSC Adv.*, 2013.

[25] O. Singh and R. C. Singh, "Enhancement in ethanol sensing response by surface activation of ZnO with SnO_2," *Mater. Res. Bull.*, vol. 47, no. 3, pp. 557–561, 2012.

[26] S. Bai, T. Guo, Y. Zhao, J. Sun, D. Li, A. Chen, and C. C. Liu, "Sensing performance and mechanism of Fe-doped ZnO microflowers," *Sens. Actuators B: Chem.*, vol. 195, pp. 657–666, 2014.

[27] A. Mirzaei, J. H. Kim, H. W. Kim, and S. S. Kim, "Resistive-based gas sensors for detection of benzene, toluene, and xylene (BTX) gases: A review," *J. Mater. Chem. C*, vol. 6, pp. 4342–4370, 2018.

[28] H. T. Derraz, N. Benramdane, D. Nacer, A. Bouzidi, and M. Medles, "Investigations on $Zn_xCd_{1-x}O$ thin films obtained by spray pyrolysis," *Sol. Energy Mater. Sol. Cells*, vol. 73, pp. 249–259, 2002.

[29] R. V. Kumar, K. J. Lethy, P. R. A. Kumar, R. R. Krishnan, N. V. Pillai, V. P. M. Pillai, and R. Philip, "Effect of cadmium oxide incorporation on the microstructural and optical properties of pulsed laser deposited nanostructured zinc oxide thin films," *Mater. Chem. Phys.*, vol. 121, pp. 406–413, 2010.

[30] M. I. Khan, K. A. Bhatti, R. Quindeel, L. G. Bousiakou, N. Alonizan, and F. Alam, "Investigations of the structural, morphological, and electrical properties of multilayer ZnO/TiO_2 thin films deposited by sol-gel technique," *Results Phys.*, vol. 6, pp. 156–160, 2016.

[31] J. K. Rajput, T. K. Pathak, V. Kumar, M. Kumar, and L. P. Purohit, "Annealing temperature dependent investigations on the nano-cauliflower-like structure of CdO thin film grown by sol-gel method," *Surf. Interfaces*, vol. 6, pp. 11–17, 2017.

[32] W. Guo, T. Liu, R. Sun, Y. Chen, W. Zeng, and Z. Wang, "Hollow, porous, and yttrium functionalized ZnO nanospheres with enhanced gas-sensing performances," *Sens. Actuators B: Chem.*, vol. 178, pp. 53–62, 2013.

[33] V. S. Rana, J. K. Rajput, T. K. Pathak, and L. P. Purohit, "Multilayer MgZnO/ZnO thin films for UV photodetectors," *J. Alloys Compd.*, vol. 764, pp. 724–729, 2018.

[34] M. Thirumoorthi and J. H. J. Prakash, "Structural, morphological characteristics and optical properties of Y-doped ZnO thin films by sol-gel spin coating method," *Superlattices Microstruct.*, vol. 85, pp. 237–247, 2015.

[35] V. S. Rana, J. K. Rajput, T. K. Pathak, and L. P. Purohit, "Cu sputtered Cu/ZnO Schottky diode on fluorine-doped tin oxide substrate for optoelectronic applications," *Thin Solid Films*, vol. 679, pp. 79–85, 2019.

[36] S. Ilicon, M. Caglar, and Y. Caglar, "Sn doping effects on the electro-optical properties of sol-gel derived transparent ZnO films," *Appl. Surf. Sci.*, vol. 256, pp. 7204–7210, 2010.

[37] M. Caglar, Y. Caglar, S. Aksoy, and S. Silicon, "Temperature dependence of the optical bandgap and electrical conductivity of sol-gel derived undoped and Li-doped ZnO films," *Appl. Surf. Sci.*, vol. 256, pp. 4966–4971, 2010.

[38] G. K. Upadhyay, J. K. Rajput, T. K. Pathak, H. C. Swart, and L. P. Purohit, "Photoactive CdO: TiO_2 nanocomposites for dyes degradation under visible light," *Mater. Chem. Phys.*, vol. 253, pp. 123191, 2020.

[39] Z. Liu, B. Liu, W. Xie, H. Li, R. Zhou, Q. Li, and T. Wang, "Enhanced selective acetone sensing characteristics based on Co-doped WO_3 hierarchical flower-like nanostructures assembled with nanoplates," *Sens. Actuators B: Chem.*, vol. 235, pp. 614–621, 2016.

[40] D. R. Miller, S. A. Akbar, and P. A. Morris, "Nanoscale metal oxide-based heterojunctions for gas sensing: A review," *Sens. Actuators B: Chem.*, vol. 204, pp. 250–272, 2014.

Evaluation of Radiation and Radiation Protection Awareness Level Among Radiographers Working in Public and Private Hospitals of Gilgit-Baltistan (GB), Pakistan

Muhammad Raza[a*] and Basharat Hussain[b]

[a]*Department of Physics Karakoram International University Gilgit-Baltistan.*

[b]*Department of Psychology & Human Development Karakoram International University Gilgit-Baltistan.*

A B S T R A C T

Radiation, in terms of ionizing or non-ionizing form, has always had a pivotal role in the field of medical diagnosis and treatment. Its uses also contain a lot of risk and increase the risk of cancer. Numerous challenges with radiation awareness, hazards, protections, safety measures, and dosimetry usage need to be evaluated in radiology departments of public and private hospitals located in Gilgit-Baltistan (GB). This study aims to assess the radiation protection awareness and practices among radiographers working in public and private hospitals of Gilgit-Baltistan (GB). This study included 18 public sectors and 21 private sector hospitals (total of 39) in GB. Mostly general radiography, computed tomography, and dental radiography are used in all hospitals included in this study, along with that some hospitals also using mammography, MRI, and interventional radiology. All hospitals included in this study have limited resources of radiation facilities. This Cross-sectional study was carried out using a validated questionnaire, which was completed by 74 (67 male & 7 female) radiographers. The data was collected through purposive sampling and analyzed using Statistical Package for Social Sciences (SPSS), version 21.0. This study concludes that 93.2 % of radiographers are well-aware that X-ray emits ionizing radiation, but only 36.5 %, and 32.4.0%, respectively, think that Ultrasound and MRI emit ionizing radiation. And 97.3 % of radiographers are aware of the radiation sensitivity of the Human Reproductive Organs.

Keywords: Radiation Protection, Computed tomography, Mammography, Demographic information, Radiography

1. Introduction

Radiation is energy spread out from a source through waves or particles. Natural radiation comes from several naturally occurring radioactive elements in the environment [1-3].

X-ray is one of the major types of radiation, and its applications are increasing day by day in medicines for diagnostic and therapeutic purposes from the day first of its discovery. Radiation from medical applications represents most radiation doses from artificial sources to which workers and the public are exposed [4, 5]. It is the consequence of the recent advancement in imaging technology. Whereas the uses of ionizing radiation revolutionized medical science, it is a double-edged sword since it is a potential source of health hazards. Globally, the developing countries carry out approximately 3.6 billion imaging annually, resulting in a 70% rise in collective effective dose attributed to medical diagnostic imaging. Exposure to ionizing radiation can cause harmful biological effects in living organisms, including DNA damage, genetic mutations, leading risk of cancer [5-8].

Physicians' and radiologists' awareness of radiation exposure during diagnostic and therapeutic procedures is important. This awareness becomes more crucial as medical imaging technology expands [9-11].

Radiation exposure has health risks for both patients and medical workers. Unnecessary radiation exposure should be discouraged, as it increases the rates of cancer growth. Research shows that insufficient knowledge of the harmful effects of ionizing radiation and safety protections caused multiple examinations, increasing exposure time for patients and workers [6, 15, 16]. Physicians and radiation workers should work collectively to minimize radiation risk related to

medical imaging. Medical personnel not only rationalize the x-ray exposure before performing radiological examination but also protect themselves and the public from radiation hazards, and sometimes, this practice changes from place to place [12, 17, 20]. It demands adequate knowledge of radiation, its harmful effects, and radiation protection [18, 19].

For occupational exposure, the International Commission on Radiological Protection has established dose limits and recommended 20 millisieverts (mSv) per year, averaged over five years. However, the annual occupational exposure limit is 50 mSv. Likewise, the US Nuclear Regulatory Commission recommended less than 5 mSv cumulative fetal exposure during pregnancy [24].

Evaluation of knowledge level is critical to classify any deficiencies to overcome them and ultimately diminish radiation risks to all taking part in the process of radiologic examination.

Gilgit-Baltistan (GB), located in Pakistan's extreme north, encounters unique healthcare challenges due to its remote location. Despite limited facilities, the region has witnessed significant advancements by establishing various public and private health units equipped with medical imaging facilities.

However, research on radiation hazards and protection measures among medical workers in GB remains rare. This knowledge gap demands an assessment of radiation awareness among radiographers in GB's hospitals.

This study aims to assess the awareness of radiation protection and practices among radiographers working in public and private hospitals in Gilgit-Baltistan (GB).

---

* Corresponding author: raza.physics@kiu.edu.pk

2. Methodology

This study carried out on medical imaging technologists / radiographers working in different public and private hospitals in Gilgit-Baltistan (GB), Pakistan. This study is a short cross-sectional survey-based design on a structured self-administered questionnaire. The data were gathered from medical imaging technologists/radiographers through a self-administered questionnaire developed based on suggestions provided by five experts, including three doctors and two researchers with experience in radiological imaging. The questionnaire consisted of 25 questions, assessing respondents' demographics, awareness of radiation hazards, knowledge of protective measures, and overall radiation literacy. The questionnaire was categorized into two major sections: i) Demographic information, including sex, age, experience, and education level, etc. ii) The second section consists of 21 questions regarding radiation awareness, radiation protection knowledge, and imaging device knowledge.

The data was collected through purposive sampling from 74 radiographers of 39 hospitals (18 public sector and 21 private sector) of GB. Participants were handed out hard copies of the questionnaire by the author himself after proper consent to participate in the survey. Where needed, they understood the questionnaire or were interviewed in Urdu and their local languages.

All public sector hospitals are run under the Gilgit-Baltistan government, and each hospital is supervised by a Medical Superintendent (MS). In contrast, all private hospitals are run under the concerned Board of Directors (BOD) and supervised by a Medical Officer (MO). To ensure ethical standards, we obtained the necessary institutional and formal approval from the relevant MS or MO. Additionally, we sought permission from the respective heads of each healthcare unit to ensure compliance with all regulations and protocols, as there were no separate ethical committees.

The data obtained were analyzed using the Statistical Package for Social Sciences (SPSS), version 21.0, and all results are shown in the results section. To achieve accurate results about radiographers' knowledge and awareness, a numerical value of 1 for the correct answer and 0 for the wrong answer was assigned to each answer. Ultimately, the total score of each section was calculated in terms of 100.

3. Results

This research includes 74 radiographers from 39 public and private hospitals in GB, Pakistan. Table 1 indicates that there are 67 (90.5 %) males and 7 (9.5 %) females. 44.5 % of radiographers with working experience of 5 - 10 years fall in the age group of 31 – 40 years old. 73 % radiographers have vocational high school certificates, and only 27 % have university level education. Out of these 74, 51.4 % of radiographers were from public sector institutions these 74, 51.4 % of radiographers were from public sector institutions,

and 48.6 % were from private sector institutions, almost from all districts of GB. The results are entered into the following tables.

3.1 Demographic Information of Participants

Table 1. Demographic details of the study variables.

Variable	n	%		n	%
Gender			Institution		
Male	67	90.5	Public	38	51.4
Female	7	9.5	Private	36	48.6
Work Experiences			Districts		
< 5 years	19	25.7	Gilgit	22	29.7
5 - 10 years	33	44.6	Skardu	27	36.5
> 10 years	22	29.7	Ghanche	10	13.5
Age			Hunza	4	5.4
18 - 30	24	32.4	Kharmang	6	8.1
31 - 40	29	39.2	Shigar	1	1.4
> 40	21	28.4	Astore	4	5.4
Education					
Vocational High School	54	73.0			
University associate degree	20	27.0			

3.2 Response to Tissue Radiation Sensitivity and Radiation Awareness Per Imaging Modality

Table 2. Tissue radiation sensitivity (assessment of basic knowledge either different organ is radiation sensitive/resistant)

Variable	Radiation Sensitive (Yes)		Radiation resistant (Yes)	
	n	%	n	%
Reproductive Organ	72	97.3	2	2.7
Central Nervous System	68	91.9	6	8.1
Bone Marrow	71	95.9	3	4.1
Thyroid Gland	69	93.2	5	6.8

Radiation sensitivity is the relative susceptibility of cells, tissue and organs to the harmful effects of ionizing radiation. It varies from tissue and organs to organs. Human reproductive organs are more radiosensitive than those of bones and teeth. Radiation has some prompt and delayed effects on tissues and organs of the human body according to its radiation sensitivity. Radiographers should know which human organ is more radiosensitive or radio resistant. Table 2 declared that 97.3 % of radiographers are aware about radiation sensitivity of the Human Reproductive Organs. Respectively 91.9 %, 95.9 %, and 93.2 % of radiographers avowed that Bone Marrow, Central Nervous System, and Thyroid Gland are radiation susceptible.

3.3 Responses Patterns by Imaging Modality, Expertise, and Protective Equipment Use, Categorized Education Level

Table 3. Imaging Modality, Expertise, and Protective equipment use.

Variable	Yes		No	
	n	%	n	%
Does X-Ray emit harmful radiation?	69	93.2	5	6.8
Does ultrasound emit harmful radiation?	27	36.5	47	63.5
Does computed tomography emit harmful radiation	41	55.4	33	44.6
Does Magnetic resonance imaging emit harmful radiation?	24	32.4	50	67.6
Does Mammography emit harmful radiation?	34	45.9	40	54.1
Imaging expertise obtained at school?	15	20.3	59	79.7
Imaging expertise obtained with own effort?	23	31.1	51	68.9
Imaging expertise obtained from college?	68	91.9	6	8.1
Do you use lead aprons?	44	59.5	30	40.5
Do you use lead screen?	42	56.8	32	43.2
Do you use other protective equipment (Gloves or Collar etc.)	33	44.6	41	55.4

Table 3 identified that 93.2 % of radiographers are aware that the X-Ray emits harmful/ionizing radiation. Respectively 55.4 %, 45.9%, 36.5%, and 32.4% of radiographers marked that Computed Tomography (CT), Mammography, Ultrasound, and MRI emit dangerous / ionizing radiation. 91.9 percent of the radiographers in the hospitals of GB took their imaging expertise from colleges, and the rest acquired their expertise by their own efforts or school level. Overall radiographers are aware of radiation hazards and radiation shielding. There are only 44.6 percent who took necessary protective measures (gloves, collar, etc.), while 44 (59.5 %) & 42 (56.8 %) utilized lead aprons and lead screens respectively.

3.4 General Knowledge Responses Regarding Radiation

Table 4 revealed that most radiographers working in different hospitals in GB believe that staff has adequate knowledge of radiation safety and protection. More than half of the participants know medical physics imaging and symbols used for ionizing and non-ionizing radiation. Most radiographers know X-ray warning symbols used for

pregnant/expected women. Most radiographers do not use their dosimeter as that may not be available.

Table 4. General awareness of radiation.

Variable	Yes		No	
	n	%	n	%
Do you believe staff have adequate knowledge of radiation safety and protection?	67	90.5	7	9.5
Do you have enough knowledge of medical imaging physics?	37	50.0	37	50.0
Do you know what the symbol uses for ionizing radiation?	39	52.7	35	47.3
Do you know the symbol used for nonionizing radiation (radio frequency) radiation?	38	51.4	36	48.6
Do you know the X-ray warning symbol for pregnant or expected women?	50	67.6	24	32.4
Do you use a personal dosimeter?	15	20.3	59	79.7

Table 5 shows a socio-demographic comparison of public and private hospitals in GB. The sample of 38 (51.4%) public hospitals and 36 (48.6%) private hospitals. Most participants were aware that X-rays emit harmful radiation (Public hospital = 94.7% and Private hospital = 91.7%). Furthermore, participants agreed that ultrasound does not emit dangerous radiation (Public hospital = 65.8% and Private hospital = 80.6%). Participants reported that they obtained imaging expertise from their efforts (Public hospital = 60.5% and private hospital = 77.8%). Furthermore, most of the participants reported that they obtained imaging expertise at college (Public hospitals = 94.7% and Private hospitals = 88.9%). The chi-square ($\chi2$) test was used to determine the statistical significance of various parameters. Among them, the only statistically significant result was observed for the parameter 'Imaging expertise obtained with own effort,' with χ^2 = 2.59 and P = 0.04. This indicates that many participants reported acquiring their imaging expertise through self-learning rather than formal training. All other parameters yielded higher P-values and lower χ^2 values, indicating non-significant results. The confidence interval for the decision further supports these findings.

Table 5: Socio-demographics

	Public		Private		χ^2	p-value
	Yes n (%)	No n (%)	Yes n (%)	No n (%)		
Does X-Ray emit harmful radiation?	36 (48.6)	2 (2.7)	33 (44.6)	3 (4.1)	0.28	0.59
Does ultrasound emit harmful radiation?	13 (17.6)	25 (20.3)	7 (9.5)	29 (39.2)	2.04	0.15
Does computed tomography emit harmful radiation	24 (32.4)	14 (18.9)	21 (28.4)	15 (20.3)	0.18	0.67
Does Magnetic resonance imaging emit harmful radiation?	16 (21.6)	22 (29.7)	12 (16.2)	24 (32.4)	0.61	0.44
Does Mammography emit harmful radiation?	20 (27.0)	18 (24.3)	20 (27.0)	16 (21.6)	0.06	0.80
Imaging expertise obtained at school?	6 (8.1)	32 (43.2)	9 (12.2)	37 (50.0)	0.97	0.33
Imaging expertise obtained with own effort?	15 (20.3)	23 (31.1)	8 (10.8)	28 (37.8)	2.59	0.04*
Imaging expertise obtained from college?	36 (48.6)	2 (2.7)	32 (43.2)	4 (5.4)	0.85	0.36
Do you use lead aprons?	24 (32.4)	14 (18.9)	20 (27.0)	16 (21.6)	0.44	0.51
Do you use lead screen?	21 (28.4)	17 (23.0)	21 (28.4)	15 (20.3)	0.07	0.79
Do you use other protective equipment (Gloves, Collar etc.)	17 (23.0)	21 (28.4)	16 (21.6)	20 (27.0)	0.01	0.98

4. Discussion

This study aimed to examine the knowledge level of radiation, and radiation protection amongst radiographers working in different public and private hospitals of GB. The literature revealed that there are various researches about radiation safety awareness of healthcare workers in different parts of the world [7]. However, no such study was performed in GB to evaluate the radiographer's knowledge level regarding radiation dose and protection. As radiographers have a key role in the radiation department [15], his/her knowledge level about radiation and its protection is a prime need. This study is the first attempt to examine the knowledge level and awareness about radiation, radiation hazards, and its protection. This study includes 74 radiographers working in the whole of GB. The questions were designated to assess general awareness regarding radiation, its types, and its protections. A limitation of this study is that there are fewer radiographers. Another is their lower education level, which may affect the response to each question.

Medical imaging is now an integral part of practice, and critical for accurate diagnosis and effective treatment. Radiographers have a major role in radiation imaging, so radiation protection is radiographers' professional responsibility. Furthermore, it is vital to recognize the potential risk of radiation exposure in the process and prioritize radiation protection awareness. The patient and the radiation workers must take the minimum and permissible dose [7, 21]. If radiographers are not aware of radiation and radiation protection, then the patients may be irradiated with unjustified radiation doses [14, 15]. It is essential to do a comprehensive benefit-risk assessment of ionizing radiation use.

According to this research, radiographers hold different degrees, age groups, and working experiences. 91.5 % of the population has acquired imaging expertise from colleges, and 75 % of radiographers have more than 5 years of working experience. The result revealed that 93.2 % of radiographers know that X-ray emits harmful/ionizing radiation. The results of some other parameters identified that the knowledge level of radiographers holding higher degrees and experience was higher than others. Interestingly high number of radiographers mention that MRI and Ultrasound do not emit ionizing radiation, which is an indication of basic knowledge of physics for understanding imaging technologies, for college-educated radiographers (Table 3). Like Sharma et al. [13] this research also concluded that awareness level highly depends on working experience and educational background. There are only 59.5 %, 56.8 %, and 44.6 % radiographers who used simultaneously lead aprons, lead screens, and protective equipment like gloves & collars, etc. (Table 3). Radiation protection knowledge among radiographers should be kept on top priority and they should have full control of radiation procedures. It is their responsibility that they use sufficient protective measures and follow safe radiation practice. In case there may increase the chance of cancer risk and other health problems among radiographers.

Although this research was conducted in one of the least developed and remotest regions of Pakistan, the results (in both basic radiation awareness and radiation protection cases majority questions marked correct by more than 60% of radiographers) showed adequate knowledge about radiation and radiation protection, and obviously, the facilities and the protective measures are substandard and not satisfactory (we have seen that due to unavailability of facilities almost 80% radiographers not used personal dosimeters and more than 50% not use other protective equipment like Gloves, collar etc.) as compared to other parts of Pakistan and developed countries (Table 3 and Table 4).

In exploring general awareness regarding radiation, it was found that out of 74 radiographers, 37, 39, 38, and 50, respectively, know about medical imaging physics, symbols of ionizing / nonionizing radiation, and X-ray warning symbols for expected women. Only 15 radiographers use personal dosimeters (Table 4). Both public and private hospital radiographers were given approximately the same responses for all fields (Table 5).

Insufficient clinical examination practice has been identified as a contributing factor to the increased use of medical imaging, as evidenced by several studies [7, 22, 23]. These faults can also lead to the harmful effects of unwanted radiation exposure among healthcare professionals and inappropriate application of radiation doses in imaging practices. So, it is recommended that training courses regarding the diagnostic application of ionizing radiation be arranged to enhance the awareness level of radiographers. It is also recommended that heads of institutions should provide personal dosimeters to all radiographers and monitor them regularly. The radiographers are responsible for working under the guidelines issued by different national and international organizations to create safer situations for imaging.

5. Conclusion

Based on the outcomes of this study, it is concluded that the majority radiographers working in different public and private hospitals of GB are aware of the basics of radiation and radiation protection. But majority neither use protective equipment nor use any personal dosimeters. This failure to use protective measures may lead to excessive radiation exposure to themselves and patients, which may increase the chance of cancer etc. The awareness level of the radiographers mostly depends on working experience and educational backgrounds. Hospitals and concerned authorities must offer academic and professional development opportunities to radiographers in radiation protection and safety.

6. Research Funding

7. Conflict of Interest

Authors have no conflict of interest.

8. Acknowledgement

References

[1] M. Tschurlovits, "What is ionizing radiation (IAEA-TECDOC-976)," Int. At. Energy Agency (IAEA), 1997.

[2] S. Özkan, G. Aba, and B. Tekinsoy, "The importance of radiation safety in terms of hospital administration and research on the awareness stage of radiology technicians," J. Acad. Res. Med., vol. 6, no. 3, 2016.

[3] M. A. Almanie, "Radiation safety awareness among healthcare workers in King Saud University Medical City," J. Positive Sch. Psychol., vol. 6, no. 9, 2022.

[4] R. Tinker, J. Abramowicz, E. Karabetsos, S. Magnusson, R. Matthes, M. Moser, and E. V. Deventer, "A coherent framework for non-ionising radiation protection," J. Radiol. Prot., vol. 42, no. 1, 2022.

[5] M. Raza, S. M. A. Jafri, Z. Uddin, S. Memon, and S. Ali, "A multi-center shielding verification study for radiotherapy linac bunkers in Karachi, Pakistan," Radiat. Prot. Dosim., vol. 176, no. 4, 2017.

[6] L. Hardell, M. Nilsson, T. Koppel, and M. Carlberg, "Aspects on the International Commission on Non-Ionizing Radiation Protection (ICNIRP) 2020 guidelines on radiofrequency radiation," J. Cancer Sci. Clin. Ther., vol. 5, no. 2, pp. 250–285, 2021.

[7] S. Aras, I. O. Tanzer, and T. Ikizceli, "A survey study of radiation protection awareness among radiology technicians in Mogadishu, Somalia," Radiat. Prot. Dosim., vol. 192, no. 1, pp. 36–40, 2020.

[8] C. Khamtuikrua and S. Suksompong, "Awareness about radiation hazards and knowledge about radiation protection among healthcare personnel: A quaternary care academic center–based study," SAGE Open Med., vol. 8, 2020.

[9] International Commission on Non-Ionizing Radiation Protection, "ICNIRP guidelines on limits of exposure to laser radiation of wavelengths between 180 nm and 1,000 μm," Health Phys., vol. 105, no. 3, pp. 271–295, 2013.

[10] S. Hayashi, M. Takenaka, H. Kogure, T. Yakushijin, H. Maruyama, and Y. Hori, "A questionnaire survey on radiation protection among 282 medical staff from 26 endoscopy-fluoroscopy departments in Japan," DEN Open, vol. 1, no. 1, 2021.

[11] M. Alhasan, M. Abdelrahman, H. Alewaidat, and Y. Khader, "Radiation dose awareness of radiologic technologists in major Jordanian hospitals," Int. J. Radiat. Res., vol. 14, no. 2, 2016.

[12] M. Malik, M. U. Din, M. Arfat, and A. Kumar, "A questionnaire survey of radiation hazards and protection among medical and imaging technology students," Int. J. Recent Sci. Res., vol. 13, no. 3, pp. 526–529, 2022.

[13] B. Sharma, S. Singh, S. Mandal, and N. Poudel, "Knowledge of radiation exposure and its risk among radiographers and radio technologists," J. Gandaki Med. Coll.-Nepal, vol. 12, no. 2, pp. 17–22, 2019.

[14] S. Maharjan, K. Parajuli, S. Sah, and U. Poudel, "Knowledge of radiation protection among radiology professionals and students: A medical college-based study," Eur. J. Radiol. Open, vol. 7, 2020.

[15] F. Paolicchi et al., "Assessment of radiation protection awareness and knowledge about radiological examination doses among Italian radiographers," Insights Imaging, vol. 7, no. 2, pp. 33–42, 2016.

[16] P. Moghimi, K. Hajimiri, F. Saghatchi, and H. Rezaeejam, "Assessment of the awareness level of radiation protection among radiographers working in the medical imaging wards of the hospitals in Zanjan, Iran," Radiat. Prot. Dosim., vol. 194, no. 3, pp. 97–103, 2021.

[17] A. Szarmach et al., "Radiation safety awareness among medical staff," Pol. J. Radiol., vol. 80, pp. 57–65, 2015.

[18] A. S. Shah, N. Begum, S. Nasreen, and A. Khan, "Assessment of radiation protection awareness levels in medical radiation science technologists—a pilot survey," J. Postgrad. Med. Inst., vol. 21, no. 3, 2007.

[19] A. R. S. Khan, "Knowledge of radiographers about radiation protection procedures," J. Postgrad. Med. Inst., vol. 20, 2006.

[20] International Commission on Radiological Protection, "ICRP recommendations of the International Commission on Radiological Protection," Ann. ICRP, vol. 21, no. 1, 1990.

[21] A. Kocyigit et al., "The knowledge level medical personnel have ten radiation exposure during common radiologic examinations," Pamukkale Med. J., vol. 7, no. 2, pp. 137–142, 2014.

[22] N. Brown and L. Jones, "Knowledge of medical imaging radiation dose and risk among doctors," J. Med. Imaging Radiat. Oncol., vol. 57, pp. 8–14, 2013.

[23] A. Yurt, B. Cavusoglu, and T. Gunay, "Evaluation of awareness on radiation protection and knowledge about radiological examinations in healthcare professionals who use ionized radiation at work," Mol. Imaging Radionucl. Ther., vol. 23, pp. 48–53, 2014.

[24] S. M. E. Allam, M. M. A. Algany, and Y. I. A. Khider, "Radiation safety compliance awareness among healthcare workers exposed to ionizing radiation," BMC Nurs., vol. 23, no. 208, 2024.

Re-Analysis of Neutron Capture on ^{90,92}Zr at S-Process Energies

Zain Ul Abideen[1*], Abdul Kabir[1,2]

[1]*Department of Space Science, Institute of Space Technology, Islamabad 44000, Pakistan*

[2]*Space and Astrophysics Research Lab (SARL), National Center of GIS and Space Applications (NCGSA), Islamabad 44000, Pakistan*

ABSTRACT

The Maxwellian-averaged cross sections (MACS) for the ^{90,92}Zr(n,γ)^{91,93}Zr processes were analyzed within the framework of the Hauser-Feshbach theory, making use of microscopic nuclear inputs. The effects of nuclear level densities and photon strength functions were studied for the mentioned isotopes. A comparison with the experimental data and KADoNiS was conducted at the s-process energies. Good agreement was achieved for both nuclear reactions under study. Finally, making use of the best-fit microscopic nuclear ingredients, we calculated the thermonuclear reaction rates, which show a reduction from the previously reported calculations.

Keywords: Nucleosynthesis, AGB stars, Massive stars, Statistical model, Nuclear level densities, Thermonuclear reaction rates

Introduction

The production of elements beyond the iron-peak occurs mainly through the neutron capture reactions. These are classified into *s-* and *r-*processes based on the neutron capture times [1]. The (slow) *s-*process is said to occur when the time for neutron capture is relatively greater than the time for beta decay. Under this constraint, the target nucleus for the neutron capture is ensured to be stable. This leads to the production of many isotopes being inaccessible through the *s-*process, and is in contrast to the (rapid) *r-*process, where the neutron capture times are lower than the beta decay times of the target nuclei. Nevertheless, the origin of about half of the elements heavier than iron, from *A*~56-204, can be attributed to the *s-*process [2]. There also exist approximately 30 stable, proton-rich nuclei known as the *p-*nuclei. These are hypothesized to be produced by the so-called *p-*process where their production is initiated by photodisintegration reactions on the products of neutron capture processes [3].

The energy production and the elemental synthesis in main-sequence stars are driven by the charged particle-induced reactions taking place inside their cores. This process can carry nucleosynthesis till iron (Fe) during later evolutionary stages, which has the highest binding energy per nucleon. After it, the Coulomb barrier becomes too large for these reactions to be sustained, and nucleosynthesis can only predominantly occur through neutrons. The *s-*process can occur in both low mass and massive stars. The main component of the *s-*process, responsible for the production of elements from A~90-204, occurs in low-mass AGB (asymptotic giant branch) stars, whereas the weak component responsible for the production of elements from the iron-peak nuclides to *A*~90, occurs in massive stars. The two components are distinguished based on the neutron sources they employ. In massive stars, the ^{22}Ne(α,n)^{25}Mg reaction produces a steady source of neutrons, and is hypothesized to occur during the helium-core burning and the carbon-shell burning phases [4]. In low-mass AGB stars, the temperature-dependent ^{22}Ne(α,n)^{25}Mg reaction rate is not high enough, and the neutron production is hypothesized to occur mainly through the ^{13}C(α,n)^{16}O process, which occurs in the intershell region. All AGB stars are expected to produce elements from mass numbers *A*~90-140, whereas only low-metallicity stars are hypothesized to create heavier elements (till *A*~204) [2].

This study focuses on the capture cross sections of the two zirconium (Zr) isotopes under investigation. Progress in theoretical modeling and experimental techniques has allowed researchers to probe nuclei and gain a better understanding of the production of heavier elements in stars. Both ^{90}Zr and ^{92}Zr are key to the production of heavier elements as they are associated with the first *s-*process peak in the abundance distribution around *A*=90. The isotopes share the magic and nearly magic number of neutrons (50, 52), and thus their cross sections add to the initial bottleneck from the iron-peak nuclides to beyond. The most recent experimental measurements for (n,γ) Maxwellian-averaged cross sections (MACS) were done by Tagliente *et al.* [5, 6]. The MACS were determined by folding the capture cross sections with the stellar spectra over a large neutron energy range. Their analyses lead to the reduction of the *s-*component of ^{92}Zr. Recently, Kabir *et al.* [4] analyzed the MACS of the ^{90,92}Zr(n,γ)^{91,93}Zr processes using phenomenological models for optical potential, nuclear level density, and radiative strength (with the exception of the Gogny D1M model). They compared their finding with the

available experimental data, and their adjusted results were in good agreement. They further calculated the thermonuclear reaction rates using the best-fit model combinations based upon the least calculated percentage error at the typical s-process temperature.

The phenomenological models rely on the introduction of free parameters, which can be adjusted to constrain the theoretical predictions. The primary goal of these models is to produce highly accurate results. In contrast, microscopic models prioritize a precise representation of underlying physics using minimal free parameters [7]. The phenomenological models are most suited for the applied domain of nuclear sciences, but for nuclear astrophysics, where often high extrapolation capabilities are required, microscopic models are preferable. In the present study, we aim to investigate the predictions of microscopic nuclear inputs, including optical potential, level densities, and the radiative strengths, for the Maxwellian-averaged cross sections and the thermonuclear reaction rates. In the next sections, the framework and the discussions are presented, leading to the conclusion.

Theoretical Framework

Experimental data only cover a limited portion of the total nuclear data required for nucleosynthesis calculations. Nuclei with relevance to astrophysics generally have exotic origins and, thus, are difficult to study experimentally [8]. Only theoretical predictions, constrained by the available measurements, can be used to fill in the gaps. Neutron capture reactions beyond the iron-peak are studied within the framework of the Hauser-Feshbach theory, also known as the statistical model [9]. The capture cross sections are directly related to the transmission coefficients in the entrance and all exit channels. The transmission coefficients in the entrance channels are calculated using the optical model potential, which describes the interaction between the projectile and the target nucleus. For the case of capture reactions, the transmission coefficients for the emission of γ photons are given by the radiative strength functions. The nuclear level density needs to be folded in due to the large number of nuclear levels at excitation energies, when information about discrete levels is either missing or incomplete. The Hauser-Feshbach formula for binary cross section is given by

$$\sigma_{\alpha\alpha'}^{comp} = D^{comp} \frac{\pi}{k^2} \sum_{J=mod(l+s,1)}^{l_{max}+l+s} \sum_{\Pi=-1}^{1} \frac{(2J+1)}{(2I+1)(2s+1)}$$

$$\sum_{j=|J-I|}^{J+I} \sum_{l=|(j-s)|}^{j+s} \sum_{j'=|(J-I')|}^{J+I'} \sum_{l'=|(j'-s')|}^{j'+s'} \delta_\pi(\alpha)\delta_\pi(\alpha')$$

$$\frac{T_{\alpha lj}^J(E_a)\langle T_{\alpha' l'j'}^J(E_{a'})\rangle}{\sum_{\alpha'',l'',j''}\delta_\pi(\alpha'')\langle T_{\alpha''l''j''}^J(E_{a''})\rangle} W_{\alpha lj\alpha'l'j'}^J$$

where the following energy, angular momentum, and parity conservation laws need to be obeyed,

$$E_a + E_x + S_a = E_{a'} + E_{x'} + S_{a'} = E^{tot}$$
$$s + I + l = s' + I' + l' = J$$
$$\pi_o\Pi_o(-1)^l = \pi_f\Pi_f(-1)^{l'} = \Pi.$$

In the above equations, the symbols have the following meaning:

E_a is the energy of the projectile,

l is the orbital angular momentum of the projectile,

s is the spin of the projectile,

j is the total angular momentum of the projectile,

π_0 is the parity of the projectile,

$\delta_\pi(\alpha)$ is 1 if $(-1)^l\pi_0\Pi_0 = \Pi$, 0 otherwise to enforce parity conservation,

α is the designation of the channel for the initial projectile-target system:

$\alpha = \{a, s, E_a, E_x, I, \Pi_0\}$, where a and E_x are the type of the projectile and the excitation energy (which is usually zero) of the target nucleus, respectively,

l_{max} is the maximum l-value of the projectile,

S_a is the separation energy,

$E_{a'}$ is the energy of the ejectile,

l' is the orbital angular momentum of the ejectile,

s' is the spin of the ejectile,

j' is the total angular momentum of the ejectile,

π_f is the parity of the ejectile,

$\delta_\pi(\alpha')$ is 1 if $(-1)^{l'}\pi_f\Pi_f = \Pi$, 0 otherwise to enforce parity conservation,

α' is the designation of channel for the ejectile-residual nucleus final system:

$\alpha' = \{a', s', E_{a'}, E_x, I', \Pi_f\}$, where a' and E_x are the type of the ejectile and the residual nucleus excitation energy, respectively,

I is the spin of target nucleus,

Π_0 is the parity of target nucleus,

I' is the spin of residual nucleus,

Π_f is the parity of residual nucleus,

J is the total angular momentum of the compound system,

Π is the parity of the compound system,

D^{comp} is the depletion factor so as to take into account the pre-equilibrium and direct effects,

k is the wave number of the relative motion,

T is the transmission coefficient,

W is the correction factor for width fluctuation.

The preferred implementation of the Hauser-Feshbach theory was the TALYS 2.02 code [10]. It includes all reaction mechanisms involved in the study of light particle-induced nuclear reactions. The predictions of the code have been tested on many nuclei of astrophysical interest by many authors [3, 4, 11, 12]. For all nuclear inputs (optical models, level densities, and radiative strengths), both phenomenological and microscopic options are available. The microscopic option for the optical model includes the model of Jeukenne-Lejeune-Mahaux (JLM) [13]. For the level densities, the microscopic options include the Skyrme-Hartree-Fock-Bogoliubov model (SHFB), Gogny-Hartree-Fock-Bogoliubov model (GHFB), and the temperature-dependent Gogny-Hartree-Fock-Bogoliubov model (TGHFB). Finally, for the radiative strengths, the microscopic options include, but are not limited to, the Skyrme-Hartree-Fock-BCS model (HFBCS), the temperature-dependent relativistic mean-field model (TRMF), and the Gogny HFB+QRPA model with D1M interaction (D1M) [14].

The Maxwellian-averaged cross section (MACS) is used when the energies of projectiles follow a Maxwellian distribution, just as is the case with stellar environments. At the conditions in AGB and massive stars ($n_n \sim 10^9$ cm^{-3} and $kT \sim 30$ keV), both the Fermi-Dirac and the Bose-Einstein distributions reduce to the Maxwell-Boltzmann distribution [15]. Under these conditions, the high-energy tail of the Fermi-Dirac and Bose-Einstein distributions becomes negligible due to frequent particle interactions.

$$\langle\sigma\rangle(kT) = \frac{2}{\sqrt{\pi}(kT)^2}\int_0^\infty E\,\sigma(E)exp\left(\frac{-E}{kT}\right)dE,$$

where k is the Boltzmann constant, T is the temperature, $\sigma(E)$ is the capture cross section, and E is the projectile energy. The thermonuclear reaction rates per particle pair can be obtained from these MACS by multiplying with the mean velocity v_T at the temperature T [16].

Results and Discussions

To begin our analysis, we performed the computations for the MACS of ^{90}Zr(n,γ)^{91}Zr and ^{92}Zr(n,γ)^{93}Zr processes using the microscopic model combinations mentioned above.

The Zr isotopes employed in our study have the magic and nearly magic neutron numbers, which result in their low capture cross sections and consequently large abundances. For each of the nuclear reactions, the optical model was constrained, and the models for level densities and photon strengths were iterated. For low-energy neutrons as projectiles, the effects of changing the optical model can be ignored in favor of the other two components, the level densities and the photon strengths [11].

For the ^{90}Zr(n,γ)^{91}Zr reaction, the level density model was first fixed, and the photon strengths (HFBCS, TRMF, D1M) were iterated. The results are shown in *Figure 1*. First, we calculated the deviation from the experimental data at the typical *s*-process energy of kT=30 keV. At this energy, the MACS using the SHFB level densities were 17.97 mb (HFBCS), 16.13 mb (TRMF), and 16.99 mb (D1M). The measurement of Tagliente *et al.* [5] at this energy was 19.30 mb. The percentage differences were 7.4%, 19.6%, and 13.6%, respectively. Similarly, at kT=30 keV, the MACS using the GHFB level densities were 16.05 mb (HFBCS), 14.37 mb (TRMF), and 23.02 mb (D1M). The percentage differences were 20.2%, 34.3%, and 19.3%, respectively. Finally, at kT=30 keV, the MACS using the TGHFB level densities were 11.26 mb (HFBCS), 10.27 mb (TRMF), and 12.90 mb (D1M). The percentage differences were 71.4%, 87.9%, and 49.6%, respectively. Among all cases, the photon strengths combined with the SHFB level densities produced the best results, while the TGHFB level densities produced the worst.

The same set of level densities and photon strengths were employed for the ^{92}Zr(n,γ)^{93}Zr reaction. The results have been shown in *Figure 2*. At kT=30 keV, the MACS using the SHFB level densities were 34.31 mb (HFBCS), 29.31 mb (TRMF), and 27.71 mb (D1M). The measurement of Tagliente *et al.* [6] at this energy was 38.10 mb. The percentage differences were 11.0%, 29.9%, and 37.5%, respectively. Similarly, at kT=30 keV, the MACS using the GHFB level densities were 28.47 mb (HFBCS), 24.48 mb (TRMF), and 34.59 mb (D1M). The percentage differences were 33.8%, 55.6%, and 10.1%, respectively. Finally, at kT=30 keV, the MACS using the TGHFB level densities were 36.49 mb (HFBCS), 31.49 mb (TRMF), and 32.35 mb (D1M). The percentage differences were 4.4%, 20.9% and 17.8%, respectively. Among all cases, the photon strengths combined with the TGHFB level densities produced the best results, followed by the SHFB predictions. It is also noted that the agreement with the experimental data deviates by a factor of 1.5 at higher energies.
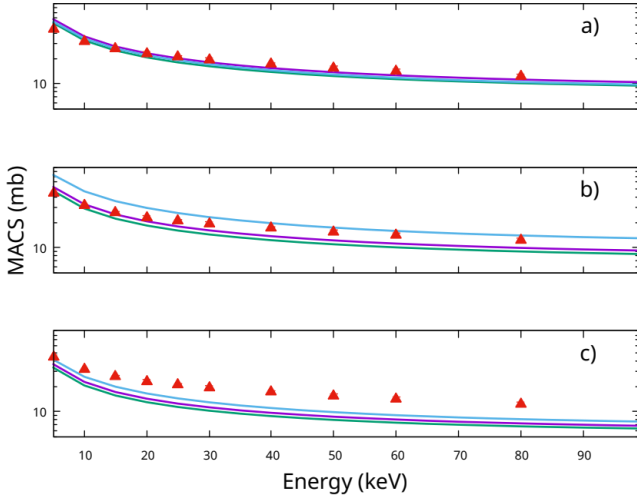
Fig. 1   The calculated MACS using the a) SHFB b) GHFB c) TGHFB level densities for the $^{90}Zr(n,\gamma)^{91}Zr$ process along with the comparison data. The solid lines colored purple, green, and cyan represent the HFBCS, TRMF, and D1M models of photon strengths, respectively. The red triangles represent the experimental data of Tagliente *et al.* [5].

Fig. 2   The calculated MACS using the a) SHFB b) GHFB c) TGHFB level densities for the $^{92}Zr(n,\gamma)^{93}Zr$ process along with the comparison data. The solid lines colored purple, green, and cyan represent the HFBCS, TRMF, and D1M models of photon strengths, respectively. The red triangles represent the experimental data of Tagliente *et al.* [6].
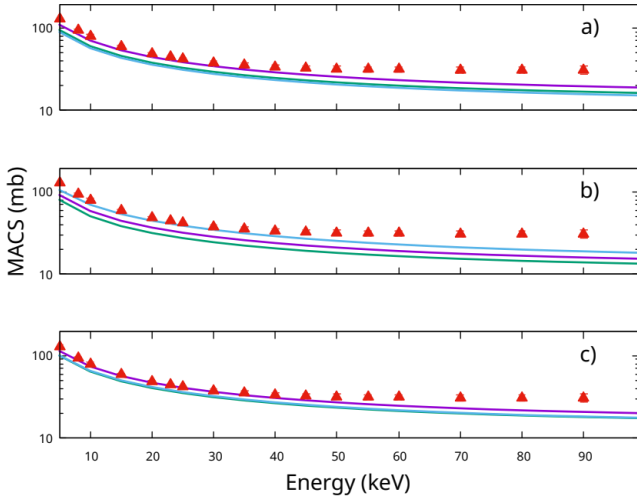
Table 1. The comparison of calculated MACS for the $^{90}Zr(n,\gamma)^{91}Zr$ process with those from KADoNiS at the typical *s*-process energy *kT*=30 keV.

Level Density	Photon Strength	MACS	KADoNiS	Δ
SHFB	HFBCS	17.97	19.3	7.4%
SHFB	TRMF	16.13	19.3	19.7%
SHFB	D1M	16.99	19.3	13.6%
GHFB	HFBCS	16.05	19.3	20.2%
GHFB	TRMF	14.37	19.3	34.3%
GHFB	D1M	23.02	19.3	19.3%
TGHFB	HFBCS	11.26	19.3	71.4%
TGHFB	TRMF	10.27	19.3	87.9%
TGHFB	D1M	12.90	19.3	49.6%

Table 2. The comparison of calculated MACS for the $^{92}Zr(n,\gamma)^{93}Zr$ process with those from KADoNiS at the typical *s*-process energy *kT*=30 keV.

Level Density	Photon Strength	MACS	KADoNiS	Δ
SHFB	HFBCS	34.31	30.1	13.9%
SHFB	TRMF	29.31	30.1	2.7%
SHFB	D1M	27.71	30.1	8.6%
GHFB	HFBCS	28.47	30.1	5.7%
GHFB	TRMF	24.48	30.1	22.9%
GHFB	D1M	34.59	30.1	14.9%
TGHFB	HFBCS	36.49	30.1	21.6%
TGHFB	TRMF	31.49	30.1	4.6%
TGHFB	D1M	32.35	30.1	7.5%

Additionally, we have performed a comparison of our microscopic calculations of MACS with those of Karlsruhe Astrophysical Database of Nucleosynthesis in Stars (KADoNiS) [17]. The analysis based on percentage deviation for $^{90}Zr(n,\gamma)^{91}Zr$ process has been presented in *Table 1*, while that for the $^{92}Zr(n,\gamma)^{93}Zr$ process is in *Table 2*. The results of this comparison are in agreement with the analysis performed with the experimental measurement. For the $^{90}Zr(n,\gamma)^{91}Zr$ process, the SHFB level densities produced the best results, while the TGHFB level densities performed the worst. For the $^{92}Zr(n,\gamma)^{93}Zr$ process, SHFB level densities again produced the best results, followed closely by TGHFB level densities. Interestingly, for this case, all model combinations produced results with percentage differences less than 25%.

Lastly, using the best-fit microscopic model combinations, we have computed the thermonuclear reaction rates up to a temperature of T_9=0.5 as depicted in *Figure 3*. Collections of reaction rates, commonly referred to as libraries, are core nuclear physics inputs to the theoretical studies of the nucleosynthesis environments [18]. The effects of magic neutron numbers on the rates are clearly illustrated. The rates of the $^{92}Zr(n,\gamma)^{93}Zr$ process are higher because the nearly magic neutron numbers offer little resistance to the incoming neutrons in contrast to the $^{90}Zr(n,\gamma)^{91}Zr$ process. The microscopic descriptions suggest a lower reaction rate for $^{92}Zr(n,\gamma)^{93}Zr$ at $T_9 < 0.2$, while for the $^{90}Zr(n,\gamma)^{91}Zr$ process, the rates are found to be systematically lower at all temperatures.

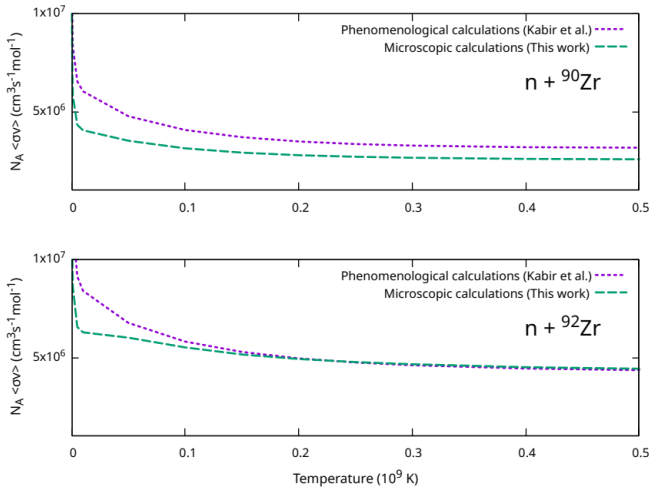Fig. 3   The thermonuclear reaction rates for the ^{90,92}Zr(n,γ)^{91,93}Zr processes using the best fit microscopic and phenomenological model combinations, up to a temperature of T₉=0.5.

Conclusion

In conclusion, we have studied the neutron capture reactions on the isotopes of Zr with mass numbers *A*=90 and *A*=92 using microscopic models for the optical potential, nuclear level density, and photon strength. Our analyses included comparisons with the available experimental data and with KADoNiS. The results obtained using the microscopic nuclear inputs were within the acceptable range, which makes them preferable over the results of adjusted phenomenological models. For ^{90}Zr, the photon strengths combined with the SHFB level densities provided the best agreement. In contrast, for ^{92}Zr, model combinations gave a systematic deviation at higher energies while agreeing at the standard *s*-process energy of *kT*=30 keV. The best-fit reaction rates were found to be lower than the phenomenological ones for both nuclear reactions, suggesting a slower *s*-process flow. The constrained microscopic reaction rates reported in our study can be incorporated in elemental abundance models for improved predictions.

References

[1]   E. M. Burbidge, G. R. Burbidge, W. A. Fowler, and F. Hoyle, "Synthesis of the elements in stars," *Rev. Mod. Phys.*, vol. 29, no. 4, pp. 547, 1957.

[2]   S. Goriely and L. Siess, "The s-process Nucleosynthesis," *Proc. Int. Astron. Union*, vol. 1, no. S228, pp. 451–460, 2005.

[3]   M. Eroğlu, C. Yalçın, and R. T. Güray, "Investigation of the 121Sb (α, γ) 125I reaction cross-section calculations at astrophysical energies," *Nucl. Sci. Tech.*, vol. 34, no. 11, pp. 168, 2023.

[4]   A. Kabir, Z. U. Abideen, J.-U. Nabi, and D. Khan, "Investigation of 90, 92Zr (n, γ) 91, 93Zr in the s-process nucleosynthesis," *Z. Naturforsch. A*, vol. 79, no. 5, pp. 489–496, 2024.

[5]   G. Tagliente *et al.*, "Neutron capture cross section of Zr 90: Bottleneck in the s-process reaction flow," *Phys. Rev. C*, vol. 77, no. 3, pp. 035802, 2008.

[6]   G. Tagliente *et al.*, "The Zr 92 (n, γ) reaction and its implications for stellar nucleosynthesis," *Phys. Rev. C*, vol. 81, no. 5, pp. 055801, 2010.

[7]   N. N. Le, S. Cristallo, D. Vescovi, L. T. Phuc, and N. Q. Hung, "Maxwellian-averaged cross section of 181Ta (n, γ) reaction and its astrophysical implications," *Nucl. Phys. A*, vol. 1023, pp. 122450, 2022.

[8]   S. Goriely, S. Hilaire, and A. J. Koning, "Improved predictions of nuclear reaction rates with the TALYS reaction code for astrophysical applications," *Astron. Astrophys.*, vol. 487, no. 2, pp. 767–774, 2008.

[9]   W. Hauser and H. Feshbach, "The inelastic scattering of neutrons," *Phys. Rev.*, vol. 87, no. 2, pp. 366, 1952.

[10]   A. J. Koning, S. Hilaire, and M. C. Duijvestijn, "TALYS: Comprehensive nuclear reaction modeling," in *AIP Conf. Proc.*, vol. 769, no. 1, pp. 1154–1159, 2005.

[11]   A. Kabir, Z. U. Abideen, and J.-U. Nabi, "Re-investigation of Neutron Capture by 84 Kr and 86 Kr in the s-Process Nucleosynthesis," *Braz. J. Phys.*, vol. 54, no. 3, pp. 80, 2024.

[12]   A. Kabir, M. Tahir, J. Nabi, Z. U. Abideen, and I. Mudassir, "Examination of Radiative capture Rates of 99Tc (n, γ) 100Tc and Stellar β-Decay Rates of 99Tc," *Res. Astron. Astrophys.*, 2025.

[13]   E. Bauge, J. P. Delaroche, and M. Girod, "Semimicroscopic nucleon-nucleus spherical optical model for nuclei with A>~ 40 at energies up to 200 MeV," *Phys. Rev. C*, vol. 58, no. 2, pp. 1118, 1998.

[14]   A. Koning, S. Hilaire, and S. Goriely, "TALYS: modeling of nuclear reactions," *Eur. Phys. J. A*, vol. 59, no. 6, pp. 131, 2023.

[15]   H. Beer, F. Voss, and R. R. Winters, "On the calculation of Maxwellian-averaged capture cross sections," *Astrophys. J. Suppl. Ser.*, vol. 80, no. 1, pp. 403–424, 1992.

[16]   A. Kabir, J.-U. Nabi, M. Tahir, A. Muneem, and Z. U. Abideen, "Re-analysis of temperature dependent neutron capture rates and stellar β-decay rates of 95-98Mo," *Chin. Phys. C*, vol. 48, no. 9, pp. 094101, 2024.

[17]   I. Dillmann *et al.*, "The new KADoNiS v1.0 and its influence on the weak s-process nucleosynthesis," in *PoS (NIC XIII Conf.)*, vol. 57, 2014.

[18]   M. S. Smith, "Nuclear data resources and initiatives for nuclear astrophysics," *Front. Astron. Space Sci.*, vol. 10, pp. 1243615, 2023.

DFT-Based Quantum Chemical Analysis of Coumarin Derivatives

Srinath More[*], Omnath Patil, Shivakumar Chillargikar, Dayanand Lalasangi and S. M. Hanagodimath

Department of PG Studies and Research in Physics, Gulbarga University, Kalaburagi – 585 106, Karnataka, India.

ABSTRACT

The goal of the current work is to use density functional theory (DFT) at the B3LYP level of theory, using a basis set of 6-311++G (d, p), to comprehend the physical and chemical characteristics of 6-Methoxy-4-(4-nitro-phenoxy methyl)-chromen-2-one (6MNPM) and 1-(4-nitro-phenoxy methyl)-benzo[f]-chromen-3-one (4NPMB) of coumarin derivatives. Bond lengths and bond angles, two geometrical parameters, are calculated for coumarin derivatives. We have estimated the frontier molecular orbitals (FMO). Furthermore, to shed light on the stability and chemical reactivity of coumarin derivatives, the global reactivity descriptors were computed using FMO. The molecular electrostatic potential (MEP) investigation aims to identify the coumarin molecules' preferred locations for electrophilic and nucleophilic attacks. The distribution of atomic charge in Mulliken has been performed. The nonlinear optical properties (NLO) of coumarin molecules have been calculated to assess their suitability for NLO applications. The computation of natural bonding orbital (NBO) allows the identification of the most likely intense intermolecular interactions. The analysis focused on the temperature dependency of the thermodynamic characteristics of coumarin derivatives.

Keywords: Frontier molecular orbitals (FMO), Nonlinear optical properties (NLO), Molecular electrostatic potential (MEP), and thermodynamic parameters.

1. Introduction

Coumarin is a versatile scaffold with intriguing biological, pharmacological, biochemical, medicinal, and photochemical properties, offering various applications [1-4]. It belongs to the benzopyrone family and is produced when a benzene ring and an α-pyrone ring fuse together. Since A. Vogel discovered coumarin from tonka beans in 1820, the compound has been identified in seeds, roots, and leaves, particularly among green plants [5]. The coumarin molecule (2H-chromen-2-one) can exhibit a broad spectrum of pharmacological activity because it interacts with numerous important sites in organisms in many ways through multiple mechanisms, including hydrophobic interactions, hydrogen bonding, and electrostatic interactions [6]. Additionally, coumarin derivatives are produced for various uses, such as dye lasers and solar cells with dye sensitization [7]. Furthermore, by replacing the aromatic ring, the versatile function of coumarin allows for adaptable structural changes in the scaffold position (3 and 4) [8]. Phenyl-coumarins are synthetically versatile derivatives that have shown biological and pharmacological effects with an additional phenyl ring connected to any position of the coumarin scaffold. They are regarded as a key class of molecular moiety [9]. Computational techniques can offer useful molecular details for these coumarin derivatives. Consequently, the main goal of this work is to determine the link between the calculated molecular characteristics and the chemical substitutions by examining the structure, electrical, and optical properties of these identical derivatives [10]. We utilized density functional theory (DFT) [11], which is a widely and extensively used quantum mechanical technique, to compute the electronic and structural characteristics of the derivatives [12–14].

The two coumarin derivatives were subjected to a thorough computer analysis [15]. The molecular characteristics of coumarin derivatives have been the subject of several computational DFT investigations for use in optoelectronics [16,17], solar cells [18–21], fluorescent dyes, and lasers [22]. The motivation behind this work is to understand the basic properties of coumarin derivatives with the help of a computational approach, and the results are useful for synthesizing new substitutes of the coumarin molecule, which are useful for optoelectronic devices, sensing applications, and as drug carriers in the medical field. The presented work has not been carried out on the 6MNPM and 4NPMB coumarin derivatives.

2. Materials and methods

2.1. Materials

6-Methoxy-4-(4-nitro-phenoxy methyl)-chromen-2-one (6MNPM) and 1-(4-nitro-phenoxy methyl)-benzo[f]-chromen-3-one (4NPMB) coumarin derivatives were synthesized as per the procedure reported in the literature [23]. The composition of the compounds of the coumarin derivatives is given in Fig. 1 (a) and (b).
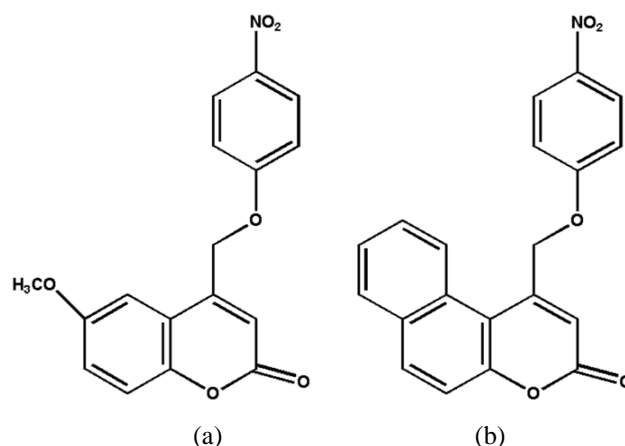

(a)   (b)

Fig. 1 Molecular structures of (a) 6MNPM and (b) 4NPMB molecules

2.2. Quantum Computational details

The DFT approach has been utilized to accomplish the quantum chemical computation of coumarin derivatives at

---

the B3LYP model, with a basis set of 6-311++G (d, p). Gaussian 16 software is used to compute the various properties of the specified derivatives [24]. All computations have been performed to better address the polar bonds of the methoxy and nitro groups. The triple split valence basis set 6-311++G is expanded by including the polarization function (p) and diffuse function (d) for heavy atoms. In the gas phase, the optimization was carried out. The improved geometry has been utilized for the subsequent computations [25-28].

3. Results and Discussion

3.1 Geometrical parameters

The 6MNPM and 4NPMB are substituted phenoxymethyl with two different functional groups: nitro (NO2), methoxy (CH3O), and nitro (NO2), and benzo[f] chromene-3-one (an extra benzene ring to the coumarin). The mentioned functional groups are planar to the benzene ring. Using a basic set of 6-311G++ (d, p), the geometrical parameters, such as the bond length and bond angle of derivatives, were optimized at B3LYP using the DFT approach. As seen in Fig. 2 (a-b), the optimal molecular geometry was calculated at the theoretical level of B3LYP. According to the computed summary of the derivatives' optimal structure, they are members of the C1 point group. The dipole moments of 6MNPM and 4NPMB derivatives in the ground state are 3.44D and 5.15D, respectively. This indicates that the molecule's polarity increases from 6MNPM to 4NPMB molecules. By using the mentioned method, the geometrical characteristics of coumarin derivatives were derived from the optimized molecular structure and are shown in Table 1 (a-b). The parameters, like bond length, bond angle, and dihedral angle, show similar values in both molecules.
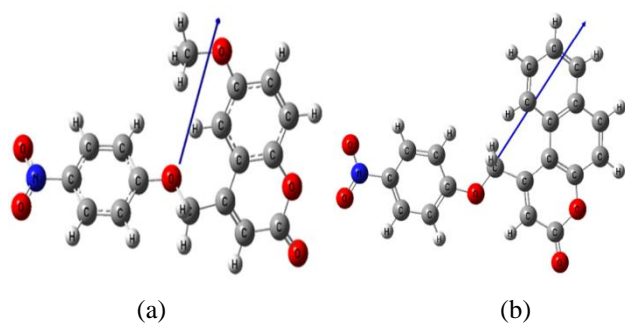

(a)   (b)

Fig. 2 Optimized geometries with dipole moment vector of (a) 6MNPM and (b) 4NPMB molecules.

3.2 Frontier molecular orbital (FMO)

A frontier molecular orbital (FMO) is the intersection of the lowest unoccupied molecular orbital (LUMO) and the highest occupied molecular orbital (HOMO) [29–31]. For coumarin derivatives, the HOMO and LUMO energy plots together with the band gap energy were calculated at B3LYP of DFT using the basis set of 6-311++G (d, p). Figure 3 (a-b) present the electron energy distribution in the HOMO and LUMO for the coumarin derivatives. The observation from Figure 3 (a-b) is, that in the 6MNPM and 4NPMB

derivatives for LUMO, the phenoxy methyl and the functional group of the molecule, NO2 occupies electron density. Whereas in HOMO the localization of electron density is on the methoxy which is attached to the benzene ring but there is a slight change in the distribution of electron density in both derivatives due to the role played by the functional groups attached to the aromatic ring. This indicates the possible intermolecular charge transfer. To examine the chemical reactivity, hardness (η), softness (S), electronegativity (χ), potential (μ), ionization potential (I), electron affinity (E), energy gap (Eg), and electrophilicity index (ω) of derivatives, it is essential to obtain the HOMO-LUMO energy gap value [32, 33]. Using Koopman's formulas, these parameters were determined for the coumarin derivatives in the chemical model, and the obtained values are listed in Table 2. The energy gap in the examined derivatives reduces in the following order: 6MNPM < 4NPMB molecule. This suggests that the energy gap of the 6MNPM molecule is lower. In comparison to the 4NPMB, the 6MNPM molecule has a lower energy value, which suggests that it is more chemically soft, highly reactive, and has weak kinetic stability. Electron affinity (E) and electronegativity (χ) will give information about the electron-accepting ability of a molecule; the higher the values of (E) and (χ), the better the electron-accepting ability. 6MNPM and 4NPMB derivatives have the same value. This means that both derivatives can accept electrons from computational quantum calculations. The electrophilicity index further clarifies the system's capacity for accepting electrons; a higher value of it indicates a higher electron-accepting ability of the molecule. 6MNPM and 4NPMB have very small changes in the value of the electrophilicity index of 0.01 between them, so on this basis, 6MNPM has a higher electron-accepting ability compared to the 4NPMB molecule.

Table 1 (a). Optimized geometrical parameters of 6MNPM molecules.

Structural parameters	B3LYP / 6-311++G (d, p)
Bond length (A^0)	
C1-C5	1.5
C1-O14	1.4
C2-C3	1.3
C3-C4	1.5
C4-C5	1.3
C5-H9	1.0
C7-C11	1.3
C21-O22	1.4
C23-C28	1.3
C24-C25	1.3
C26-N33	1.4
N33-O34	1.1
N33-O35	1.3
Bond angle (θ)	
C5-C1-C14	120.7
O14-C1-O15	119.6
C3-C2-O14	122.3

C2-C3-C4	120.6
C3-C4-C5	118.5
C10-C8-H12	119.9
C8-C10-C11	119.9
O22-C21-H36	109.4
O22-C23-C24	120.0
C24-C23-C28	120.0
C26-N33-O34	120.0
O34-N33-O35	120.0
Dihedral angle (θ)	
O14-C1-C5-C4	010.4
O14-C1-C5-H9	-170.0
O15-C1-C5-H9	009.2
C5-C1-O14-C2	-022.5
O15-C1-O14-C2	158.0
O14-C2-C7-H6	003.9
O14-C2-C7-C11	-175.7
C3-C2-O14-C1	020.7
O22-C23-C24-H30	000.0
C28-C23-C24-H25	000.0
C28-C23-C24-H30	-180.0

Table 1 (b). Optimized geometrical parameters of 4NPMB molecules.

Structural parameter	B3LYP/6-311++G(d, p)
Bond length (A^0)	
C1-C2	1.5
C1-C6	1.3
C1-H18	1.0
C2-C3	1.3
C2-H19	1.0
C3-C4	1.5
C3-H35	1.0
C4-C5	1.3
C4-C7	1.5
C5-C6	1.5
C6-H20	1.0
C7-C8	1.5
C7-C13	1.3
Bond angle (θ)	
C2-C1-C6	119.9
C2-C1-H18	120.0
C6-C1-H18	120.0
C1-C2-C3	119.9
C1-C2-H19	120.0
C3-C2-H19	120.0
C2-C3-C4	120.0
C2-C3-H35	119.9
C4-C3-H35	119.9
C3-C4-C5	119.9
C3-C4-C7	119.9
C5-C4-C7	120.1

Dihedral angle (θ)	
C6-C1-C2-C3	000.0
C6-C1-C2-C19	-179.9
H18-C1-C2-C3	-179.9
H18-C1-C2-H19	000.0
C2-C1-C6-C5	-0.060
C2-C1-C6-H20	179.9
H18-C1-C6-C5	179.9
H18-C1-C6-H20	-0.058
C1-C2-C3-H35	-179.9
C1-C2-C3-H35	-179.9
H19-C2-C3-C4	-179.9

Table 2. Calculated energy values of global reactivity descriptors of 6MNPM and 4NPMB molecules by B3LYP/6-311++G (d, p) method.

| Parameters with Unit	DFT	
	6MNPM	4NPMB
E_{HOMO} (eV)	-0.22815	-0.23039
E_{LUMO} (eV)	-0.08895	-0.08659
Energy gap (E_g) (eV)	0.13920	0.14380
Ionization potential (I) (eV)	0.22815	0.23039
Electron affinity (E) (eV)	0.08895	0.08659
Electronegativity (χ) (eV)	0.15855	0.15849
Chemical potential (μ) (eV)	-0.15855	-0.15849
Chemical hardness (η) (eV)	0.06960	0.07190
Chemical softness (S) (eV^{-1})	14.36781	13.90820
Electrophilicity index (ω) (eV)	0.18053	0.17461

(a) (b)
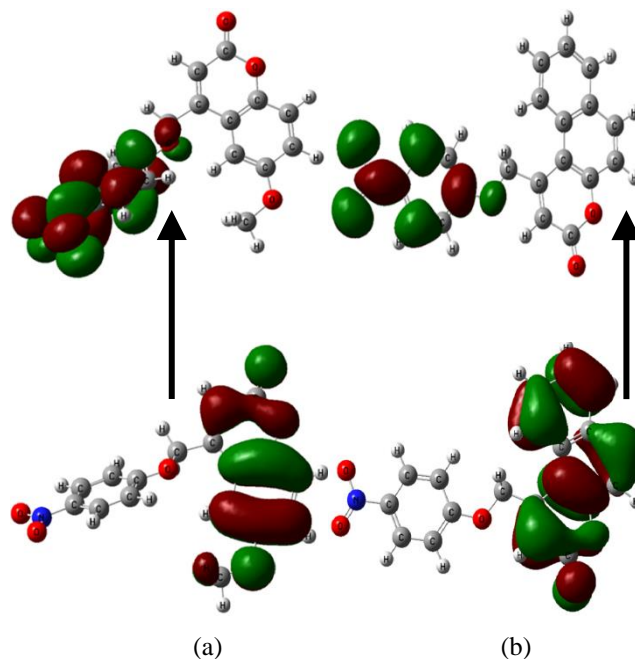
Fig 3. HOMO and LUMO of (a) 6MNPM and (b) 4NPMB molecules.

3.3 Molecular Electrostatic Potential (MEP)

The molecular electrostatic potential(MEP) is utilized to show the hydrogen bonding interactions and it describes a molecule's nucleophilic and electrophilic sites qualitatively

[32, 34]. The physio-chemical characteristics are also analyzed using MEP. The MEP color coding goes as follows: red denotes an electron-rich site, which is the spot where an electrophilic attack is more likely to occur. Yellow denotes a little electron deficiency, green denotes neutrality, light blue denotes a slight electron deficiency, and blue denotes an electron deficiency, the ideal location for a nucleophilic attack. These maps provide us with the ability to see a molecule's variable charge areas. The present study obtains the 3-dimensional plot of MEP of coumarin derivatives using the DFT model. The MEP maps obtained from chemical mode have certain similarities. Fig. 4 (a-b) shows the MEP-mapped surface estimated for coumarin derivatives at the B3LYP level of theory. This sort of circumstance has been observed in various compounds. It is referred to as electrophilic attack because it demonstrates that negative potential is dispersed around the oxygen atom that is linked to the carbon [35], with potential elevations in the following order: red, orange, green, and blue. In the 6MNPM molecule, the color coding of these maps falls between -0.0544 a.u. (deepest red) and 0.0544 a.u. (deepest blue). The nitrogen N and hydrogen H atoms connected to the benzene ring are surrounded by a positive potential, making this an attractive target for nucleophilic attack. When contrasted, the N atoms' positive potential value is 0.011 a.u, and the H atoms also have a positive potential value of identical magnitude. However, the H atom has a larger positive potential than the N atom. Concerning the H atoms in the CH_3 group, the maximal positive areas have a value of 0.031 a.u. In contrast, the 6MNPM molecule's H atoms in the ring have smaller values than those at the CH_3. As a result, the electrostatic potential distribution of 4NPMB and its surrounding molecule is somewhat altered when a benzene ring is added in place of a methyl group in the provided molecule. Coumarin derivatives exhibit chemical activity due to the presence of both nucleophilic and electrophilic attack sites.
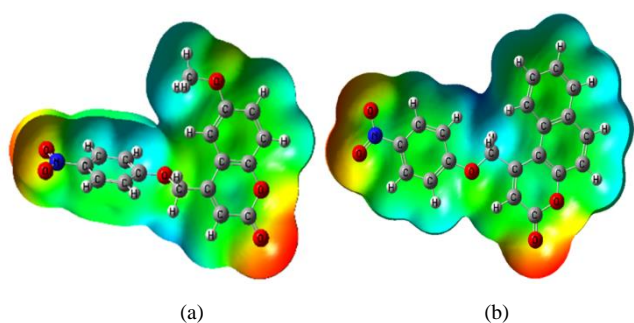

Fig. 4 Electrostatic Density Surface of (a) 6MNPM and (b) 4NPMB molecules.

3.4 Mulliken Atomic Charges

Using a quantum chemistry approach, the Mullikan atomic charge analysis may be performed to characterize the impacts of atomic charge, dipole moment, electronic structure and molecule polarizability of the system [36, 35]. The Mulliken atomic charge distribution of the derivatives is computed at the B3LYP level of theory using the DFT chemical model, employing the basis set of 6-311++G (d, p) for the coumarin molecules. Figures 5 (a, b) show the distribution of atomic charges in Mulliken for coumarin molecules. The distribution of charge between the 6MNPM and 4NPMB derivatives is found to differ noticeably. In the molecule of 6MNPM, the C_1 atom has a charge of 0.5922C and it is surrounded by the carbon and hydrogen atoms and attached by oxygen atoms. The 4NPMB molecule also consists of a C_1 atom with a charge of -0.0864 C. It is in the aromatic ring and connected by the H atom. So here clearly, we can see the difference in the charge occupied by the C_1 atom. This could be due to the conjugation interaction between the C1 and its surrounding atoms.
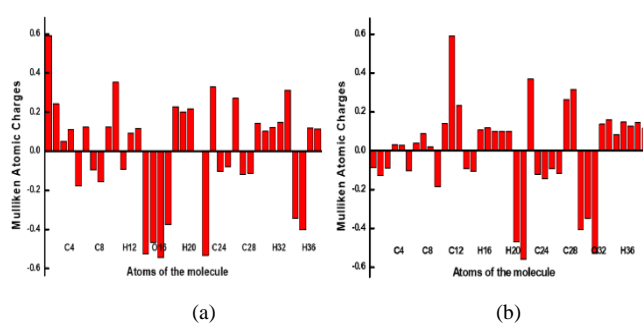
Fig 5. Mulliken Atomic Charge Distribution of (a) 6MNPM and (b) 4NPMB molecules.

3.5 Natural Bond Orbital Analysis (NBO)

Natural bond orbital analysis (NBO) was used to interpret interaction atomic orbitals on title molecules, revealing atomic charges, orbital occupancies, hybrid contributions, and electron density delocalization. The NAO orbital energies are calculated by using the Kohu-sham operator (F) as

$$\varepsilon_i^{(A)} = \langle \theta_i^{(A)} / F / \theta_i^{(A)*} \rangle$$

Table 3 (a-b) depict many bonding principles, such as the kind of bond orbital, occupancies, natural atomic hybrids that comprise the NBO, and the proportion of each hybrid in the NBO. Furthermore, the hybrid label and atom label show the quantity of s-character, p-character and additional hybrid orbital (sp_x) composition of coumarin molecules, as estimated by the B3LYP/6-311++G (d, p) basis set using DFT as a chemical model [37–41]. Table 4 (ab) summarizes the stabilizing energy of several types of interaction. As shown below, the stabilization energy E (2) is connected to the delocalization of i (donor) → j (acceptor) [42, 43].

$$E^{(2)} = -q_i \frac{F^2(i,J)}{\varepsilon_j - \varepsilon_i}$$

Table 3(a). Natural bond orbital analysis of 6MNPM molecule by DFT/B3LYP with the basic set 6-311++G (d, p).

Bond orbital	Occupancy	Atom	Contribution from parent NBO (%)	Atomic hybrid contribution (%)
σC1-C2	1.97984	C1	49.94	S(30.92)+P(69.04)+D(0.04)
		C2	50.06	S(30.83)+P(69.13)+D(0.04)
πC1-C6	1.82588	C1	50.09	S(00.00)+P(99.94)+D(0.06)
		C6	49.91	S(00.00)+P(99.94)+D(0.06)
πC2-C3	1.83272	C2	48.25	S(00.00)+P(99.94)+D(0.06)
		C3	51.75	S(00.00)+P(99.96)+D(0.04)
πC4-C5	1.70412	C4	50.06	S(00.00)+P(99.95)+D(0.05)
		C5	49.94	S(00.00)+P(99.95)+D(0.05)
πC7-C13	1.76916	C7	52.80	S(00.00)+P(99.95)+D(0.05)
		C13	47.20	S(00.01)+P(99.92)+D(0.07)
πC8-C10	1.84714	C8	48.06	S(00.07)+P(99.86)+D(0.07)
		C10	51.94	S(00.06)+P(99.87)+D(0.07)
πC12-O21	1.98014	C12	32.29	S(00.26)+P(99.58)+D(0.16)
		O21	67.71	S(00.15)+P(99.56)+D(0.29)
πC14-C15	1.83286	C14	51.05	S(00.00)+P(99.94)+D(0.06)
		C15	48.95	S(00.00)+P(99.94)+D(0.06)
πC23-C25	1.77184	C23	47.43	S(00.01)+P(99.92)+D(0.07)
		C25	52.57	S(00.00)+P(99.94)+D(0.06)
σ*C1-C2	0.02155	C1	50.06	S(30.92)+P(69.04)+D(0.04)
		C2	49.94	S(30.83)+P(69.13)+D(0.04)
π*C1-C6	0.15664	C1	49.91	S(00.00)+P(99.94)+D(0.06)
		C6	50.09	S(00.00)+P(99.94)+D(0.06)
π*C2-C3	0.17183	C2	51.75	S(00.00)+P(99.94)+D(0.06)
		C3	48.25	S(00.00)+P(99.96)+D(0.04)
π*C4-C5	0.30175	C4	49.94	S(00.00)+P(99.95)+D(0.05)
		C5	50.06	S(00.00)+P(99.95)+D(0.05)
π*C7-C13	0.27597	C7	47.20	S(00.00)+P(99.95)+D(0.05)
		C13	52.80	S(00.01)+P(99.92)+D(0.07)
π*C8-C10	0.12327	C8	51.94	S(00.07)+P(99.86)+D(0.07)
		C10	48.06	S(00.06)+P(99.87)+D(0.07)
π*C12-O21	0.24436	C12	67.71	S(00.06)+P(99.58)+D(0.16)
		O21	32.29	S(00.15)+P(99.56)+D(0.29)
π*C14-C15	0.15948	C14	48.95	S(00.00)+P(99.94)+D(0.06)
		C15	51.05	S(00.00)+P(99.94)+D(0.06)
π*C23-C25	0.23609	C23	52.57	S(00.01)+P(99.92)+D(0.07)
		C25	47.43	S(00.00)+P(99.94)+D(0.06)

Table 3(b). Natural bond orbital analysis of 4NPMB molecule by DFT/B3LYP with the basic set 6-311++G (d, p).

Bond orbital	Occupancy	Atom	Contribution from parent NBO (%)	Atomic hybrid contribution (%)
σC1-C2	1.97984	C1	49.94	S(30.92)+P(69.04)+D(0.04)
		C2	50.06	S(30.83)+P(69.13)+D(0.04)
πC1-C6	1.82588	C1	50.09	S(00.00)+P(99.94)+D(0.06)
		C6	49.91	S(00.00)+P(99.94)+D(0.06)
πC2-C3	1.83272	C2	48.25	S(00.00)+P(99.94)+D(0.06)
		C3	51.75	S(00.00)+P(99.96)+D(0.04)
πC4-C5	1.70412	C4	50.06	S(00.00)+P(99.95)+D(0.05)
		C5	49.94	S(00.00)+P(99.95)+D(0.05)
πC7-C13	1.76916	C7	52.80	S(00.00)+P(99.95)+D(0.05)
		C13	47.20	S(00.01)+P(99.92)+D(0.07)
πC8-C10	1.84714	C8	48.06	S(00.07)+P(99.86)+D(0.07)

		C10	51.94	S(00.06)+P(99.87)+D(0.07)
πC12-O21	1.98014	C12	32.29	S(00.26)+P(99.58)+D(0.16)
		O21	67.71	S(00.15)+P(99.56)+D(0.29)
πC14-C15	1.83286	C14	51.05	S(00.00)+P(99.94)+D(0.06)
		C15	48.95	S(00.00)+P(99.94)+D(0.06)
πC23-C25	1.77184	C23	47.43	S(00.01)+P(99.92)+D(0.07)
		C25	52.57	S(00.00)+P(99.94)+D(0.06)
σ*C1-C2	0.02155	C1	50.06	S(30.92)+P(69.04)+D(0.04)
		C2	49.94	S(30.83)+P(69.13)+D(0.04)
π*C1-C6	0.15664	C1	49.91	S(00.00)+P(99.94)+D(0.06)
		C6	50.09	S(00.00)+P(99.94)+D(0.06)
π*C2-C3	0.17183	C2	51.75	S(00.00)+P(99.94)+D(0.06)
		C3	48.25	S(00.00)+P(99.96)+D(0.04)
π*C4-C5	0.30175	C4	49.94	S(00.00)+P(99.95)+D(0.05)
		C5	50.06	S(00.00)+P(99.95)+D(0.05)
π*C7-C13	0.27597	C7	47.20	S(00.00)+P(99.95)+D(0.05)
		C13	52.80	S(00.01)+P(99.92)+D(0.07)
π*C8-C10	0.12327	C8	51.94	S(00.07)+P(99.86)+D(0.07)
		C10	48.06	S(00.06)+P(99.87)+D(0.07)
π*C12-O21	0.24436	C12	67.71	S(00.06)+P(99.58)+D(0.16)
		O21	32.29	S(00.15)+P(99.56)+D(0.29)
π*C14-C15	0.15948	C14	48.95	S(00.00)+P(99.94)+D(0.06)
		C15	51.05	S(00.00)+P(99.94)+D(0.06)
π*C23-C25	0.23609	C23	52.57	S(00.01)+P(99.92)+D(0.07)
		C25	47.43	S(00.00)+P(99.94)+D(0.06)

Where q_i is the donor orbital occupancy, ε_i, and ε_j are diagonal elements (orbital energies), and F^2 (i, j) is the off-diagonal Fock matrix element. The data presented in Table 4 (a-b) for the derivatives 6MNPM and 4NPMB show that the correspondence between the bonding donor (C_{26}-C_{27}) and anti-bonding acceptor (C_{24}-C_{25}) has a maximum stabilizing energy value of 20.25 Kcal mol^{-1} for the 6MNPM molecule.

Table 4(a). Second-order perturbation theory analysis of Fock matrix in NBO basic for 6MNPM molecule with the basic set 6-311++G (d, p).

Donor(i)	Type of bond	Acceptor(j)	Type of bond	E^2 (*kJ*/mol)[a]	E(j) - E(i) (a.u)[b]	F(i.j) (a.u)[c]
C1-C5	σ	C4-C5	σ*	01.91	1.29	0.044
C1-O14	σ	C2-C7	σ*	02.51	1.21	0.049
C1-O15	π	C1-O15	π*	00.61	0.35	0.014
	π	C4-C5	π*	04.91	0.39	0.040
C2-C3	π	C4-C5	π*	10.58	0.32	0.053
		C7-C11	π*	10.04	0.31	0.049
C4-C5	π	C1-O15	π*	16.56	0.28	0.062
		C2-C3	π*	09.14	0.31	0.050
C7-C11	π	C2-C3	π*	10.24	0.30	0.051
		C8-C10	π*	10.65	0.31	0.052
C8-C10	π	C7-C11	π*	10.26	0.31	0.050
C24-C25	π	C23-C28	π*	12.02	0.30	0.054
C26-C27	π	C24-C25	π*	20.45	0.18	0.060
N33-O35	π	C26-C27	π*	01.14	1.48	0.037

Table 4(b). Second order perturbation theory analysis of Fock matrix in NBO basic for 4NPMB molecule with the basic set 6-311++G (d, p).

Donor(i)	Type of bond	Acceptor(j)	Type of bond	E^2 (*kJ*/mol)[a]	E(j) - E(i) (a.u)[b]	F(i.j) (a.u)[c]
C1-C6	π	C2-C3	π*	11.16	0.30	0.052
C2-C3	π	C1-C6	π*	09.89	0.31	0.050
C2-H19	σ	C3-C4	σ*	05.51	0.94	0.064

C4-C5	π	C14-C15	π^*	10.01	0.30	0.051
		C7-C13	π^*	11.04	0.29	0.051
C7-C13	π	C4-C5	π^*	10.32	0.33	0.053
		C14-C15	π^*	09.15	0.32	0.049
C8-C9	π	C7-C13	π^*	09.32	0.31	0.050
C12-O21	π	C12-O21	π^*	00.63	0.35	0.014
		C8-C10	π^*	04.85	0.39	0.040
C14-C15	π	C4-C5	π^*	09.63	0.32	0.051
		C7-C13	π^*	10.88	0.30	0.052
C23-C25	π	C27-C28	π^*	13.18	0.30	0.057
C27-C28	π	N29-O31	π^*	20.80	0.18	0.060
N29-O31	π	C27-C28	π^*	03.64	0.48	0.040

The 4NPMB molecule has the highest stabilization energy value of 20.80 Kcal mol^{-1} between the bonding donor of (C$_{27}$-C$_{28}$) and the anti-bonding acceptor of (N$_{29}$-O$_{31}$). The interactions mentioned above represent the most significant interactions of coumarin derivatives among all interactions.

3.6 Polarizability and hyperpolarizability (NLO)

The polarizability tensor components' value depends on the chosen Cartesian coordinate system. Isotropic derivatives have the same polarizability in all directions, while anisotropic derivatives have different directions. Raman scattering intensity is proportional to derived polarizability components, which are constant regardless of the molecules' orientation. The quantities ($\bar{\alpha}$) and (γ) measure the scattering intensity and anisotropy invariant, respectively. Using the DFT chemical model with a basis set of B3LYP/6-311++G (d, p) numerical derivative of the dipole moment, the polarizability invariant is calculated. Table 5 displays the relevant parameter values. There are atomic units in the calculated values. Accordingly, the computed values are transformed into electrostatic units (for β, 1 a.u. = 8.6393 x 10^{-33} esu, and for α, 1 a.u. = 0.1482 x 10^{-24} esu). Definitions [43] about isotropic polarizability state that

$$\bar{\alpha} = 1/3(\alpha_{xx} + \alpha_{yy} + \alpha_{zz})$$

The polarizability anisotropy invariant is

$$\gamma^2 = 1/2\left[(\alpha_{xx} - \alpha_{yy})^2 + (\alpha_{yy} - \alpha_{zz})^2 + (\alpha_{zz} - \alpha_{xx})^2 + 6(\alpha_{xy}^2 + \alpha_{yz}^2 + \alpha_{zx}^2)\right]$$

and the average hyperpolarizability is

$$\beta_{total} = \sqrt{(\beta_x^2 + \beta_y^2 + \beta_z^2)}$$

or

$$\beta_{total} = \sqrt{(\beta_{xxx} + \beta_{xyy} + \beta_{xzz})^2 + (\beta_{yyy} + \beta_{yxx} + \beta_{yzz})^2 + (\beta_{zzz} + \beta_{zxx} + \beta_{zyy})^2}$$

where α_{xx}, α_{yy} and α_{zz} are elements of the polarizability tensor. β_x, β_y and β_z are hyperpolarizability's tensor components. The study of NLO of coumarin derivatives will provide useful information that could be used to understand important properties like optoelectronic applications. Table 5 provides the parameters of 6MNPM and 4NPMB molecules.

Table 5. Total electric dipole moment ($\bar{\mu}$), the mean polarizability($\bar{\alpha}$), the anisotropy polarizability ($\bar{\gamma}$), and mean first-order hyperpolarizability with the basic set 6-311++G (d, p).

Parameters	DFT	
	6MNPM	4NPMB
Electric dipole moment ($\bar{\mu}$)		
μ_x	0.93	2.93
μ_y	3.31	4.20
μ_z	0.04	-0.43
$\bar{\mu}$ (Debye)	3.44	5.15
Polarizability(α)		
α_{xx}	-186.58	-186.80
α_{yy}	-132.66	-156.00
α_{zz}	-140.89	-145.59
α_{xy}	027.78	033.18
α_{xz}	000.98	004.71
α_{yz}	-004.95	-001.17
$\bar{\alpha}$	-153.38	-162.80
$\bar{\gamma}$	379.98	403.56
$\bar{\alpha}$ esu (x 10^{-24})	-022.73	-024.12
$\bar{\gamma}$ esu (x 10^{-24})	056.31	059.80
Hyperpolarizability(β)		
β_{xxx}	324.19	380.23
β_{yyy}	110.48	119.40
β_{zzz}	-002.23	000.60
β_{xyy}	-084.13	-061.98
β_{xxy}	048.18	027.77
β_{xxz}	-033.90	-052.49
β_{xzz}	-017.99	-028.20
β_{yzz}	-013.05	-022.92
β_{yyz}	006.25	-009.28
β_{xyz}	-009.41	-007.53
β_x	222.07	290.04
β_y	145.61	124.25
β_z	-029.88	-061.17
β_{total}	267.23	321.41
β_{total} esu (x 10^{-33})	2308.70	2776.78

It included the values of electric dipole moment, polarizability and hyperpolarizability of coumarin molecules. The 4NPMB molecule has a slightly larger value of parameters mentioned above as compared to the 6MNPM molecule.

3.7 Thermodynamic Properties

Using DFT as a chemical model and the B3LYP/6-311++G (d, p) basis set, the values for various thermodynamic parameters, such as heat capacity, entropy, and enthalpy changes of the title molecule in the gas phase at different temperatures are computed to explain, how the thermodynamic parameters change while changing the chemical models. These thermodynamic parameters are rising with temperatures between 100 and 1000K, as shown in Table 6, because molecule vibrational intensities are increasing with temperature [43]. Figure 6 shows how entropy (S), enthalpy change ($\Delta H_o \rightarrow T$), and heat capacity at constant pressure (Cp) relate to temperature. It reveals that the thermal energy and entropy of the 6MNPM molecule are the same at the temperature of 400K, while 4NPMB molecule requires 470 K to achieve the same state. This difference in temperature is likely due to the distinct molecular structures of the two coumarin molecules.

Table 6. Thermodynamic properties of 6MNPM and 4NPMB molecules at different temperatures by B3LYP/6-311++G (d, p).

| Temperature (k)	C_v (calmol^{-1}K^{-1})		S (calmol^{-1}K^{-1})		ΔH_o (calJmol^{-1})	
	6MNPM	4NPMB	6MNPM	4NPMB	6MNPM	4NPMB
100	34.10	32.50	100.59	99.62	163.81	173.83
200	56.26	56.09	132.37	130.61	168.32	178.23
273	73.06	74.55	152.96	151.39	173.04	183.00
298	78.85	80.89	159.83	158.41	174.95	184.96
300	79.28	81.35	160.33	158.93	175.09	185.11
400	101.00	105.02	186.75	186.22	184.13	194.45
500	119.47	125.04	211.78	212.32	195.18	205.99
600	134.53	141.31	235.30	236.97	207.91	219.33
700	146.71	154.43	257.30	260.08	222.00	234.14
800	156.60	165.05	277.82	281.69	237.18	250.14
900	164.68	173.70	296.98	301.88	253.26	267.09
1000	171.34	180.81	314.90	320.77	270.07	284.83

(a)

(b)
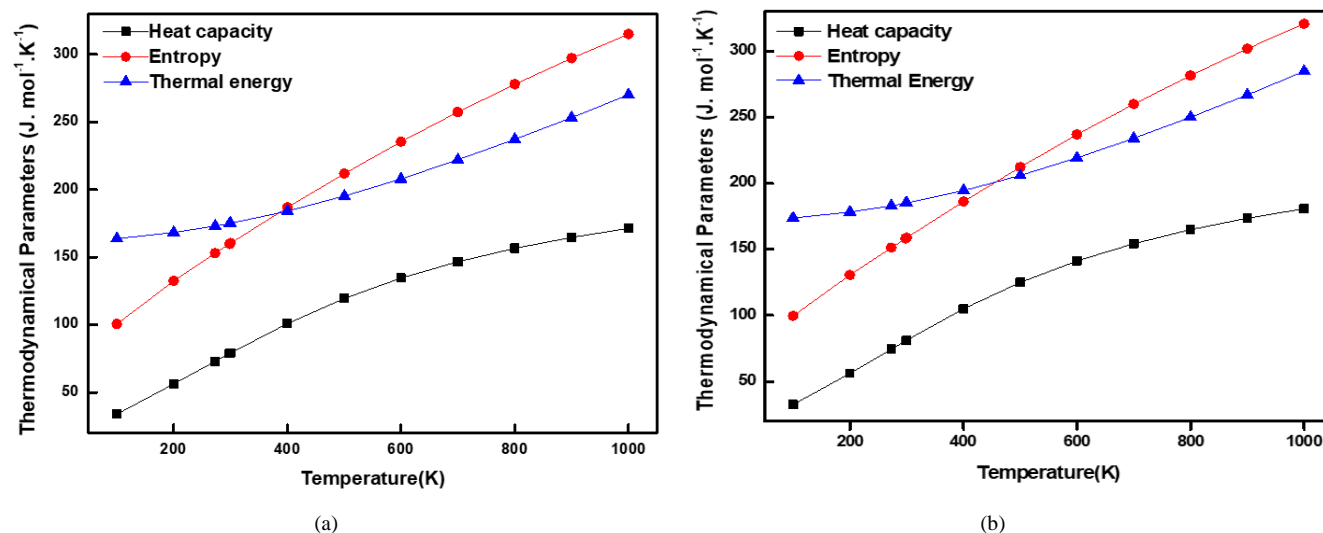
Fig 6. Correlation Graph of (a) 6MNPM and (b) 4NPMB molecules.

4. Conclusion

In the current work, the thermal properties of both derivatives were analysed together with the geometrical characteristics of the optimal structure of coumarin molecules. The MEP map demonstrates that the positive potential sites are located around the N and H atoms connected to the benzene ring, while the negative potential sites are located around the O atom related to the C. Analysis of natural bond orbitals reveals the strong intramolecular interactions. The HOMO and LUMO reveal the molecule's chemical activity. Utilizing the orbital energies, molecular traits like electronegativity, chemical potential, hardness, softness, and electrophilicity index were calculated. The reduction of the HOMO-LUMO energy band gap supports the molecule's bioactive properties. The Mulliken charges and first-order hyperpolarizability are determined. Since

molecular vibration intensities increase with temperature, thermodynamic characteristics show that heat capacities, entropies and enthalpies essentially rise with temperature. We intend that all the computed and analysed data above will be helpful to future researchers.

Author Contributions: Each author contributed to the idea and planning of the study. Srinath, Omnath Patil, Shivakumar Chillargikar, Dayanand Lalasangi and S. M. Hanagodimath prepared the materials, collected the data, and conducted the analysis. All contributors provided feedback on earlier iterations of the article, with Srinath writing the original draft. The final manuscript was reviewed and approved by each author.

Data Availability: During the current investigation, no datasets were created; only the occurred data.

Declarations

Competing Interests: None of the authors has any conflicting interests.

References

[1] M. A. Musa, J. S. Cooperwood, and M. O. Khan, "A review of coumarin derivatives in pharmacotherapy of breast cancer," Curr. Med. Chem., vol. 15, pp. 2664–2679, 2008.

[2] F. Borges, F. Roleira, N. Milhazes, L. Santana, and E. Uriarte, "Simple coumarins and analogues in medicinal chemistry: Occurrence, synthesis and biological activity," Curr. Med. Chem., vol. 12, pp. 887–916, 2005.

[3] G. R. Geen, J. M. Evens, A. K. Vong, A. R. Katritzky, C. W. Rees, and E. F. V. Scriven, "Pyrans and their benzo derivatives: Applications," in Comprehensive Heterocyclic Chemistry II, R. Lan, C. W. R. Katritzky, and E. F. V. Scriven, Eds. Oxford, U.K.: Pergamon Press, 1997, pp. 469–500.

[4] D. Egan, R. O'Kennedy, E. Moren, D. Cox, E. Prosser, and R. D. Thornes, "The pharmacology, metabolism analysis and applications of coumarin and coumarin-related compounds," Drug Metab. Rev., vol. 22, pp. 503–529, 1990.

[5] M. Curini, G. Cravotto, F. Epifano, and G. Giannone, "Chemistry and biological activity of natural and synthetic phenyloxy coumarins," Curr. Med. Chem., vol. 13, pp. 199–222, 2006.

[6] P. Anand, B. Singh, and N. Singh, "A review on coumarins as acetylcholinesterase inhibitors for Alzheimer's disease," Bioorg. Med. Chem., vol. 20, pp. 1175–1180, 2012.

[7] X. Liu, J. M. Cole, P. G. Waddell, T. C. Lin, J. Radia, and A. Zeidler, "Molecular origins of optoelectronic properties in coumarin dyes: Toward designer solar cell and laser application," J. Phys. Chem. A, vol. 116, pp. 727–737, 2011.

[8] K. P. Barot, S. V. Jain, L. Kremer, S. Singh, and M. D. Ghate, "Recent advances and therapeutic journey of coumarins: Current status and perspectives," Med. Chem. Res., vol. 24, pp. 2771–2798, 2015.

[9] G. L. Delogu and M. J. Matos, "Coumarins as promising scaffold for the treatment of age-related diseases—An overview of the last five years," Curr. Top. Med. Chem., vol. 17, pp. 3173–3189, 2017.

[10] A. G. Pramod, C. G. Renuka, and Y. F. Nadaf, "Electronic structure, optical properties and quantum chemical investigation on synthesized coumarin derivative in liquid media for optoelectronic devices," J. Fluorescence, vol. 29, pp. 953–968, 2019.

[11] W. Kohn, "Nobel Lecture: Electronic structure of matter—Wave functions and density functionals," Rev. Mod. Phys., vol. 71, pp. 1253–1266, 1999.

[12] I. Azad, Y. Akhter, T. Khan, M. I. Azad, S. Chandra, P. Singh, D. Kumar, and M. Nasibullah, "Synthesis, quantum chemical study, AIM simulation, in silico ADMET profile analysis, molecular docking and antioxidant activity assessment of aminofuran derivatives," J. Mol. Struct., vol. 127, pp. 285, 2019.

[13] E. Molteni, G. Cappellini, G. Onida, and G. Mula, "Extensive stacking of DHI-like monomers as a model of out-of-plane complexity in eumelanin protomolecules: Chemical and structural sensitivity of optical absorption spectra," Chem. Phys., vol. 524, pp. 92–100, 2019.

[14] D. Zhao, Q. Lu, R. Su, Y. Li, and M. Zhao, "Light harvesting and optical-electronic properties of two quercetin and rutin natural dyes," Appl. Sci., vol. 9, no. 2567, 2019.

[15] M. A. L. Marques and E. K. U. Gross, "Time-dependent functional theory," Annu. Rev. Phys. Chem., vol. 55, pp. 427–455, 2004.

[16] K. V. Basavarajappa, Y. Arthoba Nayaka, H. T. Purushothama, M. M. Vinaya, A. Antony, and P. Poornesh, "Optoelectronic and current-voltage studies for novel coumarin dyes," Int. J. Environ. Anal. Chem., pp. 1–14, 2019.

[17] K. Hara, T. Sato, R. Katoh, A. Furube, Y. Ohga, A. Shinpo, S. Suga, K. Sayama, H. Sugihara, and H. Arakawa, "Molecular design of coumarin dyes for efficient dye-sensitized solar cells," J. Phys. Chem. B, vol. 107, pp. 597–606, 2003.

[18] C. I. Oprea, P. Panait, F. Cimpoesu, M. Ferbinteanu, and M. A. Girtu, "Density functional theory (DFT) study of coumarin-based dyes absorbed on TiO2 nanoclusters—Applications to dye-sensitized solar cells," Materials, vol. 6, pp. 2372–2392, 2013.

[19] K. Hara, Z. S. Wang, T. Sato, A. Furube, R. Katoh, H. Sugihara, Y. Danoh, C. Kasad, A. Shinpo, and S. Suga, "Oligothiophene-containing coumarin dyes for efficient dye-sensitized solar cells," J. Phys. Chem. B, vol. 109, pp. 15476–15482, 2005.

[20] R. Sanchez-de-Armas, M. A. San Miguel, J. Oviedo, and J. F. Sanz, "Coumarin derivatives for dye-sensitized solar cells: A TD-DFT study," Phys. Chem., vol. 14, pp. 225–233, 2012.

[21] F. Mutlak, A. Mohi, and T. Alwan, "Density functional theory study of molecular structure, electronic properties, UV-Vis spectra on coumarin 102," Baghdad Sci. J., vol. 13, pp. 143–152, 2016.

[22] Srinath, D.Lalasangi, V.Mallayya*, S. M. Hanagodimath "Fluorescence Quenching Analysis of 6MNPM Molecule by Steady State Method". g analysis of 6MNPM molecule Mapana – Journal of Sciences 2025, Vol. 24, No. 1, 43-52 ISSN 0975-3303.

[23] M. Basanagouda, M. V. Kulkarni, D. Sharma, V. K. Gupta, P. Pranesha, P. Sandhyarani, and V. P. Rasal, "Synthesis and biological evaluation of some novel 1,2,4-triazole derivatives," J. Chem. Sci., vol. 121, pp. 485–495, 2009.

[24] A. Kumar, G. Cappellini, and F. Delogu, "Electronic and optical properties of chromophores from hexaneuronic acids," Cellulose, vol. 26, pp. 1489–1501, 2019

[25] N. Chowdareddy, A. R. Lamani, A. G. Pramod, and V. B. Tangod, "Nonlinear refractive index enhancement of Nd^{3+} ions loaded borate glasses in the near-infrared region by silver nanoparticles," Opt. Mater., vol. 142, p. 114067, 2023.

[26] V. B. Tangod, B. M. Mastiholi, P. Raikar, S. G. Kulkarni, and U. S. Raikar, "Studies of the photophysics of highly fluorescent Red Mega 480 laser dye in solutions: Steady state spectroscopy," Spectrochim. Acta A Mol. Biomol. Spectrosc., vol. 148, pp. 105–113, 2015.

[27] M. S. Jadhav, L. S. Laxmeshwar, J. F. Akki, P. U. Raikar, V. B. Tangod, and U. S. Raikar, "Multimode fiber optic sensor for adulterant traces in edible oil using nanotechnology technique," Mater. Today Proc., vol. 4, no. 11, pp. 11910–11914, 2017.

[28] S. Patil, O. Devar, and S. Srinath, "Estimation of electric dipole moment by solvatochromism, computational method, and study of the effect of solvents by preferential solvation of 6-methoxy-4-(4-nitrophenoxy methyl)-chromen-2-one (6MNPM)," J. Fluoresc., 2024.

[29] X. Liu, J. M. Cole, and K. S. Low, "Solvent effects on the UV-Vis absorption and emission of optoelectronic coumarins: A comparison of three empirical solvatochromic models," J. Phys. Chem. C, vol. 117, pp. 14731–14741, 2013.

[30] A. G. Pramod, C. G. Renuka, Y. F. Nadaf, and R. Rajaramakrishna, "Impact of solvents on energy gap, photophysical, photometric properties for a new class of 4-HCM coumarin derivative: Nonlinear optical studies and optoelectronics applications," J. Mol. Liq., vol. 292, pp. 111–393, 2019.

[31] M. Cossi, J. M. Millam, M. Klene, C. Adamo, R. Cammi, J. W. Martin, D. J. Fox, Gaussian 09, Revision D.01, Gaussian Inc., Wallingford, CT, 2009.

[32] M. A. Mumit, T. K. Pal, M. A. Alam, M. A. Islam, S. Paul, M. C. Sheikh, "DFT studies on vibrational and electronic spectra, HOMO-LUMO, MEP, HOMO, NBO and molecular docking analysis of benzyl-3-N-(2,4,5-trimethoxyphenylmethylene) hydrazinecarbodithioate," J. Mol. Struct., vol. 1220, p. 128715, 2020.

[33] V. Q. Vuong, Y. Nishimoto, D. G. Fedorov, B. G. Sumpter, T. A. Niehaus, and S. Irle, "The fragment molecular orbital method based on long-range corrected," J. Chem. Theory Comput., vol. 15, no. 5, pp. 3008–3020, 2019.

[34] V. K. Choudhary, K. Bhatt, D. Dash, and N. Sharma, "DFT calculation on molecular structure, HOMO-LUMO study, reactivity descriptors and spectral analysis of newly synthesized diorganotin (IV) 2-chloridophenylacetohydroxamate complexes," J. Comput. Chem., vol. 40, no. 27, pp. 2354–2363, 2019.

[35] S. Muthu and E. I. Paulraj, "Molecular structure, vibrational spectra, first order hyperpolarizability, NBO and HOMO-LUMO analysis of 4-amino-3(4-chlorophenyl)butanoic acid," Solid State Sci., vol. 14, no. 4, pp. 476–487, 2012.

[36] J. Frau, F. Muñoz, and D. Glossman-Mitnik, "Validation of Koopman's theorem in DFT through the calculation of the conceptual DFT descriptors of three fluorescent DNA staining dyes," Chem. Informatics, vol. 2, no. 2, 2016.

[37] A. U. Rani, N. Sundaraganesen, M. Kurt, M. Cinar, and M. Karabacak, "FT-IR, FT-Raman, NMR spectra and DFT calculation on 4-chloro-N-methylaniline," Spectrochim. Acta Part A Mol. Biomol. Spectrosc., vol. 75, no. 5, pp. 1523–1529, 2010.

[38] S. P. Vijayachamundeshwari, E. J. Jebaseelen Samuel, and N. Sundaraganesan, "Molecular structure, vibrational spectra, NMR and UV spectral analysis of sulfamethoxazole," Spectrochim. Acta Part A Mol. Biomol. Spectrosc., vol. 118, pp. 1–10, 2014.

[39] A. E. Reed, R. B. Weinstock, and F. Weinhold, "J. Chem. Phys.," vol. 83, pp. 735–743, 1985.

[40] A. E. Reed and F. Weinhold, "J. Chem. Phys.," vol. 83, pp. 1736–1747, 1985.

[41] A. E. Reed and F. Weinhold, "J. Chem. Phys.," vol. 78, pp. 4066–4072, 1983.

[42] F. Weinhold and C. R. Landis, Discovering Chemistry with Natural Bond Orbitals, John Wiley & Sons, New Jersey, 2012.

[43] R. J. Xavier and A. Prabaharan, "Vibrational spectroscopic investigations of 4,4-dimethyl-2-oxazoline: A density functional theory approach," Spectrochimica Acta Part A: Molecular and Biomolecular Spectroscopy, vol. 136, pp. 1530–1542, 2015.

Study of Kinetic and Neutronic Parameters for HEU and Potential LEU/MEU Fuels in a Typical MNSR

Muhammad Sohail*, Hassan Tariq, Rizwan Ahmed

Department of Nuclear Engineering, Pakistan Institute of Engineering & Applied Sciences (PIEAS), Nilore-45650, Islamabad, Pakistan

A B S T R A C T

The MTR-PC package, which combines WIMSD and CITATION codes, was used to calculate the effective delayed neutron fraction and prompt neutron lifetime for a Miniature Neutron Source Reactor (MNSR). In the Reduced Enrichment for Research and Training Reactors (RERTR) program, these kinetic parameters were calculated for various potential LEU and MEU fuels. The effect of composition changes due to fuel depletion on these parameters was studied for HEU and potential LEU/MEU fuels. The results of kinetic and other neutronic parameters for the HEU MNSR core are in agreement with the values in the literature. The delayed neutron fraction and prompt neutron lifetime showed minor variations over the 200 Effective Full Power Days (EFPD) burnup cycle of the MNSR cores for each fuel. The maximum change in delayed neutron fraction (β_{eff}) over the burnup cycle was found for UO$_2$ fuel with Zircaloy-4 clad system, showing the maximum ^{239}Pu production among all fuel types. The maximum neutron generation time (Λ) increase of 0.4μs was found in UAl$_4$ 90.3% enriched core.

Keywords: Kinetic parameters, MNSR, LEU fuels, Neutronic analysis, MTR-PC

1. Introduction

Before 1978, nuclear reactors for research and isotope production were mainly based on High-Enriched Uranium (HEU) fuels. This created a high proliferation risk as the fuel used in those reactors contained a large amount of ^{235}U isotope [1]. Consequently, in the light of the RERTR program, many reactors have been successfully converted to LEU fuels provided their performance remains within the acceptable criterion with minimum economic penalties [2].

The Miniature Neutron Source Reactors (MNSRs) are low-power reactors based on HEU fuel. A few MNSRs operate in different countries, mainly for research and training purposes. To a certain extent, other researchers have already done the conversion studies for some of them. The UO$_2$ as LEU fuel has been considered one of the study analyses for Syrian MNSR [3]. Similar studies were carried out for Ghana Research Reactor with UO$_2$, U$_9$Mo and U$_3$Si$_2$Al fuels as potential LEU fuels [4]. The analysis of core lifetime and inventory of isotopes for a typical MNSR was conducted for U-9Mo-Al and UO$_2$ as potential LEU fuel [5]. Uranium silicide and uranium molybdenum dispersed in aluminum matrix were included in another work for four potential LEU fuel options and Medium Enriched Uranium (MEU) fuels for similar calculations [6].

Besides core lifetime and isotope inventory calculations in respect of HEU to LEU/MEU conversion of typical MNSR core requires the estimation of the kinetic parameters for transient, accidental and stability analysis. However, the calculations of the kinetic parameters for alternative fuels for different MNSRs have been performed only at Beginning of Cycle (BOC). A. researchers used MCNP-4C computer code to estimate the kinetic parameters for a Syrian MNSR [7]. The prompt neutron lifetime for Nigeria MNSR (NIRR-1) reactor is calculated for both HEU and LEU cores [8]. In another study of core conversion of Ghana MNSR, the delayed neutron fraction is calculated for UO$_2$ fuel with Monte Carlo runs of the MCNP code [4].

The delayed neutron fraction (β_{eff}) sets the allowable limit of reactivity insertion to avoid prompt criticality. The neutron generation time (Λ) determines the power change rate on reactivity insertion. Delayed neutron fraction and neutron generation time depend on the fuel type and core arrangement. They are subjected to two kinds of changes: Firstly, the short-term changes that happen during a transient, a typical example is when reactor power is increased. This will harden the spectrum and lead to an increase in fast fission of ^{238}U. The change in neutron spectrum can also affect the magnitude of kinetic parameters in the core. The delayed neutron fraction is affected by fission in ^{238}U, and the neutron generation time is sensitive to the average speed of neutrons and the fission cross section of the fissile isotope. The hardening of the spectrum also changes the neutron generation time. The changes above are usually neglected to simplify the mathematical model. The long-term changes in the core isotopic composition about fuel burnup alter the effective delayed neutron and neutron generation time.

This work focuses on estimating kinetic parameters for conventional HEU and potential LEU/MEU fuels for typical MNSRs. The parameters β_{eff} and Λ are computed at different burnup steps to see the variation of these parameters. The MTR-PC neutronics calculation package, which includes computer codes WIMSD/4 and CITATION. These were used for the calculation of kinetic parameters of MTR type research reactor [9].

2. Brief introduction of the reactor

The reactor is a typical tank in pool type with Highly Enriched Uranium (HEU) fuel. The rated thermal power is 27kW and has self-limiting characteristics with large negative moderator temperature coefficient. Its core is almost square cylinder with 344 fuel pins and 10 non fuel pins (6 dummy pins and 4 tie rods). The only cadmium control rod is situated at the center of the core. The core has annular and bottom beryllium reflector. It also has a shim

tray at the top to add Be reflector plates for reactivity compensation. Water is used for neutron shielding and reflection. The vertical and core-mid-plane horizontal cross sections shown in Fig. 1 and the important design specifications are provided in Table 1.

Table 1: Some important design parameters of the reactor [10]

Parameters	Description
Reactor type/class	Tank-in-Pool/MNSR
Power (nominal/self-limiting; kW_{th})	27/87
^{235}U core loading (g)	994.8
^{235}U enrichment (%)	90
Material (fuel/clad/mod./reflector)	UAl_4/Al (303-1)/H_2O/Be
Control rod (meat/clad/length, cm/worth, mk)	Cd/S.S./23/6.7
Core (height/diameter; cm)	23/25
Fuel (meat-dia., cm/number of pins)	0.43/344
Excess reactivity (mk; cold, clean)	4.0
Number of irradiation sites (inner/outer)	5/5
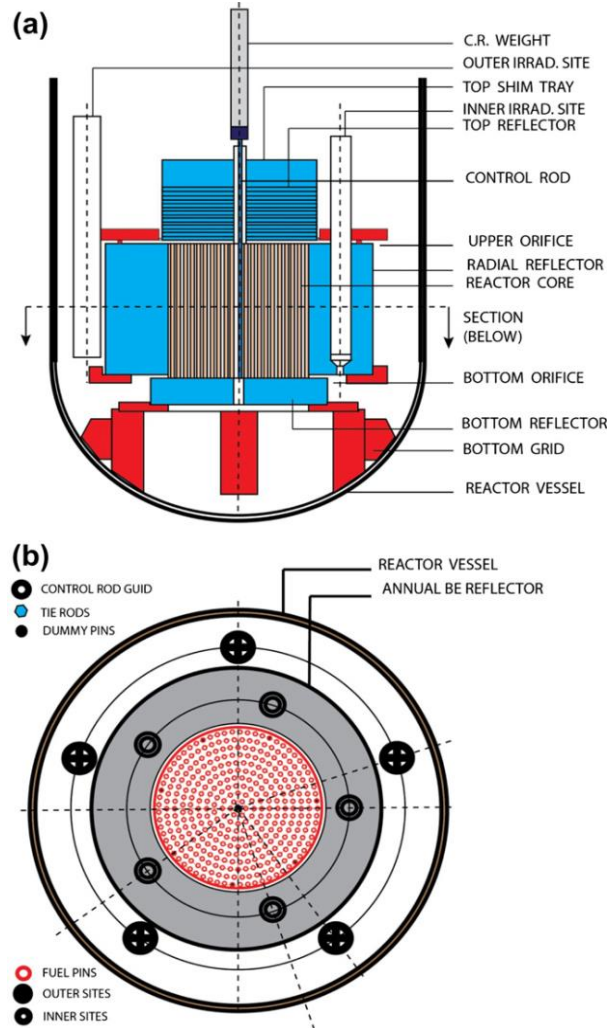
Fig. 1: Cross-sectional views of the MNSR system (a) vertical section and (b) horizontal section at the core mid-plane [6].

3. Theory and computational modeling

The MTR PC package has the ability to efficiently manage the transfer of the data among the lattice cell calculation code WIMSD4 [11] and diffusion theory based code CITATION through BORGES computer program [12].

The cluster option of WIMS for geometry modeling is used for the generation of microscopic cross sections (ENDF/B-IV library) along with $(1/v)_{avg}$. The energy group structure for which the set of cross sections are obtained is provided in Table 2 [5].

Table 2: Energy structure in WIMS

| Sr. No	WIMS Cross-section lib. groups	Upper limit (eV)	Mean Energy (eV)
1	1- 5	1.00000E+07	2.86531E+06
2	6-7	8.21000E+05	4.98350E+05
3	8	3.02500E+05	2.35282E+05
4	9 -11	1.83000E+05	8.64613E+04
5	12 -14	4.08500E+04	1.92995E+04
6	15-17	9.11800E+03	4.51877E+03
7	18-20	2.23945E+03	9.06898E+02
8	21-23	3.67262E+02	1.32845E+02
9	24-25	4.80520E+01	2.77001E+01
10	26-27	1.59680E+01	7.99200E+00
11	28-32	4.00000E+00	2.28035E+00
12	33-36	1.30000E+00	1.17996E+00
13	37-40	1.07100E+00	1.02030E+00
14	41-44	9.72000E-01	8.70724E-01
15	45 to 48	7.80000E-01	5.22494E-01
16	49 to 52	3.50000E-01	2.95804E-01
17	53 to56	2.50000E-01	1.58114E-01
18	57 to 60	1.00000E-01	7.07107E-02
19	61 to 64	5.00000E-02	3.53553E-02
20	65 to 69	2.50000E-02	1.58114E-04
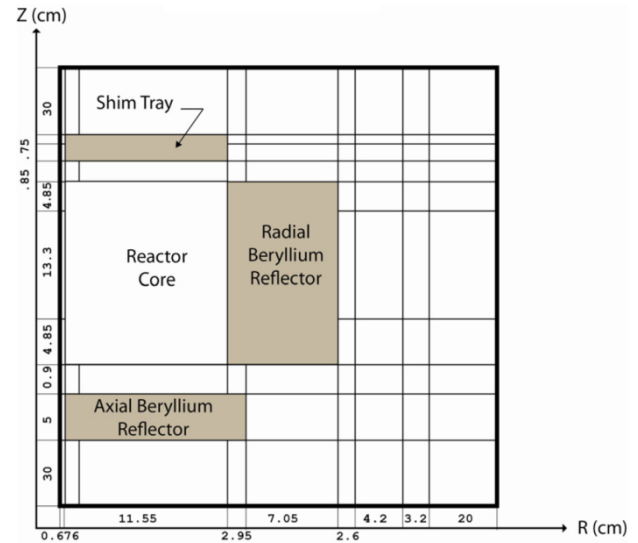
Fig. 2: The RZ-model of the MNSR system used in the CITATION calculations of HEU and the potential LEU cores [6]

From the group structure presented in Table 2, the first delayed neutron group falls within the 8th energy group, with a mean energy of 2.35282×10^2 eV. The remaining delayed neutron groups are distributed across the 6th and 7th energy groups, with a mean energy of 4.98350×10^3 eV. The kinetic parameters and multiplication factor are determined through CITATION simulations. The reactor geometry is modeled using the 2-dimensional r-z geometry option in the CITATION code, as illustrated in Fig. 2. The key steps involved in calculating the kinetic parameters are outlined in Fig. 3.

The perturbation option of CITATION code has been used which simplifies the computation of kinetic parameters.

The prompt neutron lifetime is calculated by CIATTION using Equation (1).

$$l = \frac{\Sigma_i \frac{V_i}{v(n)}}{\frac{1}{k}\Sigma_i V_i \Sigma_g \chi(g)\phi_{i,g}^* \Sigma_n v\Sigma_{f,n}\phi_{i,n}} \tag{1}$$

Here, i refers to mesh point location and n, g refers to energy groups. v, ϕ, ϕ^* and $v\Sigma\phi$ represents velocity, flux, adjoint flux and production rate of neutrons respectively.

CITATION also requires a set of decay constants and average delayed neutron yields. The decay constants for six groups of delayed neutron are given in Table 3.
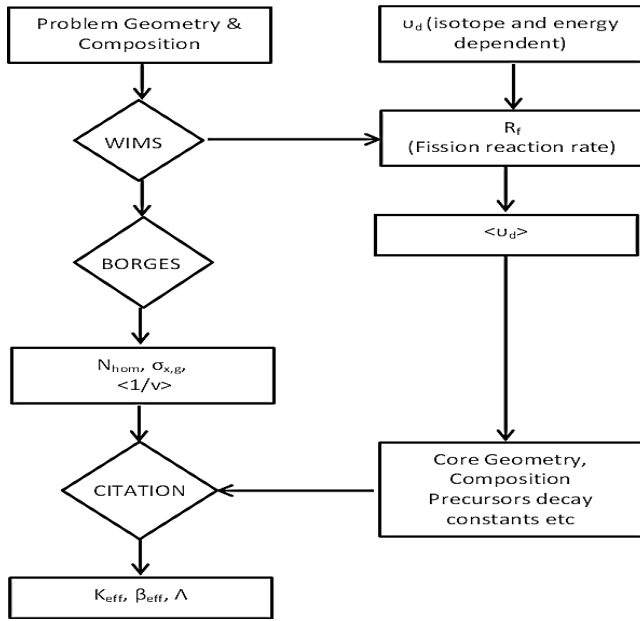
Fig. 3: Calculation flow chart

Table 3: Set of decay constant used in the calculations [13]

Delayed Group	Decay Constant (s^{-1})
1	0.0129
2	0.0311
3	0.134
4	0.331
5	1.26
6	3.21

Average delayed neutron yields are computed with the help of Equation (2) for CITATION. Where, the fast and thermal fission reaction rates are obtained from WIMSD.

$$(\overline{v_{dj}})^i = \frac{\int_V \int_{0.14eV}^{\infty} v_{dj}^i(E_f)\Sigma_f(r,E)\phi(r,\text{E})\,\text{d}E\text{d}V + \int_V \int_0^{0.14eV} v_{dj}^i(E_t)\Sigma_f(r,E)\phi(r,\text{E})\,\text{d}E\text{d}V}{\int_V \int_0^{\infty}\Sigma_f(r,E)\phi(r,\text{E})\,\text{d}E\text{d}V} \tag{2}$$

Where, v_{dj}^i, represents the delayed neutron yields for delayed neutron group, j and isotope, i. $\Sigma_f(r,E)$ and $\phi(r,\text{E})$

are the macroscopic fission cross section and flux for energy E and position r respectively.

The nuclides ^{235}U and ^{239}Pu have significant contribution towards the delayed neutron production. Their delayed neutron yields for fast and thermal energy ranges used for averaging by equation 3 are given in Table 4.

Table 4: Delayed neutron yield for U^{235} and Pu^{239} for fast and thermal energy ranges [14]

Delayed neutron groups	Delayed neutron yield for U^{235}		Delayed neutron yield for Pu^{239}	
	Fast	Thermal	Fast	Thermal
1	0.00063	0.00052	0.00024	0.00021
2	0.00351	0.00346	0.00176	0.00182
3	0.0031	0.0031	0.00136	0.00129
4	0.00672	0.00624	0.00207	0.00199
5	0.00211	0.00182	0.00065	0.00052
6	0.00043	0.00066	0.00022	0.00027

CITATION also estimates the fraction of delayed neutron in one group using Equation (3):

$$\beta_j = \frac{\Sigma_i V_i \Sigma_g \chi'(j,g)\phi_{i,g}^* \Sigma_b \beta_{b,j} N_{b,i} \Sigma_n v\sigma_{f,n,b,i}\phi_{i,n}}{\Sigma_i V_i \Sigma_g \chi(g)\phi_{i,g}^* \Sigma_n v\Sigma_{f,n}\phi_{i,n}} \tag{3}$$

Here, b, j refers to delayed neutron group j and isotope b and $\chi(g)$ is the delayed neutron distribution function. $N_{b,i}$ is the number density of isotope b at mesh location i.

4. Results and discussion

4.1 HEU core model validation

The results of the HEU

MNSR core calculations are summarized in Table 5. These results are compared with available literature values for key reactor parameters, including excess reactivity, control rod worth, the worth of top Be shim plates (Fig. 4), effective delayed neutron fraction, and prompt neutron lifetime.

4.1.1 Excess Reactivity

The computed excess reactivity of the standard HEU MNSR core is 4.19 mk, which is in close agreement with the Final Safety Analysis Report (FSAR) values reported by [10], which state an excess reactivity of 4.0 mk. The deviation observed between the computed and FSAR values are minimal, indicating improved accuracy compared to other reported computed values in the literature. Furthermore, [9] conducted a more detailed reactor core modeling using the CITATION code, obtaining results that showed even closer agreement with FSAR data. This suggests that enhanced computational modeling techniques contribute to more precise estimations of excess reactivity.

Table 5: Comparison of various computed values of parameters of the standard HEU fuel.

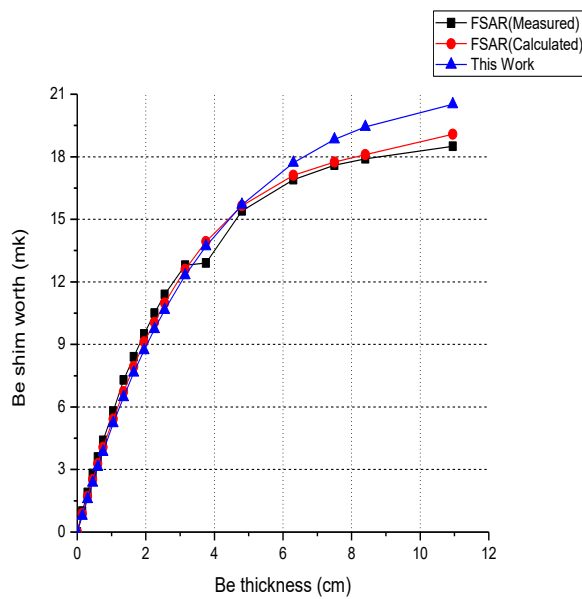| Parameters	This Work (% error with FSAR)	[4]	[15]	[6]	FSAR (Qazi et al., 1994)
Excess reactivity (mk)	4.19 (4.8)	4.51	4.05 (1.1)	4.32 (8)	4.0
CR worth (mk)	-6.75 (0.7)	-7.55	-6.39 (-4.6)	-7.11 (6.1)	-6.7
Shut down margin (mk)	-2.56 (-5.2)	-3.03	-2.34 (13.2)	-2.79 (3.4)	-2.7
Top Be worth (mk)	20.53 (7.7)	-	-	18.98 (0.4)	19.07
Delayed neutron fraction	0.00811 (2)	-	-	-	0.00795
Prompt neutron life time (µs)	0.0494 (6.7)	-	-	-	0.0463

Fig 4: Top reflector worth versus thickness of top Be plates

4.1.2 Control Rod Worth

The computed control rod worth of -6.75 mk aligns exceptionally well with the FSAR-reported value of -6.7 mk [10]. Compared with other reported calculations in Table 5, the current results exhibit significant accuracy, confirming the reliability of the employed computational methods. Additionally, the results for excess reactivity and control rod worth demonstrate an improvement over those obtained in previous studies that utilized the CITATION code with macroscopic cross sections generated using the WIMS cluster option and the RZ model [6]. This improvement suggests that employing a larger number of energy groups along with average microscopic cross sections enhances the precision of diffusion theory calculations.

4.1.3 Effective Delayed Neutron Fraction and Prompt Neutron Lifetime

The computed values for the effective delayed neutron fraction and prompt neutron generation time are 0.00811 and 0.0494 µs, respectively. These results closely align with FSAR-reported values, with deviations of 2% for the effective delayed neutron fraction and 6.7% for the prompt neutron lifetime. The relatively small errors further validate the accuracy of the adopted modeling approach. The close agreement indicates that the neutron physics parameters obtained from this study are reliable for safety and operational assessments of the HEU MNSR core.

Overall, the present study's computational results for HEU MNSR core parameters strongly agree with FSAR and previously reported values in the literature. The enhanced precision, particularly in excess reactivity and control rod worth calculations, demonstrates the effectiveness of employing detailed microscopic cross sections and a higher number of energy groups in diffusion theory modeling. These findings contribute to improved predictive capabilities

in reactor core physics calculations and enhance confidence in computational reactor analysis methodologies.

4.2 Potential LEU/MEU core analysis

Different LEU fuel types, i.e., UO_2 (Al, Zircaloy-4 clad), U_3Si–Al, U_3Si_2–Al, and U–9Mo–Al, have been considered for the MNSR system. The core configuration, such as the number of fuel pins, their physical and core dimensions, is the same as that of the original HEU MNSR system. This ensures the thermal-hydraulic characteristics remain unchanged. The computed results for these fuels considered for MNSR system are presented in Table 6.

The oxide fuel has relatively high density and, additionally, good thermal characteristics, making it the most attractive option among LEU fuels. However, zircaloy-4, along with aluminum, has been considered as a cladding material with oxide fuel. The higher loading of ^{235}U in oxide fuel requires relatively lower enrichment to obtain the desired value of excess reactivity, as is evident from the results in Table 6. The excess reactivity has been obtained close to the 4 mk value for all fuels with enrichment 12.5% (UO_2, Zircaloy-4 clad), 12.78% (UO_2, Al clad), 19.81% (U_3Si–Al), 22.31% (U_3Si_2–Al) and 24.29% (U–9Mo–Al) respectively.

The control rod worth and shutdown margin are computed as -5.57 mk and -1.55 mk for UO_2 fuel with Zircaloy-4 clad. The value is reasonably close with the corresponding reported values i.e. -5.748 [6], -5.437 mk [15] and -6.583 mk [4]. Similarly, the value of shutdown margin of -1.55 mk calculated in this work is also in comparable agreement with the corresponding reported values i.e. -1.768 [6] -1.43 mk [15] and -2.062 mk [4].

The enrichment values for the case of UO2 fuel with aluminum Al clad are slightly higher, i.e. 12.78%, due to the higher absorption cross-section of Al aluminum. The computed values of control rod worth as -5.61 mk and shutdown margin as -1.62 mk are in very good agreement with reported values, i.e. -5.615 mk and -1.606 mk [11], respectively.

For the case of U_3Si–Al fuel, the values of control rod worth and shutdown margin are found to be -5.84 mk and -1.79 mk which also agree well with corresponding reported values. However as mentioned above, the enrichment values obtained for potential LEU fuels including U_3Si_2–Al and U–9Mo–Al are slightly higher than 20%. The calculation results of the values for corresponding safely related parameters for both these fuels showed good agreement with the reported values.

4.3 Estimation of Kinetic parameters for potential LEU and MEU fuels

The kinetic parameters of potential LEU and MEU fuels are calculated with the procedure discussed in section 2. The values of effective delayed neutron fraction (β_{eff}) and mean neutron generation time (Λ) for different fuels are listed in Table 7. The β_{eff} values are not much different for these fuel

types, however, the mean neutron generation time has maximum value of 4.43μs for U_3Si_2-Al fuel and minimum value of 3.70μs for U-9Mo-Al fuel.

Table 6: Comparison of various computed values of parameters for different LEU and MEU fuels.

LEU fuel	Enrichment (%)	ρ_{ex} (mk)	C.R. worth (mk)	S.D margin (mk)
UO_2 ((Zr-4 clad)				
This Work	12.5	4.02	-5.57	-1.55
[6]	12.5	4.01	-5.748	-1.736
[4]	12.6	4.52	-6.583	-2.062
[15]	12.6	4.01	-5.437	-1.43
[5]	11.2	4.33	–	–
[16]	12.45	4.73	–	–
UO_2 (Al clad)				
This work	12.78	3.99	-5.61	-1.62
[6]	12.78	4.008	-5.615	-1.606
U_3Si–Al (-38%)				
This work	19.81	4.03	-5.82	-1.79
[6]	19.81	4.04	6.041	-2.001
[4]	19.75	4.043	-6.586	-2.542
U_3Si_2–Al				
This work	22.31	4.05	-5.84	-1.79
[6]	22.31	4.028	-6.115	-2.087
[4]	19.75	4.27	-6.655	-2.365
[5]	20.7	4.3	–	–
U–9Mo–Al (42.4%)				
This work	24.29	4.16	-4	0.16
[6]	24.29	4.047	-4.529	-0.4822

Table 7: Kinetic parameters of alternate LEU/MEU fuel at BOC.

Fuel	Enrichment (%)	β_{eff}	Λ (μs)
UO_2- Zircaloy-4 clad	12.50	0.00809	4.27
UO_2- Al clad	12.78	0.00810	4.24
U_3Si-Al	19.81	0.00809	4.40
U_3Si_2-Al	22.31	0.00809	4.43
U-9Mo-Al	24.29	0.00806	3.70

Burnup dependent calculations of kinetic parameters are performed with time step of 20 days for 200 EFPD for each fuel type. This corresponds to the reactor operation of 2 hours per day; 5 days a week sustained over a period of 10 years which is equivalent to 200 EFPD.

The results of β_{eff} and Λ for different fuels are shown in Fig. 5 to Fig. 8. The parameter β_{eff} has shown decreasing trend for all fuels owing to the production of Pu isotopes in the core. However, Λ has shown an increasing trend with burnup due to decrease in the macroscopic fission cross section. A decrease in β_{eff} and an increase in Λ would negatively impact the reactor period, reducing its magnitude as the fuel undergoes burnup. However, the small magnitude of changes in kinetic parameters due to fuel depletion would not significantly impact safety or the reactivity insertion margin.

The change in kinetic parameters for conventional HEU fuel i.e. UAl_4 is given in Fig. 5. An overall decrease of 5.8×10^{-7} is found in β_{eff}, which is the least among all the fuels. Whereas, an increase of 0.4μs in Λ is found at the EOC for UAl_4 fuel.
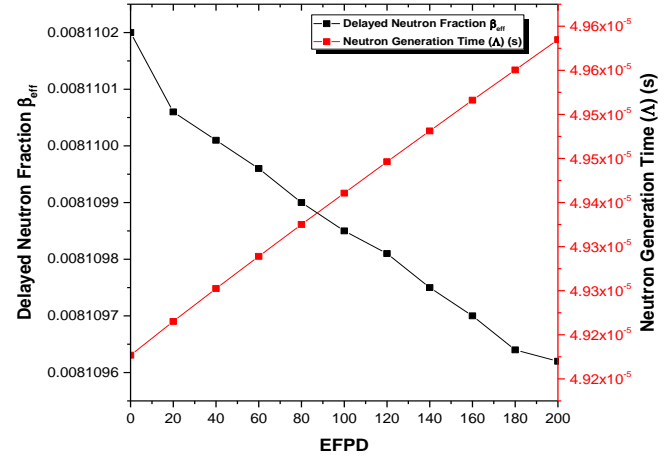

Fig. 5: Variation in kinetic parameters with burnup for standard HEU fuel.

The results for the variation in kinetic parameters are shown in Fig. 6 for ceramic fuels. The decrease in β_{eff} for ceramic fuels i.e. UO_2 with Zircaloy-4 clad and UO_2 with Al clad is 6×10^{-6} and 5.7×10^{-6} respectively. Meanwhile, the increase found in Λ are 0.3 and 0.2 μs respectively after 200 EFPDs.

The results of kinetic parameters for silicide dispersed fuels i.e. U_3Si-Al and U_3Si_2-Al are shown in Fig. 7. Both silicide fuels have shown an equal increase of 0.13μs in Λ values over the whole burnup cycle. However, the decrease in β_{eff} of U_3Si-Al and U_3Si_2-Al fuels are 4.3×10^{-6} and 4.0×10^{-6} respectively at the end of 200 EFPD.

The Fig. 8 is plotted for the calculated data for U-9Mo-Al fuel where the delayed neutron fraction has shown decrease by 3.1×10^{-6} and increase in neutron generation time by 0.1μs over the whole burnup cycle.
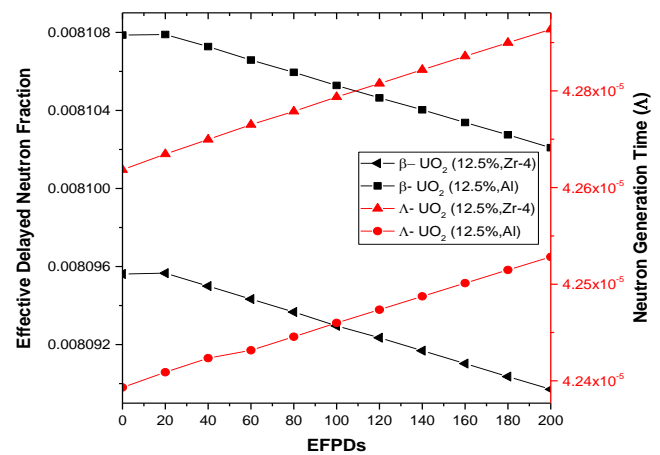

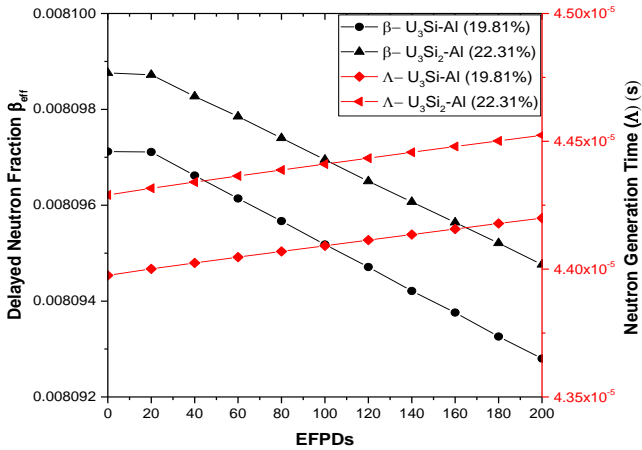Fig. 6: Variation of kinetic parameters for UO_2 with Zircaloy-4 clad and UO_2 with Al clad with burnup.

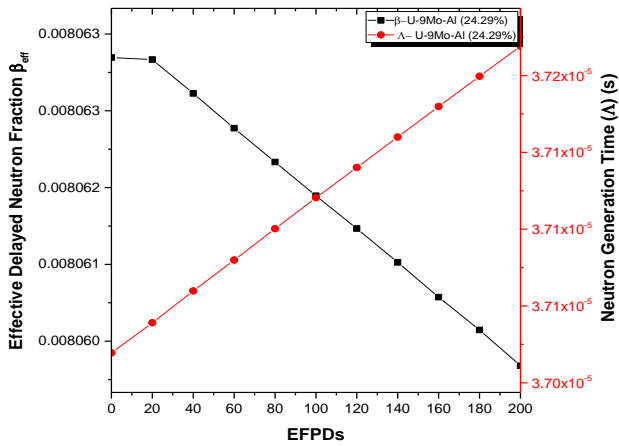Fig. 7: Variation of kinetic parameters for U_3Si-Al and U_3Si_2-Al with burnup

Fig. 8: The variation of kinetic parameters for U-9Mo-Al with burnup

Table 8 indicates that the net decrease in delayed neutron fraction for all fuel types is dependent on the production of Pu^{239} in the reactor core. The maximum decrease in effective delayed neutron fraction is observed in ceramic fuels as compared to other types due to relatively larger amount of Pu^{239}. A relatively hardened spectrum with Zircaloy cladding leads to an increase Pu^{239} production resulting in greater variations in the delayed neutron fraction. In contrast to Al, being lighter in mass is a more effective neutron moderator compared to zirconium alloy.

Table 8: Amount of Pu^{239} produced and net change in delayed neutron fraction.

Fuel	Change in β_{eff}	Amount of produced Pu^{239} (g)	
		This work	[5]
UO_2- Zircaloy 4 clad	6×10^{-6}	0.779	0.793
UO_2- Al clad	5.7×10^{-6}	0.773	-
U_3Si-Al	4.3×10^{-6}	0.528	-
U_3Si_2-Al	4×10^{-6}	0.472	-
U-9Mo-Al	3.1×10^{-6}	0.503	0.799

The neutron generation time depends on $<1/v>$ and neutron fission cross section. The increase in Λ with the burnup can be attributed to the increase in $<1/v>$ and

decrease in fission cross section. The net increase in Λ of all considered fuel is presented in Table 8.

5. Conclusion

This work focused on determining the variation in kinetic parameters as burnup proceeds for conventional HEU and potential LEU/MEU fuels for MNSR core. The calculations were carried out using MTR-PC package. The microscopic cross sections were generated using the cluster processing option in WIMS and RZ geometry for reactor modeling in CITATION. The model validation results showed good agreement of the computed values of excess reactivity, control rod worth, shutdown margin, effective delayed neutron fraction, and prompt neutron lifetime with the corresponding values found in literature for the HEU core. Four potential fuels UO_2 (Zircaloy-4 clad & Al-clad), U_3Si–Al, U_3Si_2–Al and U9Mo–Al, are considered for the analysis of kinetic parameters as LEU fuels. The parameters β_{eff} and Λ of HEU system for the clean core are in good agreement with the safety analysis report of the reactor. The error in the delayed neutron fraction is 2%, and in the prompt neutron lifetime is less than 7%. The kinetic parameters showed variation at different burnup steps. The decrease in β_{eff} is the result of ^{239}Pu production in the core. The highest variation is found in UO_2 12.5% enriched with Zr-4 clad system, which has the highest ^{239}Pu production among all fuels. The maximum increase in Λ of 0.4µs is seen in UAl_4 90.3% enriched core. The trend of variation of the kinetic parameters is in excellent agreement with the reported values.

References

[1] J. R. Askew, F. J. Fayers, and P. B. Kemshell, "General description of the lattice code WIMSD," *J. Brit. Nucl. Energy Soc.*, vol. 5, pp. 564–585, 1966.

[2] T. B. Fowler, D. R. Vondy, and G. W. Cunningham, "Nuclear reactor core analysis code citation," 1971.

[3] A. Hainoun, H. Haj Hassan, and N. Ghazi, "Determination of major kinetic parameters of the Syrian MNSR for different fuel loading using Monte Carlo technique," *Ann. Nucl. Energy*, vol. 36, pp. 1663–1667, 2009.

[4] Y. V. Ibrahim, M. O. Adeleye, R. L. Njinga, H. C. Odoi, and S. A. Jonah, "Prompt neutron lifetime calculations for the NIRR-1 reactor," *Adv. Energy Res.*, vol. 3, pp. 125–131, 2015.

[5] M. Iqbal, T. Mahmood, and S. Pervez, "Flow of kinetic parameters in a typical swimming pool type research reactor," *Ann. Nucl. Energy*, vol. 35, pp. 518–524, 2008.

[6] K. O. Ott and R. J. Neuhold, *Introductory Nuclear Reactor Dynamics*, 1st ed. Illinois, USA: ANS, 1985.

[7] G. R. Keepin, *Physics of Nuclear Kinetics*, 1st ed. Reading, MA: Addison-Wesley, 1965.

[8] I. Khamis and K. Khattab, "Lowering the enrichment of the Syrian miniature neutron source reactor," *Ann. Nucl. Energy*, vol. 26, pp. 1031–1036, 1999.

[9] J. R. Liaw and J. E. Matos, "MNSR flux performance and core lifetime analysis with HEU and LEU fuels," 2008.

[10] T. Mahmood, S. Pervez, and M. Iqbal, "Neutronic analysis for core conversion (HEU–LEU) of Pakistan research reactor-2 (PARR-2)," *Ann. Nucl. Energy*, vol. 35, pp. 1440–1446, 2008.

[11] A. Nawaz, S. M. Mirza, N. M. Mirza, and M. Sohail, "Analysis of core life-time and neutronic parameters for HEU and potential LEU/MEU fuels in a typical MNSR," *Ann. Nucl. Energy*, vol. 47, pp. 46–52, 2012.

[12] S. Pervez and M. Iqbal, "Performance evaluation of converted and upgraded PARR-1," 1998.

[13] M. K. Qazi, M. Israr, and A. Karim, Final Safety Analysis Report on Pakistan Research Reactor-2, PINSTECH-123, 1994.

[14] S. A. Sampong, A. Andam, J. Liaw, and J. Mattos, "Neutronic analysis for conversion of Ghana Research Reactor-1 facility using Monte Carlo methods and UO_2 LEU fuel," *Res. React. Fuel Manag. Meet. Int. Gr. React. Res.*, 2007.

[15] N. G. Sjöstrand, "Reduced enrichment for research and test reactors," *Nucl. Instrum. Methods Phys. Res., Sect. A*, vol. 256, pp. 193, 1987.

[16] S. Waqar, N. M. Mirza, and S. M. Mirza, "Comparative study of actinide and fission product inventory of HEU and potential LEU fuels for MNSRs," *Prog. Nucl. Energy*, vol. 51, pp. 129–134, 2009.

[17] S. M. Tasveer, S. Ahmad, K. S. Chaudri, and A. Ahmad, "Beryllium as reflector of MNSR," *Ann. Nucl. Energy*, vol. 35, pp. 1708–1712, 2008.

[18] W. Syed, K. S. Chaudri, and M. Sohail, "Development of coupled neutron physics/thermal hydraulics system using OpenMC and RELAP5," *Int. Conf. on Emerging Technologies*, 2016.

Quantum Optimization for Enhanced Combinatorial Algorithms

Pradeep Kumar Pandey, Ruchi Chaturvedi, Suraj Bhan Dangi[*]

Department of Computer Science & Technology, Sam Global University, Raisen, Madhya Pradesh, India

A B S T R A C T

The twenty-first century has been the era of data. Algorithms are crucial in tasks ranging from simple document searches to complex batching and scheduling jobs. Optimization techniques are often applied to enhance algorithms and achieve better results. As Moore rightly predicted, the exponential increase in transistors has led to a point where classical computers can no longer solve specific problems within a human timeframe. This paved the way for the development of quantum computers, which utilize quantum phenomena to solve problems. Quantum optimization techniques and algorithms have been designed to leverage the quantum advantage for improved optimization. This research compares and presents the results of quantum optimization techniques applied to classic combinatorial algorithms.

Keywords: Quantum Optimization, Combinatorial Algorithms, Quantum Computing, Algorithm Efficiency, Computational Complexity

1. Introduction

Quantum computers utilize quantum phenomena to execute various computations [1]. Quantum advantage primarily depends on two factors: first, the quantum computer itself, and second, the algorithms developed to leverage these quantum phenomena. The fundamental component of a quantum computer is known as a qubit. Qubits are said to exist in a superposition of two states: the off state (0) and the on state (1). Unlike a classical bit, which can be either in a 0 state or a 1 state, a qubit can be in both states simultaneously at the exact moment. This property allows n qubits to represent 2^n states at once.

Quantum computing relies on three main quantum properties of an atom:

i. Superposition

ii. Entanglement

iii. Interference

Superposition is the property that allows atoms to exist in multiple states simultaneously. This property enables quantum computers to scale and perform exponentially better than classical computers. Entanglement is the phenomenon where two atoms remain correlated, even when separated by vast distances [2]. This property facilitates the instantaneous transfer of information. Interference is the process by which an atom collapses from a superposition into a single state when it interacts with its environment. Interference plays a crucial role in information security, as even a small disturbance can cause the collapse of an atom's superposition state [3]. Another key phenomenon in quantum computing is quantum entanglement, which enables qubits to be intrinsically linked, regardless of distance. When entangled, the state of one qubit instantly determines the state of another, providing a means for highly efficient information transfer and parallel computation [4]. These quantum properties facilitate the execution of quantum algorithms such as Shor's algorithm for integer factorization, which threatens conventional cryptographic

security, and Grover's algorithm for searching unstructured databases exponentially faster than classical algorithms [5][6]. Quantum advantage, the point at which a quantum computer surpasses classical systems in problem-solving efficiency, depends on the hardware and algorithms designed to exploit quantum mechanics effectively. Developing quantum algorithms and error correction techniques is crucial for practical quantum computing applications. Current implementations of quantum computers include: superconducting qubits, trapped ions, and topological qubits, each offering distinct advantages and challenges regarding coherence time, scalability and noise resistance [7]. Despite significant advancements, quantum computing still faces considerable challenges, including qubit decoherence, error rates, and the need for large-scale fault tolerance [8]. Researchers continue to explore novel materials, quantum error correction codes, and hybrid quantum-classical algorithms to enhance the feasibility and scalability of quantum computing [9].

Our study focuses on applying the Quantum Approximate Optimization Algorithm (QAOA) to classical combinatorial problems such as: Max-Cut and Knapsack Problem, demonstrating its effectiveness in achieving optimized solutions. Using these quantum principles, the QAOA is used as a promising method for solving classical combinatorial problems like Max-Cut and the Knapsack problem. This study evaluates QAOA's effectiveness in finding optimized solutions and compares its advantages with classical techniques. By bridging classical and quantum optimization, it helps improve our understanding of quantum algorithms in problem-solving. Additionally, this research lays the groundwork for future studies by comparing QAOA with other quantum methods and benchmarking them against classical approaches.

1.1 Optimization

Optimization for any algorithm can be of two types: (1) Arriving at a solution that is closest to the expected result, and (2) the amount of time taken to arrive at the solution.

---

[*]Corresponding author:surajdangisd97@gmail.com

Below are some of the commonly used quantum optimization techniques for computing problems.

1.2 Quantum Annealing

Quantum annealing, or Quantum Stochastic Optimization, is an optimization technique that allows us to find the global minimum for functions with several local minima. Quantum annealing uses two main techniques to achieve its goal: (i) quantum fluctuations and (ii) quantum tunneling. Quantum fluctuations refer to the change in the energy level of a qubit by an external magnetic field which allows it to end up in the lowest energy level. This quantity that controls the magnetic field is called bias [10]. Quantum tunneling helps qubits propagate through potential barriers instantaneously without climbing them. These factors prove quantum annealing is more efficient and faster to converge to the optimal solution [11].

1.3 Quantum Approximate Optimization Algorithm (QAOA)

QAOA is an optimization technique that is used to solve combinatorial optimization problems like the NP-Hard Max-cut problem. The aim of the max cut problem is to obtain a value close to the maximum no. of edge cuts (C) possible in a given graph (G). Classical function with binary variables is encoded by introducing a quantum spin for each variable. QAOA has proven to be more efficient than the classical technique in arriving at the closest solution [12].

1.4 Adiabatic Quantum Optimization

Adiabatic Q-optimization aims to find the optimal solution by evolving the ground state rapidly. Similar to quantum annealing, this technique also starts with a Hamiltonian ground state. Unlike quantum annealing, which uses quantum tunneling to pass through states that might end up in a local minimum, this adiabatically evolves and arrives at the optimal solution [13,14].

2. Methodology

QAOA Implementation: The QAOA is a hybrid quantum-classical algorithm designed to solve combinatorial optimization problems efficiently. It operates by iteratively optimizing a quantum circuit parameterized by classical optimization techniques. Our implementation of QAOA includes several crucial aspects:

2.1 Parameter Selection

The QAOA performance heavily depends on the selection of variational parameters β and γ, which control the evolution of the quantum state. We employed gradient-based and heuristic optimization methods, such as Nelder-Meadand COBYLA, to fine-tune these parameters.

2.2 Circuit Design:

The quantum circuit for QAOA consists of alternating layers of problem Hamiltonian evolution and mixing Hamiltonian evolution. We used a depth parameter "*p*" to control the number of layers, balancing accuracy and quantum resource constraints.

3. Proposed Work

3.1 MAX CUT

Max–Cut problem is a classical NP-Hard problem that tries to find the maximum cut which splits the graph into two sets that would have the greatest number of edges in between it [9]. QAOA is a quantum algorithm that leverages the use of quantum properties to arrive at an optimized approximate solution. QAOA is a heuristic algorithm that provides the closest answer in polynomial time. The algorithm does not guarantee performance but is expected to produce a result closest to the actual solution [10]. The circuit for finding the Maximum-Cut of the graph starts by placing all the qubits in superposition. This becomes the initial state. A unitary is applied to the circuit according to the Hamiltonian for the graph. Later, a mixing unitary is applied. Optimal parameters for the circuit are initialized using a classical optimization algorithm, which is then applied to a QAOA circuit. Steps are repeated until convergence is achieved.
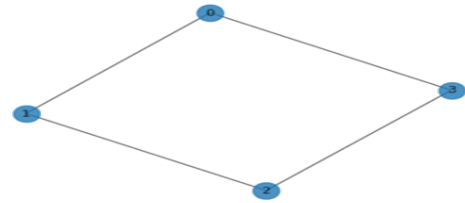

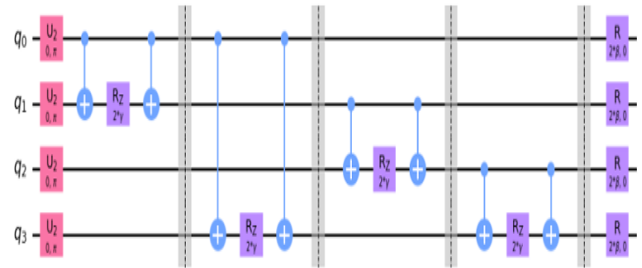Fig. 1 Graph with 4 nodes

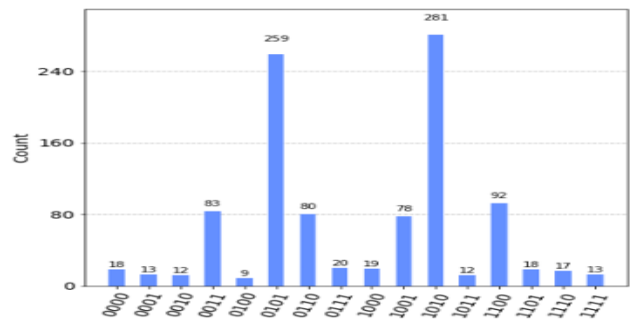Fig. 2 Circuit for solving using QAOA

Fig. 3 Results for Max-Cut with 4 nodes

QAOA also guarantees to achieve the most optimal solution for weighted Max-Cut problems. Here a Hamiltonian model of the weighted graph is generated which is then applied to the QAOA to find the maximum cut [7].

3.2 Knapsack Problem

The Knapsack problem is an NP-complete problem that involves combinatorial optimization. The problem involves finding the set of items that give the maximum value for a given knapsack weight. The problem has two flavors; one is the 0-1 Knapsack problem that only allows to add only one copy of an item. The bounded knapsack allows many copies of an item but restricts it to an upper bound. The quantum optimization for Knapsack is carried out using QAOA. The circuit is first initialized to superposition. Hamiltonian is constructed for the problem. The Hamiltonian is solved using the Minimum Eigen Optimizer. Thus, the result is obtained by finding the maximum value of the objective function.

Table 1 Max Cut Results using QAOA
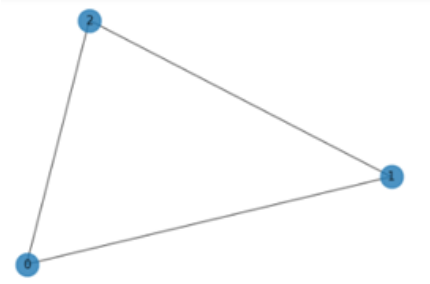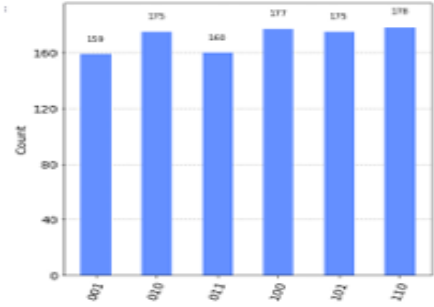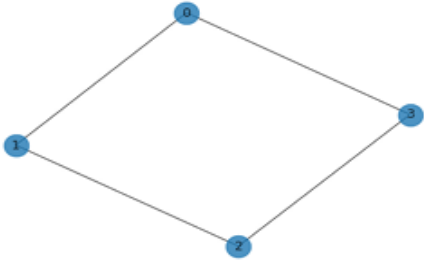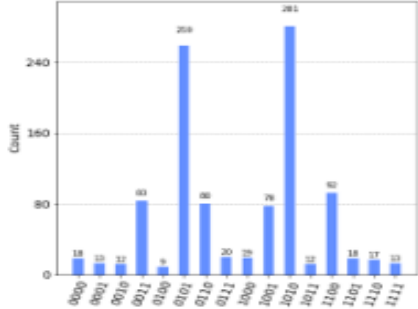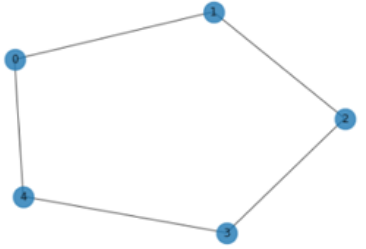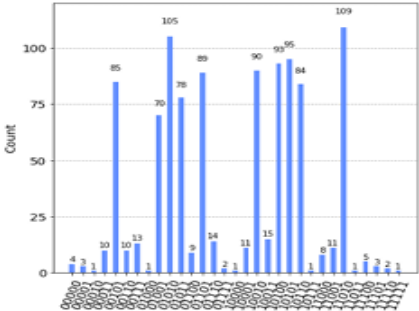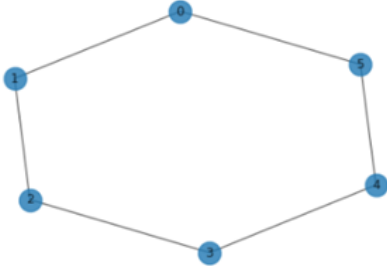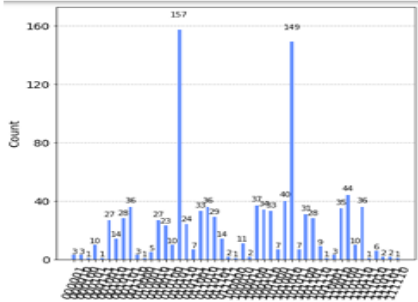
No of Nodes	Graph	Max-Cut Solution using QAOA
3		
4		
5		
6		

Table 2 Knapsack Results using QAOA

No. of items	Values	Maximum Weight of Knapsack	Weights	Objective function (Max Z)	Solution	Time taken (s)
5	[3, 4, 5, 6, 7]	10	[2, 3, 4, 5, 6]	$3^*x\_0 + 4^*x\_1 + 5^*x\_2 + 6 x^*x\_3 + 7^*x\_4$	[0, 1, 3]	4.285
6	[3, 4, 5, 6, 7,8]	12	[2, 3, 4, 5, 6,7]	$3^*x\_0 + 4^*x\_1 +5^*x\_2 + 6^*x\_3 + 7^*x\_4 +8^*x\_5$	[0, 2, 4]	1.241
7	[3, 4, 5, 6, 7,8,2]	15	[2, 3, 4, 5, 6,7,10]	$3^*x\_0 + 4^*x\_1 +5^*x\_2 + 6^*x\_3 + 7^*x\_4 +8^*x\_5 2^*x\_6$	[0, 1, 2, 4]	11.46

4. Advantages of Quantum Optimizers over Classical Optimizers

Quantum computing leverages superposition, allowing quantum bits (qubits) to exist in multiple states simultaneously rather than being confined to a single binary state like classical bits. This capability significantly enhances computational power, enabling the exploration of many possible solutions in parallel before arriving at an optimal result. For combinatorial optimization problems, this property provides a key advantage, as it allows quantum algorithms to evaluate numerous potential solutions efficiently. These problems are first mathematically modelled using a Hamiltonian function, representing the system's total energy, encoding the constraints and objectives of the optimization problem. Once the problem is formulated in this manner, Quantum optimizers are employed to find the best solution. Quantum optimizers are generally categorized into two types:

4.1 Heuristic-based optimization:

These methods use probabilistic and approximation techniques to explore the solution space and converge toward the most optimal solution. Examples include QAOA and the variational quantum Eigen solver (VQE).

4.2 Performance-based optimization:

These techniques focus on reducing time complexity, leveraging quantum speedup to solve problems faster than their classical counterparts. Algorithms such as Grover's search or quantum annealing fall into this category, enabling more efficient computations for large-scale problems.

By integrating these optimization strategies, quantum computing presents a promising alternative to classical approaches, particularly for complex combinatorial problems that require evaluating many possible solutions within a feasible timeframe. By incorporating these optimization strategies, quantum computing emerges as a promising alternative to classical approaches, particularly for solving complex combinatorial problems that involve evaluating a vast number of possible solutions within a feasible timeframe.

5. Conclusion

This research explores the potential of the QAOA in solving classical combinatorial problems such as the Max-Cut and Knapsack Problem, both of which are fundamental in optimization and have wide-ranging applications in fields like logistics, finance, and network design. Our study demonstrates that QAOA effectively provides optimized solutions for these problems by leveraging quantum superposition and entanglement to explore multiple solution spaces simultaneously. QAOA consistently achieves near-optimal results across various problem instances through iterative circuit optimization and variational parameter tuning. Despite its promising performance, the effectiveness of QAOA is influenced by factors such as quantum hardware noise, decoherence, and the selection of variational parameters. These challenges highlight the necessity for further refinement in quantum error mitigation and hybrid classical-quantum optimization techniques to improve their scalability and real-world applicability. Additionally, the depth of the QAOA circuit plays a crucial role in the accuracy of the solution, requiring a balance between computational complexity and hardware constraints.

6. Future Scope

Future research could extend this work by applying QAOA to a broader range of combinatorial problems, such as the Traveling Salesman Problem and Graph Partitioning, to assess its effectiveness across diverse optimization landscapes. Comparative studies with alternative quantum optimization methods, including Quantum Annealing and Variational Quantum Eigen solver VQE, could provide deeper insights into the relative advantages of different approaches. Further exploration into hybrid quantum-classical strategies, improved error mitigation techniques, and scalability analysis will be essential for enhancing the feasibility of QAOA on near-term quantum hardware. Moreover, testing QAOA across various quantum architectures, such as superconducting qubits, trapped ions, and photonic quantum systems, may uncover hardware-specific optimizations that improve performance. These directions will help advance quantum optimization techniques closer to practical real-world applications.

References

[1] M. A. Nielsen and I. L. Chuang, *Quantum Computation and Quantum Information*. Cambridge, U.K.: Cambridge Univ. Press, 2010.

[2] R. P. Feynman, "Simulating physics with computers," *Int. J. Theor. Phys.*, vol. 21, no. 6–7, pp. 467–488, 1982.

[3] J. Preskill, "Quantum computing in the NISQ era and beyond," *Quantum*, vol. 2, p. 79, 2018.

[4] C. H. Bennett and D. P. DiVincenzo, "Quantum information and computation," *Nature*, vol. 404, no. 6775, pp. 247–255, 2000.

[5] P. W. Shor, "Polynomial-time algorithms for prime factorization and discrete logarithms on a quantum computer," *SIAM J. Comput.*, vol. 26, no. 5, pp. 1484–1509, 1997.

[6] L. K. Grover, "A fast quantum mechanical algorithm for database search," in *Proc. 28th Annu. ACM Symp. Theory Comput. (STOC)*, 1996, pp. 212–219.

[7] F. Arute *et al.*, "Quantum supremacy using a programmable superconducting processor," *Nature*, vol. 574, no. 7779, pp. 505–510, 2019.

[8] S. J. Devitt, W. J. Munro, and K. Nemoto, "Quantum error correction for beginners," *Rep. Prog. Phys.*, vol. 76, no. 7, p. 076001, 2013.

[9] M. Kjaergaard, M. E. Schwartz, J. Braumüller, P. Krantz, J. I. J. Wang, S. Gustavsson, and W. D. Oliver, "Superconducting qubits: Current state of play," *Annu. Rev. Condens. Matter Phys.*, vol. 11, pp. 369–395, 2020.

[10] J. Liu, D. An, D. Fang, J. Wang, G. H. Low, and S. P. Jordan, "Efficient quantum algorithm for nonlinear reaction-diffusion equations and energy estimation," *Commun. Math. Phys.*, vol. 404, no. 2, pp. 963–1020, 2023.

[11] A. Lucas, "Ising formulations of many NP problems," *Front. Phys.*, vol. 2, no. 1, pp. 5–17, 2014.

[12] T. Kadowaki and H. Nishimori, "Quantum annealing in the transverse Ising model," *Phys. Rev. E*, vol. 58, no. 5, pp. 5355–5363, 1998.

[13] S. Kirkpatrick, C. D. Gelatt Jr., and M. P. Vecchi, "Optimization by simulated annealing," *Science*, vol. 220, no. 4598, pp. 671–680, 1983.

[14] F. Glover and M. Laguna, "Tabu search," *Kluwer Acad. Publ.*, vol. 1, no. 1, pp. 1–32, 1997.

[15] D. S. Johnson, "The NP-completeness column: An ongoing guide," *J. Algorithms*, vol. 3, no. 2, pp. 182–195, 1982.

Information for Authors

Submission: Manuscripts [in Word (.doc, .docx, .rtf)] should be submitted by one of the authors of the manuscript through the online submission system at www.thencleuspak.org.pk after registration of corresponding author. If for some technical reason on-line submission is not possible, then write an email describing the problem along with your phone no. at editorinchief@thenucleuspak.org.pk

Terms of Submission: Each submission to The Nucleus implies that the manuscript presents the results of original scientific research and has not been published nor has been submitted for publication elsewhere. The article is written in clear and Standard English. The reported research meets all applicable ethical standards and research integrity. The submitted manuscripts is screened for plagiarism during the editorial process.

Units of Measurement: should be presented simply and concisely using System International (SI) units.

Article Structure

Subdivision - numbered sections: The article should be divided into clearly defined and numbered sections. Subsections should be numbered 1.1 (then 1.1.1, 1.1.2, ...), 1.2, etc. (the abstract is not included in section numbering). Any subsection may be given a brief heading. Each heading should appear on its own separate line.

Title: should be concise and informative. Avoid abbreviations and formulae where possible.

Author names and affiliations: Provide complete name of all the authors, their affiliation, complete postal addresses, contact numbers and e-mail addresses. Present the authors' affiliation addresses below the names. Indicate all affiliations with a lower-case superscript letter immediately after the author's name. Clearly indicate the corresponding author by superscript*. Further when manuscript is under review process, as per policy of the journal, author cannot be addeded, deleted and sequence of author can't be altered.

Keywords: Provide a maximum of 6 keywords, These keywords will be used for indexing purposes.

Introduction Section: States the objectives of the work and provides an adequate background, avoiding a detailed literature survey or a summary of the results.

Experimental Section: should contain sufficient detail to allow the work to be reproduced. Methods already published should be indicated by a reference, only relevant modifications should be described.

Theory/calculation Section: Should extend, not repeat, the background to the article already dealt with in the Introduction and lay the foundation for further work. In contrast, a Calculation section represents a practical development from a theoretical basis.

Results and Discussion: should provide the significance of the results of the work. A combined Results and Discussion section is often appropriate. Avoid extensive citations and discussion of published literature.

Conclusions: It should be presented in a short Conclusions section.

Acknowledgments: (if any) should be included at the very end of the paper before the references and may include supporting grants, presentations, and so forth.

References: We follow IEEE style for citations of references. Must be numbered consecutively and citations of references in text should be identified using numbers in square brackets (e.g., as discussed by Smith [9]; as discussed elsewhere [9, 10]). Reference to a publication:

[Ref number] Author's initials. Author's Surname, "Title of article," Title of journal abbreviated in Italics, vol. number, issue number, page numbers, Abbreviated Month Year.

[4] K.A. Nelson, R.J. Davis, D.R. Lutz, and W. Smith, "Optical generation of tunable ultrasonic waves," Journal of Applied Physics, vol. 53, no. 2, pp. 1144-1149, Feb., 2002.

For more details please see the link IEEE style for citations of different materials

Figures and Tables: Include all figures and tables in the word file of the manuscript. Figures and tables should not be submitted in separate files. If the article is accepted, authors may be asked to provide the source files of the figures. All figures should be cited in the paper in a consecutive order. In all figures, remove all unnecessary boxes, lines, marks. The resolution of all the figures must be at least 300 dpi. Tables should be cited consecutively in the text. Every table must have a descriptive title and if numerical measurements are given, the units should be included in the column heading. Vertical rules should not be used.